Centro de Investigación Científica y de Educación Superior de Ensenada, Baja California

CICESE

Doctorado en Ciencias
en Nanociencias

Diseño de una membrana reactiva para el tratamiento de aguas recuperadas mediante buckypapers

Tesis
para cubrir parcialmente los requisitos necesarios para obtener el grado de
Doctor en Ciencias

Presenta:

Enrique Contreras Bernabe

Ensenada, Baja California, México
2019

Tesis defendida por

Enrique Contreras Bernabe

y aprobada por el siguiente Comité

Dr. José Manuel Romo Herrera	**Dra. Mercedes Teresita Oropeza Guzmán**
Codirector de tesis	Codirector de tesis

Miembros del comité

Dr. Óscar Edel Contreras López

Dr. Santiago Camacho López

Dr. Gabriel Alonso Núñez

Dr. Ulises Jesús Tamayo Pérez

Dr. Sergio Fuentes Moyado
Coordinador del Posgrado en Nanociencias

Dra. Rufina Hernández Martínez
Directora de Estudios de Posgrado

Resumen de la tesis que presenta **Enrique Contreras Bernabe** como requisito parcial para la obtención del grado de Doctor en Ciencias en Nanociencias.

Diseño de una membrana reactiva para el tratamiento de aguas recuperadas mediante buckypapers

Resumen aprobado por:

Dr. José Manuel Romo Herrera	**Dra. Mercedes Teresita Oropeza Guzmán**
Codirector de tesis	Codirector de tesis

En este trabajo, se obtuvo un conjunto de muestras de nanotubos de carbono dopados con nitrógeno (CNx) variando la proporción de nitrógeno grafítico, aumentado sistemáticamente la temperatura de síntesis. Esto permitió evaluar el papel del nitrógeno grafítico de los CNx en la reacción de reducción de oxígeno (ORR). Las muestras con alto contenido de nitrógeno grafítico favorecieron la vía de los dos electrones para la ORR no solo en medios básicos (pH = 13) sino también en medios neutros (pH = 7), lo que representa una alternativa atractiva para la remediación de aguas recuperadas a través de la generación de H_2O_2 in situ. Se propone un mecanismo para argumentar que la formación de H_2O_2 debería favorecerse en presencia de sitios de nitrógeno grafítico. Además, se exploró la dispersión y estabilización de nanopartículas de magnetita mediante ultrasonido y su capacidad para la eliminación de una molécula prueba (rojo amaranto), observando buenos resultados no solo en la reacción de Fenton, sino en la foto-Fenton y la fotocatálisis debido a la interacción con la luz UV con la magnetita. Los mejores resultados se evaluaron en el agua recuperada de la ciudad de Tijuana observando una buena eliminación de los compuestos orgánicos recalcitrantes en el agua. Por otro lado, se exploró el anclaje de la magnetita dispersa en nanotubos de carbono para ensamblar buckypapers decorados con Fe_3O_4 que pueden actuar como fuente de Fe (II) generando la reacción de Fenton cuando interactúan con H_2O_2. Finalmente, se diseñó un prototipo de reacción que explota la capacidad de los buckypapers de nanotubos de carbono dopados con nitrógeno para la producción de peróxido de hidrógeno (en el cátodo) y un buckypaper decorado con Fe_3O_4 (en el ánodo) para la reacción de Fenton, dando como resultado un material funcional, promoviendo la reacción de Fenton para la eliminación de contaminantes recalcitrantes de las aguas residuales de la ciudad de Tijuana.

Palabras clave: Nanotubos de carbono dopados con nitrógeno, reacción de reducción de oxígeno, reacción Fenton.

Abstract of the thesis presented **by Enrique Contreras Bernabe** as a partial requirement to obtain the Doctor of Science degree in Nanoscience.

Design of a reactive membrane for the treatment of reclaimed water using buckypapers

Abstract approved by:

Dr. José Manuel Romo Herrera	**Dra. Mercedes Teresita Oropeza Guzmán**
Codirector de tesis	Codirector de tesis

A set of N-doped carbon nanotube (CNx) samples with the proportion of graphitic nitrogen systematically increased was obtained by modifying the synthesis temperature. This allowed evaluation of the role of the CNx graphitic nitrogen in the oxygen reduction reaction (ORR). The samples with high graphitic nitrogen content favored the two-electron pathway for the ORR not only in basic media (pH = 13) but also in neutral media (pH = 7), representing an attractive alternative for wastewater remediation through the on-site generation of H_2O_2. A mechanism is proposed to explain how the formation of H_2O_2 should be favored in the presence of graphitic nitrogen sites.Additionally, it was explored the dispersion and stabilization of magnetite nanoparticles using ultrasound, and its ability for the removal of a target molecule (amaranth red), giving good results not only in the Fenton reaction, but in the photo-Fenton, and photocatalysis of the magnetite due to the interaction with UV light. The best results were evaluated in the reclaimed water of Tijuana City observing good removal of the organic recalcitrant compounds in the water. On the other hand, it was explored the anchoring of the dispersed magnetite on carbon nanotubes to fabricate buckypapers decorated with Fe_3O_4 that could act as source of Fe (II) to generate the Fenton reaction when they interact with H_2O_2. Finally, it was designed a prototype reactor to harness the ability of the nitrogen-doped carobn nanotubes buckypapers for the hydrogen peroxide production in the cathode site and a Fe_3O_4 decorated buckypaper as the anode for the Fenton reaction, giving to a functional material, promoting the Fenton reaction for the remotion of recalcitrant pollutants from Tijuana's city wastewater.

Keywords: Nitrogen-doped carbon nanotubes, oxygen reduction reaction, Fenton reaction

Dedication

A Isabella

Quién sin saberlo forjo el hombre que ahora soy y me dio las fuerzas para continuar cuando todo parecía obscuridad

Acknowledgement

En esta tesis doctoral quiero agradecer a:

Mis padres, gracias papá por siempre estar a mi lado y siempre tener un consejo cuando lo necesitaba, gracias mamá por siempre apoyarme y escucharme. Estoy, y estaré eternamente agradecido con el esfuerzo que han hecho por mí.

A mi director de tesis, Dr. José Manuel Romo Herrera, quien fungió más allá de sus deberes de director de tesis, se volvió un mentor, un modelo a seguir e indudablemente un buen amigo, muchas gracias por aguantarme todos estos años.

A mis mejores amigos, Fernando Soto, Uriel Santoro y Mónica Vázquez, por siempre estar allí cuando más los necesité, en verdad mucho de mi trabajo esta soportado en sus hombros.

Mis amigos que conocí en mi estancia de posgrado, Luis Víctor Torres Merino, José Ruiz Marizcal, Brandon Huerta, Christian Palacios. Gracias, de ustedes he aprendido más de lo que se imaginan.

A mi comité tutoral, por estar siempre presente durante este trabajo de tesis.

Table of Contents

List of Figures

List of Tables

List of Equations

Chapter 1. Introduction

Currently, it is estimated that 780 million people have problems obtaining potable water (most of them are from Asia, Central and South America, and Africa). The United Nations (UN) reported that almost 1.8 billion people would face water scarcity in 2025 (Das et al., 2017).

Only 0.025% of the total amount of water on the planet is available for human consumption. Therefore, the reuse of wastewater is of a paramount importance given that a large part of the world population will face water stress problems shortly (S. C. Ameta, 2018).

1.1 Conventional wastewater technologies

Conventional wastewater treatment can be organized in three general areas: physical methods, chemical methods, and energy-intensive methods.

Physical methods are also known as primary treatment, which consists in the separation of the solids from the liquids, such as filtration, centrifugation, and sedimentation.

Chemical methods, also referred as secondary treatment, consist in the chemical interactions within the contaminants, helping in the separation of the contaminants from water or/and assist in the removal or neutralization of harmful effects associated with these contaminants. Some of these chemical methods are coagulation, flocculation, aerobic and anaerobic (also called biochemical methods) treatments.

Energy-intensive technologies, also called third treatment, have a role in the sterilization of water; some of these technologies are the thermal methods, the UV sterilization and electrochemical techniques (Cheremisinoff, 1997).

However, conventional methods for cleaning wastewater are quite expensive, and cannot remove heavy metals nor recalcitrant organic materials. Besides, the aggressive chemicals used in the chemical treatment and the obtained toxic sludge add contamination to the environment.

1.2 Wastewater treatment technologies based in nanomaterials

Nowadays, there is a movement in central Europe looking toward the reduction of chemical treatments in order to reduce residual chemicals in the wastewater treatment.

The nanomaterials can improve the wastewater treatment harnessing the size-dependent properties of materials such as: high catalytic surface area, fast dissolution, strong sorption, quantum confinement effect, and localized surface plasmon resonance among others.

Currently there are three principal physicochemical phenomena used for the water research using nanostructures such as adsorption, advanced oxidation process and filtration as enlisted in table 1 (Das et al., 2017).

Table 1. Nanomaterials for cleaning wastewater.

Physicochemical phenomena	Nanomaterials	
Adsorption	Carbonaceous Materials	Carbon Nanotubes
		Carbon Nanofibers
		Graphene
		Multifunctional carbon
		Superabsorbents
	Metal and Metal Oxide nanoparticles	Nanoscale zero valent iron
		Nano titanium dioxide
		Nano iron oxide
		Nano silicon dioxide
		Nano aluminum oxide
		Bimetallic nanoparticles
Advanced Oxidation Process	Photocatalysis materials	Metal and Metal Oxide nanoparticles
		Doped carbon nanostructures photocatalysts
		Doped perovskite material photocatalyst
	Nano-catalytic Materials for Air Wet Oxidation	Carbon Nanostructures
		Metal and Metal Oxide nanoparticles
	Nanohybrids Materials	
Filtration	Carbon Nanostructures	Carbon Nanotubes
		Graphene Family Members
	Inorganic Nanoparticles	Nanoceramic
		Biometric Nano-polymer

The diversity in the physicochemical phenomena related to the nanostructures as well as the ability to synthesize nanomaterials with specific activities allow to include them in water purification processes or add them to secondary or tertiary module treatment to eliminate hard contaminants such as: removal of heavy metals, hydrocarbons, recalcitrant organic materials, agrochemicals, drugs and/or another types of emerging pollutants (Saldivar & Walsh, 2015).

1.3 Global Investment in the development of nanomaterials for wastewater technologies

Therefore, wastewater treatment technologies based in nanomaterials has attracted the attention of scientists, due to the need to increase the efficacy of current wastewater treatment technologies and the development of novel technologies.

1.3.1 Worldwide investment in water research using nanostructures

At present, governments around the globe are investing in the developing of next-generation water supply systems. The United States (USA) has invested 1.5 billion dollars to the National Nanotechnology Initiative (NNI) for water research in 2015. While the European Commission for Horizon 2020 had invested 110 billion dollars for researching, where $92 million USD are for water innovation.

1.3.1 Mexican investment for the water research

México is currently participating with the European Union by the CONACYT H2020 co-founding mechanism investing 10 million Euros. Mexico has not clear statistics if any type of nanostructure is already used for purification, secondary or tertiary treatment on a large scale (Saldivar & Walsh, 2015).

Laura Saldivar (2015) surveyed top Mexican universities in the field of nanotechnology and water (CIMAV, IPICYT, UNAM, UAM, BUAP, U de Gto, and UCM). These universities referred the 66% of their funding to CONACYT and the 34% from the private sector.

Chapter 2. State of the Art

The main purpose of conventional water treatments (such as primary, secondary and tertiary) only transfer the pollution from one phase to another. Therefore, a novel technology process to destroy the organic pollutants is needed. The advanced oxidation processes (AOP) have been developed as emerging technologies which resulted in the total mineralization of most of the organic pollutants. (S. C. Ameta, 2018).

2.1 Advanced Oxidation Process

The AOPs are efficient to treat toxic organic pollutants and the complete removal of the emerging pollutants such as dyes, pesticides, antibiotics, etc. AOPs refer to a set of oxidative water treatments that are used for toxic effluents at factories, hospitals, and wastewater treatment plants. The usual AOPs are Fenton ($Fe^{2+} + H_2O_2$), electrolysis (electrodes + current), sonolysis (ultrasound), microwaves + H_2O_2, photolysis (UV+ H_2O_2), photocatalysis (light + catalyst), and photo-Fenton (solar light + Fenton).

The AOPs involves the formation of hydroxyl free radicals interacting with organic pollutants via free radical addition or an hydrogen abstraction pathway. It generates an oxidation of the organic pollutants and then forming byproducts like ketones, aldehydes or alcohols. Finally, the oxidation of the byproducts generates less toxic and molecules more susceptible to bioremediation.

One of the most oxidizing agent is the hydroxyl radical which presents one of the highest electrochemical oxidation potential of 2.8 V vs. SCE (as shown in table 2), that's why the hydroxyl free radical is the most oxidizing agent used for AOPs. (S. C. Ameta, 2018)

Table 2. Electrochemical Standard Oxidation Potential (EOP) of different oxidizing agents *(S. C. Ameta, 2018)*.

Oxidizing Agent	Electrochemical Oxidation Potential (EOP) (V vs. SCE)
Fluorine	3.06
Hydroxyl Radical	2.80
Atomic Oxygen	2.42
TiO_2 + UV	2.35
Ozone	2.08
Persulfate	2.01
Perbromate	1.85
Hydrogen Peroxide	1.78

2.1.1 Fenton Reaction

The Fenton reaction is described as the enhanced oxidative potential of H_2O_2, when iron is used as catalyst under acidic conditions described by Haber & Weiss (1932) in the following equations

$$Fe(II) + \ H_2O_2 \rightarrow Fe(III) + HO^- + HO \cdot \tag{1}$$

$$Organic\ Pollutant + HO \cdot \rightarrow Degraded\ Products \tag{2}$$
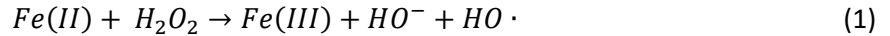
Besides the Fenton Reaction there are two types of Fenton-like reactions: i) Involves the use of other metals with many oxidation states such as copper in order to obtain the hydroxyl free radical (Nerud, Baldrian, Gabriel, & Ogbeifun, 2001) and ii) using other reagents such as the persulfate anions (Gligorovski, Strekowski, Barbati, & Vione, 2015). The Fenton-like reactions equations are presented in equation 3 and equation 4 respectively.

$$Cu(I) + \ H_2O_2 \rightarrow Cu(II) + HO^- + HO \cdot \tag{3}$$

$$Fe(II) + \ S_2O_8^{2-} \rightarrow Fe(III) + SO_4^{2-} + SO_4^{\cdot -} \tag{4}$$
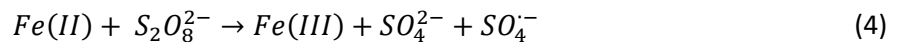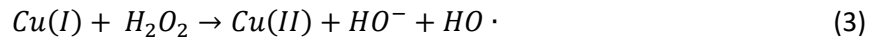
2.1.2 Photo-Fenton Reaction

When the hydrogen peroxide is combined with UV radiation and iron species (Fe^{2+} and Fe^{3+}), it is presented not only the traditional Fenton reaction presented in equation 1 but a regeneration of the Fe(III) to Fe(II) which is called photo-Fenton observed in equation 5.The combination of these two effects enhances the production of hydroxyl free radicals which consequently generates an enhancement of the degradation rate of the organic pollutants.

$$Fe(III) + \ H_2O + hv \rightarrow Fe(II) + H^+ + HO \cdot \tag{5}$$
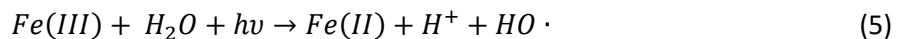
It is important to remark that the photo-Fenton process offers better performance at pH 3, this is due to the hydroxyl species are complexed the Fe (III) making them more soluble in water and more photoactive. (R. Ameta, Chohadia, Jain, & Punjabi, 2018)

2.1.3 Electro-Fenton

The electro-Fenton process, contrary to the previously Fenton reactions (presented in 2.1.1 and 2.1.2) is not focused in the hydroxyl radical generation but in generating hydrogen peroxide in-situ by a cathodic reduction of molecular oxygen (oxygen reduction reaction, see 2.2.1) that can react with iron species for the hydroxyl free radicals generation.(Le et al., 2015).

2.1.4 Photocatalysis

The photocatalysis effect is a phenomenon where light interacts with a semiconductor which generates a pair hole-electron (h-e) in the valence band (VB) and conduction band (CB) respectively. The energy difference between the valence band and the conduction band for semiconductors are usually between 1.5 eV and 3 eV (R. Ameta, Solanki, Benjamin, & Ameta, 2018) .

The excitation of the electron lead to the formation of the (h-e pair) on the surface of the catalyst and then two processes can happen: i) the recombination of charge carriers that were produced releasing energy in the form of heat and ii) the charge carriers react with an electron donor or an electron acceptor molecules on the surface of the catalyst.

In the case of the second event in wastewater treatment, the electron reacts with dissolved oxygen or the hole reacts with the water in order to form reactive oxidizing species ($O_2^{\cdot-}$, $\cdot OOH$, and $\cdot OH$) (R. Ameta, Solanki, Benjamin, & Ameta, 2018).

2.2 Hydrogen Peroxide Production

The hydrogen peroxide is one of the 100 most important chemicals, its production until the 1950 was by the electrolysis of sulfuric acid to obtain peroxydisulfate ion, water and hydrogen peroxide, however, the high cost of the electricity change the obtention pathway. Nowadays it is obtained by the anthraquinone oxidation process, this process requires palladium, platinum or nickel as catalyst to this process.

The world annual production of hydrogen peroxide is around 2.5 million tons, and it has many environmental applications, this include water treatment, odor control, oxidation of pollutants, and corrosion control. Currently there are attempts to develop new electrochemical methods cost-effective to commercialize the obtained hydrogen peroxide (Myers, 2007).

2.2.1 Oxygen Reduction Reaction

The oxygen reduction reaction (ORR) is one of the most important reactions, in aqueous solutions can occurs by two pathways: i) the four-electron pathway from molecular oxygen to water molecule (observed in equation 6), and ii) the two-electron pathway from molecular oxygen to hydrogen peroxide (observed in equation 7).

$$O_2 + 4e^- + 4H^+ \rightarrow 2H_2O \qquad\qquad E^0 = 1.229 \qquad (6)$$

$$O_2 + 2e^- + 2H^+ \rightarrow H_2O_2 \qquad\qquad E^0 = 0.70 \qquad (7)$$

To improve the reaction of the oxygen reduction reaction due to its slow kinetics a cathode catalyst is needed, the catalyst preferred is the platinum or the platinum based materials, however, these catalysts are too expensive for commercial applications. Non-metallic catalysts has been studied to improve the efficiency of the ORR and reducing the costs compared to Pt-based catalysts. (Song & Zhang, 2008)

The carbonaceous materials is an interesting alternative that has been studied in the last decade, these materials include graphite, graphene, carbon nanotubes, and nitrogen-doped carbon nanotubes.

2.3 Nitrogen-doped Carbon Nanotubes actives for ORR

The first time that was related the catalytic activity for the oxygen reduction reaction to the nitrogen sites in the carbon nanotube was done by Gong, Du, Xia, Durstock, & Dai (2009). They purified electrochemically their nitrogen doped carbon nanotubes (CNx) sample to get rid of most of the iron content present in the sample. They compared purified CNx (electrochemically purified) vs. unpurified CNx, the reason of this experiment was to attribute the ORR activity to the nitrogen sites or if the activity was due to the presence of Fe_2N-C and/or FeN_4-C, interestingly the purified CNx maintained the ORR activity (as shown in figure 1)
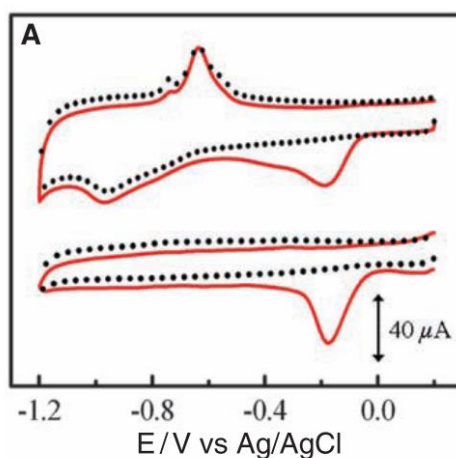
Figure 1. Comparison of the electrochemical activity of purified (red line) vs. unpurified CNx (black dots) (K. Gong et al., 2009).

They are non-aligned carbon nanotubes (NA-CNTs) without any doping and nitrogen doped carbon nanotubes (observed in figure 2A). It can be observed a shifting to a more positive potentials when the carbon nanotubes presented the doping. Furthermore, the most notorious oxidation of hydrogen peroxide was obtained by the NA-CNTs oppositely the NA-CNx did not present almost any oxidation (see the ring section of figure 2A). These experiments proved that the nitrogen sites are the active sites for the ORR, but they did not differentiate between the different nitrogen species present in carbon nanostructures.
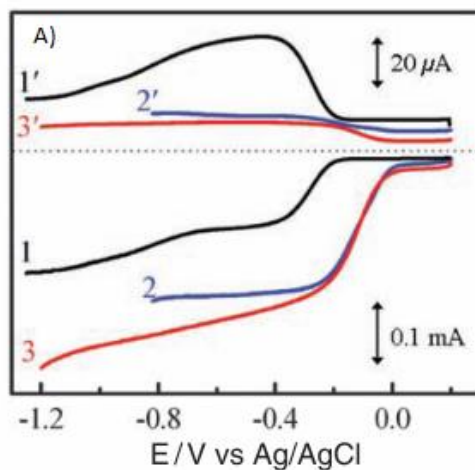
Figure 2. A) Electrochemical activity measured by the rotating-ring disk electrode of non-aligned CNTs(1), Pt-C/GC (2), and non-aligned CNx (3) (K. Gong et al., 2009).

A more profound description of nitrogen-doped carbonaceous materials either structure as active sites are described in chapter 5.

2.4 Buckypapers

Buckypapers is a macroscopic membrane of carbon nanotubes in a randomly dispersed or vertically aligned arrangement. The first time reported was by Rinzler et al. (1998) which dispersed SWCNT using alcohols and surfactants under ultrasonic bath and finally after the purification of the dispersed material they obtained the buckypapers by a vacuum filtering system.

The buckypapers gained attention by the results obtained by Endo et al., (2005) when they obtained a flexible and mechanically stable buckypapers made of double-walled carbon nanotubes as observed in figure 3A and figure 3B.
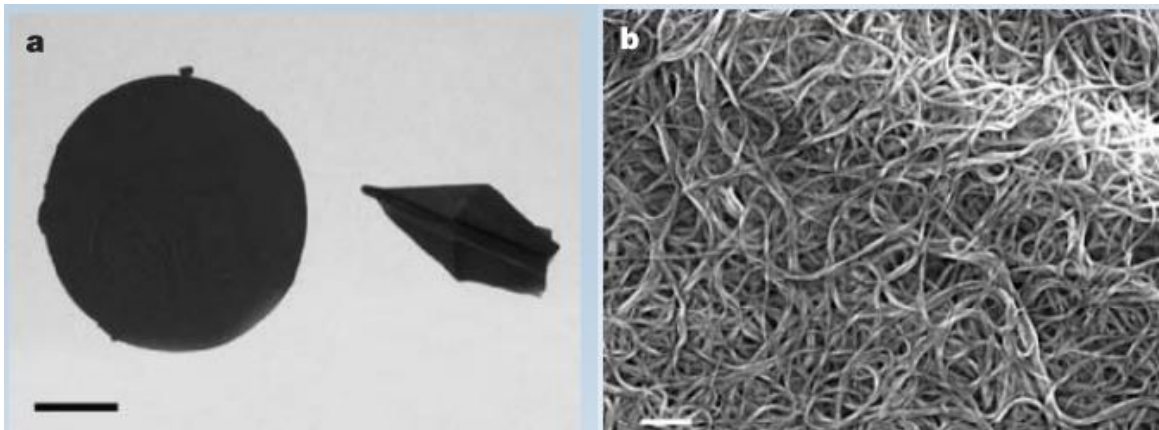
Figure 3. Macroscopic image of a buckypaper showing its flexibility (A), and a SEM image of the buckypaper showing entanglement of nanotubes (Endo et al., 2005).

In this sense, many methodologies have been described to obtain buckypapers, among them, the most important are: i) electrophoretic deposition methodology by appling a voltage of 2.8 V between a pair of electrodes in an aqueous MWCNT@surfactant dispersion during 5 minutes Rigueur, Hasan, Mahajan, & Dickerson (2010); ii) domino pushing methodology was obtained synthesizing vertically-aligned MWCNTs which were mechanically arrayed down by a pushing cylinder and peeled off from the substrate membrane Wang, Song, Liu, Wu, & Fan (2008); and iii) the vacuum assisted methodology which consisted in the dispersion of carbon nanotubes and vacuum filtering the solution onto a PFTE membrane Rinzler et al., (1998).

For the vacuum assisted methodology, the dispersion is a key-role to obtained good quality buckypapers, therefore, Alvizo-Paez et al. (2008) obtained a soft methodology (called hydrothermic treatment) for dispersing the carbon nanotubes without surfactants in polar solutions. They used mechanical forces instead of chemical treatments to avoid or minimize the structural damage or chemical functionalizations which can alter the nanotube surface, then, the methodology maintained the original physical and chemical properties of the nanotubes.

Following these methodologies, the best results obtained in the masters research of Contreras in 2015 were using 50 mg of soot with 1.6 L of deionized water and using an ultrasonic probe for 5 hours under boiling temperature, and finally the obtained dispersion is vacuum filtered

Chapter 3. Main Issue (Problem Statement)

The treated wastewater in the Baja California region is highly polluted; it has been observed a large quantity of organic matter reported by (Melgar-Lopez & Cambreros-Urbina, 2017). Therefore, it is needed to add an extra step after the third process of wastewater cleaning.

In this sense, buckypapers made of nitrogen-doped carbon nanotubes can be used as a novel technology, exploiting their physicochemical properties, and taking advantage of the macroscopic handling and flexibility advantages of this material.

In this work it is proposed to develop a macroscopic membrane based on nitrogen-doped carbon nanotubes that takes advantage of its nanometric properties for its application in the improvement of the quality of the recovered water from treatment plants. This material is intended to improve the electrocatalytic oxygen reduction reaction and the consequent generation of the electro-Fenton process, to remove the organic matter remaining in water from the recovered wastewater from Tijuana City.

3.1 Hypothesis

The carbon nanotubes doped with nitrogen will promote the oxygen reduction reaction (ORR), aiding in the in-situ generation of hydrogen peroxide. This will allow the reduction of recalcitrant organic matter from the tertiary phase of the reclaimed water, using buckypapers electrodes assembled with nitrogen-doped carbon nanotubes.

3.2 Objectives

3.2.1 General Objective

The study the carbon nanotubes doped with nitrogen (CNx) in the oxygen reduction reaction and how their response can benefit for the cleaning of reclaimed water from the tertiary wastewater process.

Furthermore, the assembly of the synthesized CNx in a manipulable macroscopic membrane (buckypaper) which will allow having the core of a prototype reactor for cleaning reclaimed water.

3.2.2 Particular Objectives

1) To evaluate and optimize the conditions for the synthesis of carbon nanotubes doped with nitrogen.

2) To obtain the synthesis parameters of carbon nanotubes that favor a higher production of H_2O_2 through the ORR.

3) To generate, evaluate, and optimize the electro-Fenton reaction using the CNx.

4) To assemble buckypapers with nitrogen-doped nanotubes obtained from the optimal synthesis parameters.

5) To test with water samples from the tertiary phase in vitro using the buckypapers obtained.

6) To design and obtain reactive membranes (nanoadsorbents, nanofiltrants, and electrocatalytic) to integrate it into a prototype reactor that improves the water quality of the reclaimed water of Tijuana City.

7) To test the prototype reactor obtained in situ with water from the tertiary phase of wastewater treatment.

Chapter 4. Methodology

4.1 Characterization Methods

4.1.1 Scanning Electron Microscopy (SEM)

The SEM microscopy was done with Israel Gradilla, a technician of the UNaC (Unidad de NanoCaracterización) in CNyN using the the JEOL JSM-5300. The sample preparation was done placing the material on carbon tape over a sample holder.

4.1.2 Transmission Electron Microscopy (TEM)

The TEM microscopy was done in the UNaC in CNyN using the the JEOL JEM 2010. The sample preparation was done by preparing TEM grids.

- The carbon nanotubes TEM grid was prepared dispersing CNTs to obtain a light gray solution, then a couple of drops was applied over a lacey carbon tem grid (hint: the TEM grid was over a filter paper).

- The magnetite TEM grid required a more elaborated process, it was prepared a magnetite dispersion of 88 µM of magnetite (to prevent the nanoparticles could contaminate the lens) in water, and one drop was placed over a TEM grid (hint: the TEM grid was over parafilm).

4.1.3 X-Ray Photoelectron Spectroscopy (XPS)

The XPS was done with David Dominguez, technician of the XPS-SPECS device. obtained CNx soot samples were deposited on a carbon tape over a molybdenum sample holder and placed in a UHV chamber to eliminate water, solvents, and volatile species for 12 h, reaching a vacuum of $7 \times 10{-}10$ Torr. Spectra were obtained at a pressure of 1×10^{-9} Torr using an X-ray source of Al K_α (1486.71 eV) and a Phoibos 150 WAL hemispherical analyzer in the constant pass energy mode (Epass = 50 eV).

4.1.4 Cyclic Voltammetry (CV)

The cyclic voltammetry (CV) was performed using an Autolab potentiostat PGSTAT302N. Three-electrode cell arrangement was used; the glassy carbon, platinum electrode, and Ag/AgCl reference electrode were purchased from BASi. Two different solutions were used as mediums for the ORR evaluation. First a basic solution (pH=13) consisting of a 0.1 M KOH solution; and a second, a simulated reclaimed water (5 mM $CaCl_2$, 5 mM $MgCl_2$, 1 mM KNO_3 and 1 mM NH_4NO_3 solution; pH=7).

The ORR was evaluated in two different environments: alkaline (pH=13) and neutral (pH=7). The solutions first were saturated with an inert gas (Argon) for 10 minutes to discriminate other signals not related with the ORR, later the solution was saturated with oxygen for 10 minutes before each measurement to analyze the ORR activity. The CV was performed at a scan rate of 100 mV/s.

The obtained results were displayed against the reversible hydrogen electrode (RHE) according to the Nernst equation (equation 8).

$$E_{RHE} = E_{Ag/AgCl} + 0.059pH + E^0_{Ag/AgCl} \qquad (8)$$

The onset potential from the CV curves were determined at the inflection point of the segment in between the highest potential value and the minimum peak of the graph. Those points were obtained by taking the first derivative curve of the graph and locating the maximum (i.e. the point where the slope of the graph changes from being increasing to start decreasing) for each voltammogram.

4.1.5 Rotating Disk Electrode Voltammetry (RDE)

The linear sweep voltammetry (LSV) was performed connected to a rotating disk electrode (RDE). Using an Autolab potentiostat PGSTAT302N. Three-electrode cell arrangement was used; the glassy carbon, platinum electrode, and Ag/AgCl reference electrode were purchased from BASi. Two different solutions were used as mediums for the ORR evaluation. First a basic solution (pH=13) consisting of a 0.1 M KOH solution; and a second, a simulated reclaimed water (5 mM $CaCl_2$, 5 mM $MgCl_2$, 1 mM KNO_3 and 1 mM NH_4NO_3 solution; pH=7).

The ORR was evaluated in two different environments: alkaline (pH=13) and neutral (pH=7). The solutions first were saturated with an inert gas (Argon) for 10 minutes to discriminate other signals not related with the ORR, later the solution was saturated with oxygen for 10 minutes before each measurement to analyze the ORR activity. The LSV with RDE were performed at 10 mV/s with rotation speeds varied from 100 rpm to 1600 rpm.The obtained results were displayed against the reversible hydrogen electrode (RHE) according to the Nernst equation (equation 8), and the onset potential was calculated according to section 4.1.4 .

4.1.6 Raman Spectroscopy

The Raman spectroscopy was obtained using a Horiba XploRA, by simply placing the sample over a glass slide. However the best conditions obtained (in the hardware toolbar section) for the measurement was using the green laser (532 nm), the used filter was the 100%, a confocal hole of 500 μm, a slit 200 μm, and a diffraction grating of 600 grooves/mm.

4.1.7 Thermal-Gravimetric Analysis (TGA)

The Thermal-Gravimetric Analysis was performed using a SDT-Q600 analyzer, following the next steps: i) open the chamber to tare the clean empty pan, ii) add the desired sample to the pan taking caution of fill just the working pan and not the reference pan, iii) close the chamber. After adding the temperature parameters, temperature ramp, and the selected gases just click start.

4.1.8 Dynamic Light Scattering (DLS)

Before to start the DLS measurement it is important to create a SOP file, to do this in the file section we selected the New SOP and fill the following sections: i) material (if it is not in the manager select add new material and add the refractive index of this material (Fe_3O_4 n=2.3; MWCNT n=2.5)), ii) select the solvent used in the dispersant section, and iii) the cuvette used for this measurement (in this case the DTS0012 was used).

The measurement was done, the cuvette is filled with the sample, and then in the software is selected new measurement, open an existing SOP, select the file and just click start.

4.1.9 Zeta Potential

Before to start the Zeta potential measurement it is important to create a SOP file, to do this in the file section we selected the New SOP and fill the following sections: i) material (if it is not in the manager select add new material and add the refractive index of this material (Fe_3O_4 n=2.3; MWCNT n=2.5)), ii) select the solvent used in the dispersant section, and iii) the cuvette used for this measurement (in this case the DTS1070 was used).

The measurement was done, the cuvette is filled with the sample, and then in the software is selected new measurement, open an existing SOP, select the file and just click start.

4.1.10 Ultraviolet-Visible Spectroscopy

The UV-Visible spectra was obtained using a spectrometer Agilent Cary 60, the measurement was done by the following steps: i) In the software section select the setup to select the wavelength range, speed and select baseline correction, ii) add the selected solvent into the quartz cell and select baseline in order to correct the following measurements, and iii) add the sample to the quartz cell and click start.

4.1.11 Fluorescence Spectroscopy

The fluorescence spectroscopy was measured using a HORIBA Aqualog. The measurement is almost straight forward as the UV-Visible spectroscopy by following the next steps: i) add the water sample to the quartz cell and placed into the aqualog, ii) in the Aqualog Software select H_2O and select the option 3D, iii) select blank only and select run the experiment, iv) when the result is displayed select "inner-filter effect", v) then select the Rayleigh Masking, vi) after that DO NOT NORMALIZE in order to follow degradation experiments, and vii) select EEM button.

4.1.12 Chemical Oxygen Demand

The chemical oxygen demand (COD) was performed adding to the digestion vials 2 mL of deionized water (as blank) and 2 mL of the sample water. All the vials were placed in the preheated reactor (150 °C for two hours), after that the reactor is cooled down to 120 °C for 20 minutes and then the vials can be retired from the reactor and waited for two hours before the measurement.

The digested samples were measured using a HACH DR 870/880 colorimeter (the program code for high range COD is the PRGM17). The blank vial is placed in the colorimeter and set as zero and removed, the samples were measured placing them into the colorimeter and just selecting read, the value of the COD is displayed in the screen.

4.1.13 Total Organic Carbon

The preparation of the sample for the total organic carbon (COD) measurement was done by following the next steps: i) add to 10 mL of water sample 0.4 mL of standardized sulfate buffer solution (pH 2.0), ii) open two TOC vials (one for the blank and the second one for the sample), iii) add TOC persulfate powder pillows to each vial, iv) add to the vials 1.0 mL of the deionized water (for the blank) and 1.0 mL of the water solution to the another vial, v) clean the indicator blue ampule with deionized water place into the vial and then the ampule is opened, and vi) close the vial.

All the vials were placed in the preheated reactor (105 °C for two hours), after that the vials can be retired from the reactor and waited for two hours before for the measurement.

The samples were measured using a HACH DR 870/880 colorimeter (the program code for low range TOC is the PRGM117). The blank vial is placed in the colorimeter and set as zero and removed, the samples were measured placing them into the colorimeter and just selecting read, the value of the TOC is displayed in the screen.

4.2 Buckypaper Fabrication

A dispersion of 50 mg of CNx-soot in water was prepared by a hydrothermal process. Briefly, a 20 kHz ultrasonic probe is used for 5 hours at boiling temperature under magnetic stirring to disperse the carbon nanotubes. The main purpose being to disperse completely the forest-like arrays of CNx coming inherently from the synthesis. Afterward, the solution is concentrated until reaching 0.5 mg/mL. Finally, the dispersion is vacuum-filtered to assembly the dispersed CNx into a membrane (buckypaper). The experimental arrangement is shown in figure 4 in the supplementary information.

Figure 4a and 4b are representations of either hydrothermal process and vacuum filtering process to make the nitrogen-doped carbon nanotubes dispersions and the buckypapers. Figure 4c and 4d are real images of the hydrothermal process. For the hydrothermal process (HTP) we used 50 mg of carbon nanotubes in 1.7 L of DI water, as observed in figure 4e, CNTs can barely be seen. After the 5 hours of HTP, it is observed a colored black dispersion shown in figure 4f and 4g. Finally, after the HTP we proceed to vacuum filter the blackish solution obtaining the buckypaper shown in figure 4h.
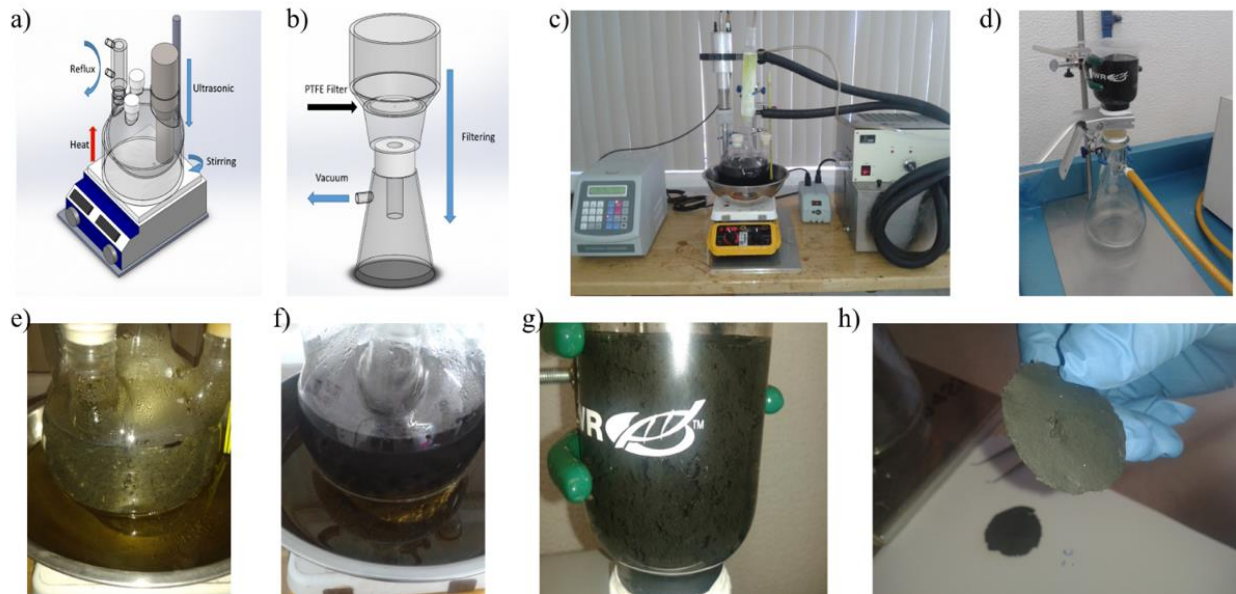
Figure 4. Hydrothermal process steps for the buckypaper fabrication (Contreras et al., 2019).

Chapter 5. Results and Discussion

5.1 In-situ H2O2 generation by Oxygen Reduction Reaction with Nitrogen-doped Carbon Nanotubes

5.1.1 State of the Art

5.1.1.1 Nitrogen-doped carbonaceous materials

The last two decades, there has been an increasing interest in the nitrogen-doped carbonaceous materials, since they present interesting physicochemical properties for different applications, in this section we will discuss about the different types of carbonaceous materials and how they had been developed thru the years.

One of the first reports of doping carbonaceous materials with nitrogen atoms was the article presented by Terrones et al., (1999) fabricating nitrogen-doped carbon nanofibers for enhancing the electronic properties using the graphitic-like nitrogen sites. Also, Han et al., (2000) proposed a mechanism for the synthesis of vertically aligned nitrogen-doped carbon nanotubes observing the bamboo-shape.

 Bhattacharyya et al. (2001) fabricated diamond doped with nitrogen, aimed to use the nitrogen atoms as *n-type* doping for conductive intracrystalline diamond films. Czerw et al., (2001) identified the pyridine nitrogen as the specie that lead the metallic behavior to the nitrogen-doped carbon nanotubes.

Later, it was reported that oxygen can be reduced by nitrogen doping in graphite structures Sidik, Anderson, Subramanian, Kumaraguru, & Popov, (2006). They demonstrated that the oxygen reduction reaction took place at lower energies in the nitrogen-doped graphite and theoretical calculations showed that oxygen was chemisorbed by alpha carbon to the graphitic nitrogen.

Lim et al. (2006) synthesized nitrogen-doped carbon nanotubes for electrical applications, using the idea of Bhattacharyya et al. 2001, tuning the electrical properties of the carbon nanotube by the introduction of nitrogen dopants. Sumpter et al., (2007) demonstrated a mechanism for the synthesis of nitrogen-doped carbon nanotubes, and explained that the nitrogen content is responsible for the characteristic bamboo-shape. Ismagilov et al. (2009) synthesized nitrogen-doped carbon fibers (CNF) to study their

electrical properties; the substitutional nitrogen atoms in the graphite matrix are electron donors which promoted the n-type conductivity in the carbon fiber.

It was until the study of Gong, Du, Xia, Durstock, & Dai (2009) when they started the area of metal free electrocatalysis observing that nitrogen doping in the carbon nanotubes promoted the oxygen reduction reaction (ORR) similar to the platinum without its disadvantages. Besides, Qu, Liu, Baek, & Dai (2010) obtained nitrogen-doped graphene by CVD synthesis using methane and ammonia. They observed similar results for the oxygen reduction reaction as the presented by Gong *et al*. (2009).

The ORR is a key-reaction for different applications such as batteries, fuel cells and biosensors. Thereafter, numerous research groups started to explore the ORR using metal free electrocatalysts.

Wu et al. (2012) took the idea of the Dai research group and extrapolated to a 3D electrode made by nitrogen-doped graphene aerogel decorated with magnetite, they observed good results for the ORR, but observing that their 3D electrode presented both pathways (the 4-electron pathway and the 2-electron pathway) of oxygen reduction reaction.

Fellinger, Hasché, Strasser, & Antonietti, (2012) also synthesized a 3D electrode but it was made of mesoporous nitrogen-doped carbon, however, contrary to the results presented by Wu et al. 2012, they observed a selectively two electron pathway ORR.

It is remarkable to state that the previous studies did not completely prove which nitrogen specie was the catalytically active for the ORR, especially for the four-electron pathway (we will discuss about that in section 5.1.1.3).

5.1.1.2 Catalytic sites of the Nitrogen-doped Carbonaceous Materials

The nitrogen can dope the carbonaceous materials (in the scheme observed in figure 5 gray balls represent carbon atoms, blue balls represent nitrogen atoms, white balls represent hydrogen atoms and pink balls represent non-resonant pair of electrons principally in three different species, pyridinic Nitrogen, graphitic Nitrogen, and pyrrolic Nitrogen):

- Pyridinic Nitrogen is sp^2 hybridized bonded to two sp^2 hybridized carbon atoms and it also has a lone pair of electrons in a sp^2 orbital perpendicular to the p orbitals. The pyridinic Nitrogen enter into resonance due to a lone electron in a p orbital forming pi orbitals (figure 5 dashed-blue circles).

- Graphitic Nitrogen specie is sp^2 hybridized bonded to three sp^2 hybridized carbon atoms presenting a 120° of separation between them, it is also observed that it does not show the lone pair of electrons, this is due to the lone pairs are in a p orbital and entered into resonance to the aromatic system (figure 5 dashed-red circles).

- Pyrrolic Nitrogen specie is sp^2 hybridized bonded to two sp^2 hybridized carbon atoms (from a pentagon in the sp^2 carbon network) and a hydrogen atom. It enters to resonance due to a lone electron in a p orbital forming pi orbitals (figure 5 dashed-black circles).
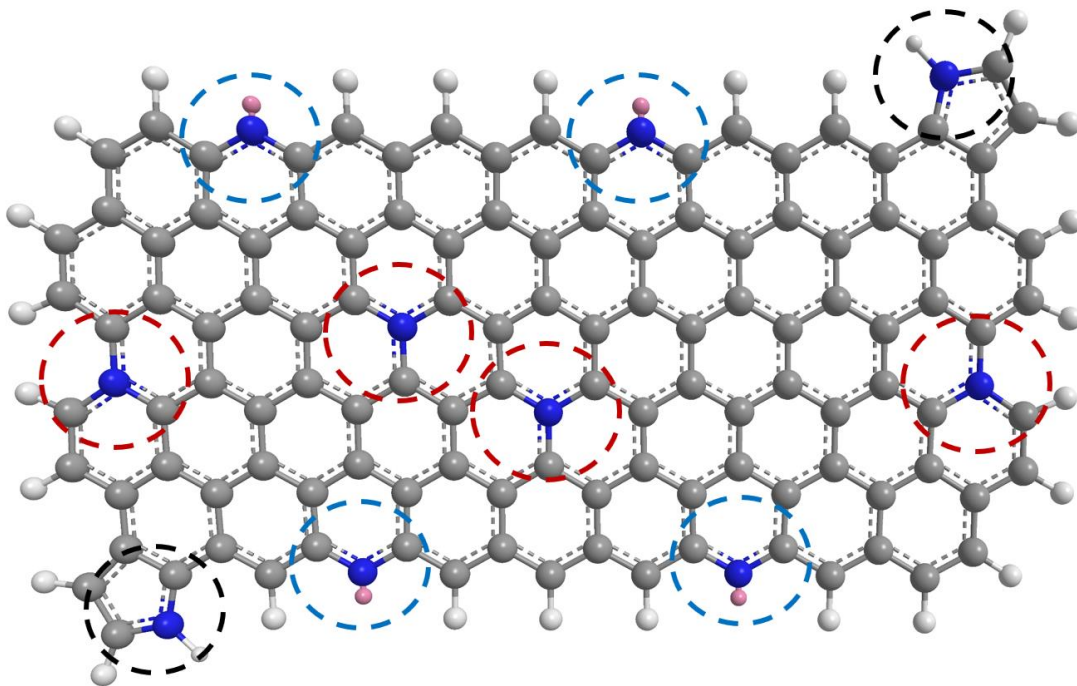
Figure 5. Nitrogen-doped graphene with pyridinic Nitrogen (dashed-blue circle, pyrrolic Nitrogen (dashed-black circle and graphitic Nitrogen (dashed-red circle).

The differences between the three nitrogen species are explained by two different theories: valence bond theory (VBT) and molecular orbital theory (MOT). In order to understand their chemical differences and as background for further reaction mechanism models.

The electron configuration for the nitrogen is [He] $2s^2$ $2p^3$. Therefore, it is needed three more electrons to fill the octet, and it is not observed an orthogonal geometry between the bonds. The geometry is explained by VBT hybridizing the atomic nitrogen orbitals (as observed in figure 6).
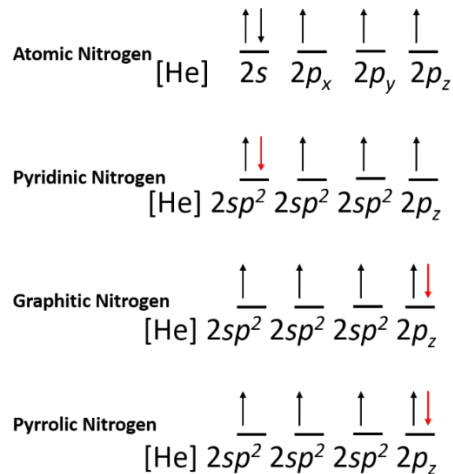
Figure 6. Electronic configuration of the Nitrogen species.

As observed in figure 6, it is needed a sp^2 hybridized nitrogen for solving the geometry issue, forming 3 new sp^2 orbitals and left one p orbital. However, the energy levels of the orbitals are degenerated, the Hund´s rule permit to pair electrons into a sp^2 orbital or p_z orbital (this is observed by the red arrow).

Comparing the electronic configuration of the three different species observed in figure 6 with the nitrogen-doped graphene model of figure 5, we can observe that pyridinic nitrogen presented a lone pair of electrons in a sp^2 orbital perpendicular to the p orbitals (represented by a pink ball), therefore these electrons cannot enter into resonance. The lone pair of electrons in the graphitic nitrogen and pyrrolic nitrogen is not observed in figure 6, it is due to the electron pair entered into resonance because the pair is in a p_z orbital.

The VBT cannot explain the difference between graphitic nitrogen and pyrrolic nitrogen, therefore, to complete the chemical understanding of the nitrogen species is used the molecular orbital theory (MOT).

Figure 7 shows the MOT for the three different species (as presented by J Robertson in 1995). Similar to the VBT, the MOT shows two sigma bonding to carbon atoms, one pair of non-bonding electrons and an electron into resonance in a π bonding.
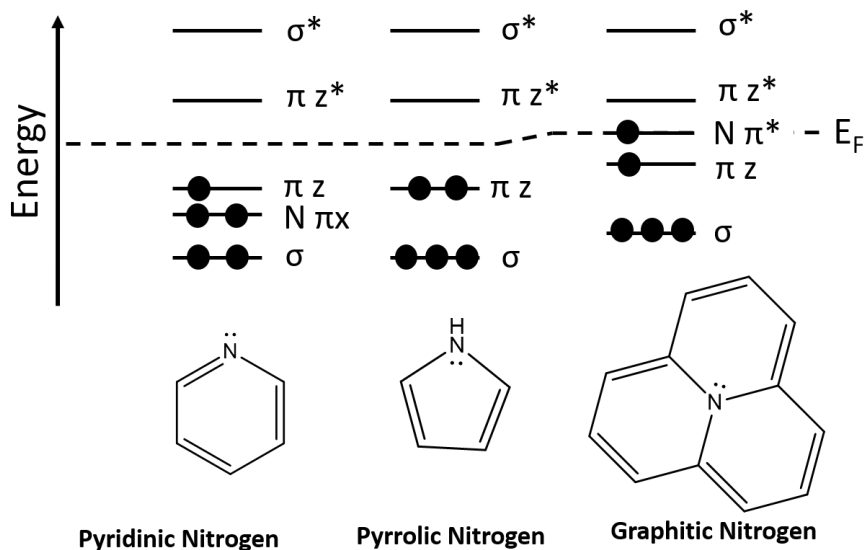
Figure 7. Energy diagram of the molecular orbitals of the Nitrogen species.

Figure 6 shows that pyrrolic nitrogen and graphitic nitrogen presents a pair of electrons in a pz orbital, however MOT presents the difference between these two species. The pyrrolic nitrogen presents its pair into a πz bonding permitting them to enter into resonance. Graphitic nitrogen presents a lone electron in an antibonding π and another lone electron in a πz, it permits just one electron enter into resonance while the second one remains in the nitrogen.

5.1.1.3 Oxygen Reduction Reaction activity in the Carbonaceous Materials

It is important to understand the oxygen reduction reaction; the ORR is a catalytic reaction where the molecular oxygen is reduced to form either hydrogen peroxide or two water molecules at different electric potential applied.

The equation 6 (known as the four-electron pathway, presented in 2.2.1) is usually considered the most important, due to its high reduction potential which make this reaction ideal for galvanic cell applications, while the equation 7 (known as the two-electron pathway, presented in 2.2.1) is usually considered an undesirable reaction due to its relatively low reduction potential compared to the 4-electron pathway reduction potential.

As previously discussed in the last two sections, we can summarize them in two key-points:

1) It is not clear which nitrogen site is the catalytically active for the oxygen reduction reaction.

2) The three nitrogen species present different chemical properties as shown either by VBT and MOT, which can unravel the catalytic activity of each nitrogen.

The non-metallic electrocatalyst research gained momentum when Guo et al., (2016) selectively doped with nitrogen highly oriented pyrolytic graphite (HOPG) with pyridinic nitrogen and/or graphitic nitrogen (see figure 8A). Their observations allowed them to observe that the pyridinic nitrogen is catalytic active for four-electron pathway, a desirable reaction for fuel cells applications.

To observe the nitrogen species contribution, they prepared four samples and tested for the ORR in acidic media. Clean-HOPG which is highly oriented pyrolytic graphite, edge-HOPG which is the HOPG edge patterned with Ar^+ etching, graph-HOPG which is HOPG doped with graphitic nitrogen by doping implanting N^+, and pyri-HOPG which is doped with pyridinic nitrogen harnessing the high edges density by treating with NH_3. The nitrogen species were measured by XPS (see figure 8A)

As observed in figure 8B the samples without nitrogen contribution presented the ORR onset (the onset potential was calculated at 1 µA/cm2, shown in light blue dashed line of figure 8B) at 0.06 V vs. RHE while the grap-HOPG was upshifted at 0.22 V vs. RHE and pyri-HOPG presented the higher upshifting at 0.38 V vs. RHE. It suggested that pyridinic Nitrogen are more catalytic than graphitic Nitrogen for the ORR. It is

clearly observed that the reduction potentials are far from the standard reduction potential (observed in equation 6 and 7).
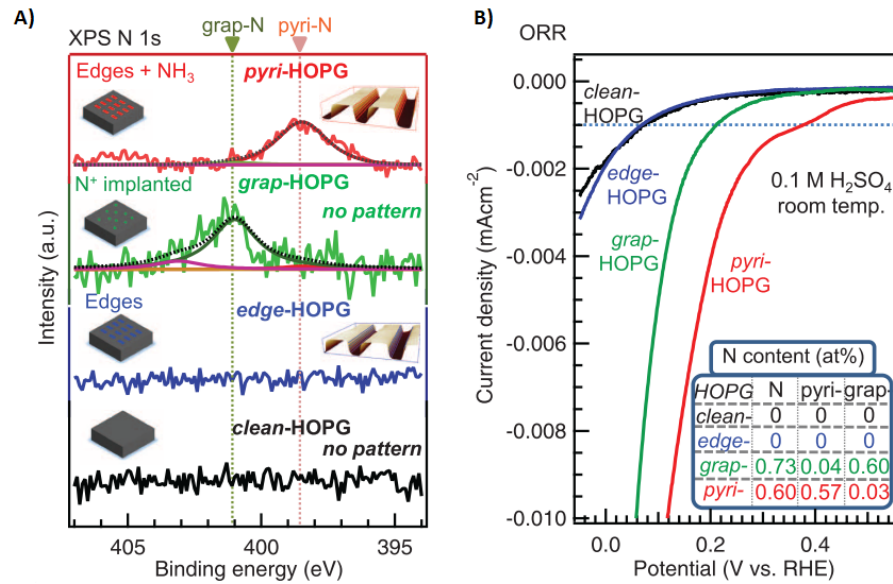
Figure 8. The unraveling of the pyridinic nitrogen specie for the four-electron pathway a) shows the HOPG with different nitrogen species and b) shows an linear scan voltammetry for the ORR observing the shifting of the HOPG with pyridinic nitrogen enchanced (image taken from Guo et al., (2016)).

Further, Guo et al. made nitrogen-doped graphene nanosheets, increasing the pyridinic nitrogen content (as observed in figure 9A). The increase in pyridinic nitrogen had a response shifting the onset potential (observed in figure 9B) to a more positive value. The higher the pyridinic nitrogen concentration the closer to the standard reduction potential of the 4-electron pathway ORR (value presented in equation 6).
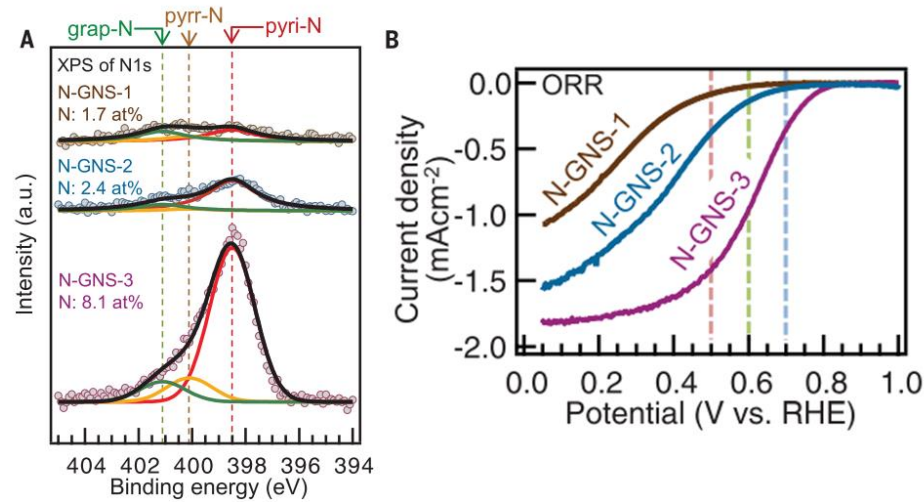
Figure 9. A) shows the XPS observing the enhancement of the pyridinic nitrogen in the graphene nanosheet, and B) shows the respective LSV presenting a shifting to more positive potentials while was incremented the pyridinic nitrogen (image taken from Guo et al., (2016)).

This result allowed them to propose a mechanism for the ORR where the alpha carbon to the pyridinic nitrogen acts as a Lewis base donating electron. Figure 10 shows the proposed mechanism, starting by bonding a singlet diatomic oxygen to the alpha carbon to the pyridinic nitrogen, then it was supplied a proton and electron to form an hydroperoxide molecule anchored to the carbonaceous material. It is a crucial point where the reaction can be guided to the two-electron pathway (by the addition of one proton and one electron) or the four electron pathway (adding two electrons and two protons to release one molecule of water and further the addition of one proton and one electron to release the second water molecule).
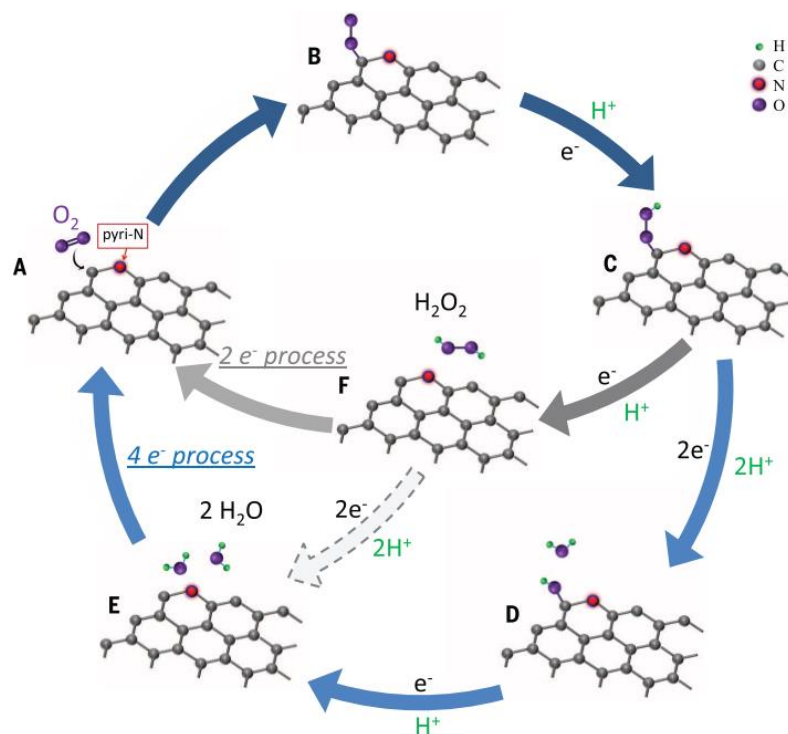
Figure 10. Proposed mechanism for either the two-electron pathway as the four-electron pathway (image taken from Guo et al., (2016)).

Iglesias et al., (2018) synthesized nitrogen-doped nanohorns. It was oxidizing previously obtained nanohorns with nitric acid and wrapping them with polydopamine and a final annealing at 700°C under intert environment (as shown in figure 11).
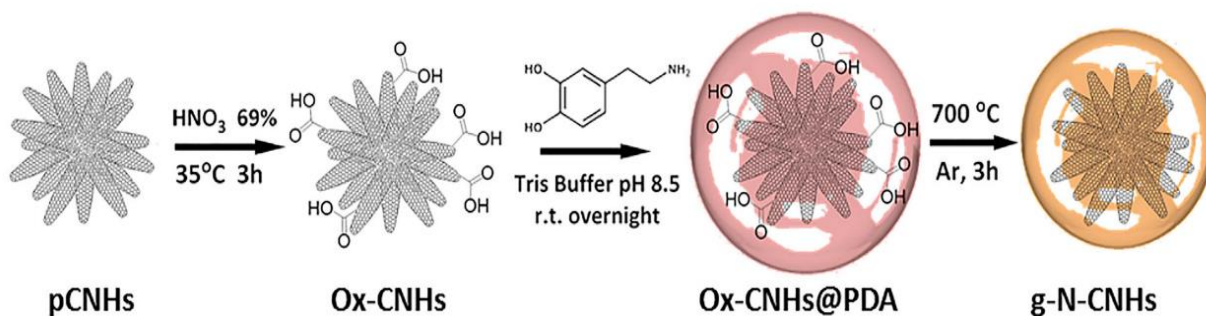
Figure 11. Synthesis of the nitrogen-doped Nanohorns (image taken from Iglesias et al., (2018)).

The nitrogen-doped nanohorns were analyzed by XPS analysis where they observed a bigger contribution of N-C species. Iglesias et al. identify this specie as pyrrolic nitrogen (however as previously presented in figure 5, there are two N-C species) as observed in figure 12.
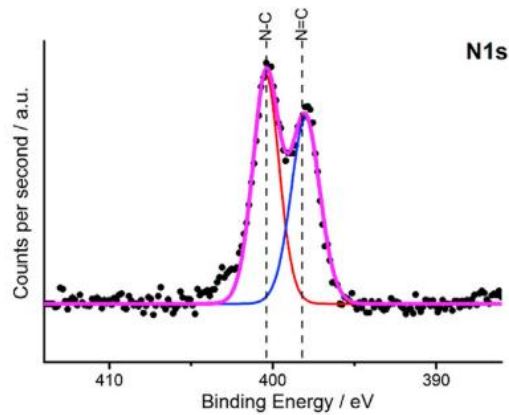
Figure 12. XPS of the nitrogen-doped Nanohorns (image taken from Iglesias et al., (2018)).

The oxygen reduction reaction evaluation was done under three different media: acidic (red line), neutral (green line), and alkaline (blue line) as presented in figure 13A. It is observed that the N-NHs has more affinity to the ORR under alkaline media (the onset closer to the 0.71 V vs. RHE similar to the standard reduction potential showed in equation 7) follow by the neutral media (onset at approximately 0.53 V vs. RHE) and the last one was the acidic media (onset at approximately 0.40 V vs. RHE).
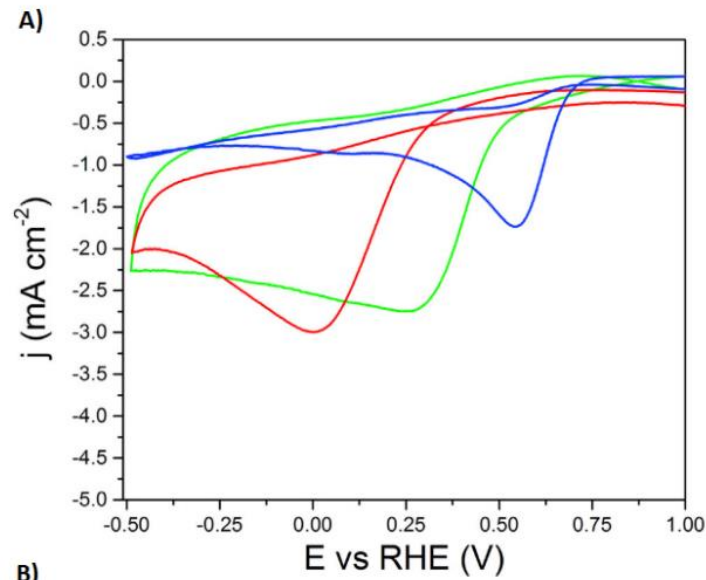
Figure 13. A) Cyclic voltammetry of the nitrogen-doped Nanohorns at different media (blue is in alkaline media, green in neutral media and red at acidic media), and B) The respective values of the cyclic voltammetry (image taken from Iglesias et al., (2018)).

Figure 13B shows the obtained values of the LSV-RRDE (Linear Sweep Voltammetry-Rotating Ring Disk Electrode), where it is shown the number of transferred electrons per catalytic site, the N-NHs at different three medias shown closer Ne- to two electrons proving the reaction went to the two-electron pathway producing hydrogen peroxide. As previously shown in figure 12, it can be assumed that the N-C is the catalytic active site for the two-electron pathway.

5.1.2 Synthesis of Nitrogen-doped Carbon Nanotubes

The nitrogen doped CNTs were synthesized using chemical vapor deposition (CVD) by the spray pyrolysis technique (see figure 14). 10 mL of a 2.5 wt% solution of Ferrocene in Benzylamine was used as the precursor. The Benzylamine acts as the source of carbon and nitrogen atoms; while the Fe from the

ferrocene generates Fe nanoparticles to promote the CNx growth as described by Sumpter et al., (2007). The precursor solution was sprayed by a pneumatic nebulizer and the aerosol generated was carried by a 4 L/min Argon flow into a quartz tube until the solution was over (~50 minutes). Once the synthesis is finished, the black soot grown on the quartz tube is mechanically collected. Five different samples were obtained when changing the reaction temperature: 800 °C, 825 °C, 850 °C, 875 °C and 900 °C; to modify the nitrogen doping species in the synthesized CNTs.
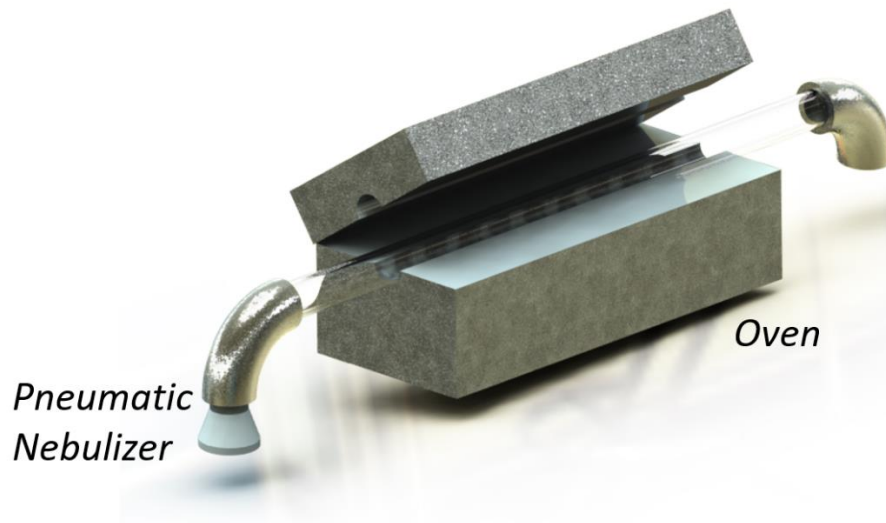
Figure 14. Chemical Vapor Deposition system

The soot obtained from the CVD synthesis reveals nanotubes in forest-like arrays as shown by SEM micrographs (figure15a and 15b); higher magnifications micrographs achieved by TEM reveal bamboo-shape nanotubes (figure 15c), a structure typical of nitrogen-doped carbon nanotubes (Sumpter et al., 2007). In order to ensure the nitrogen presence, we measured EDXS (Energy Dispersive X-rays Spectroscopy) mapping with a TEM in STEM (Scanning Transmission Electron Microscopy) mode (see figure 16). The Nitrogen map reveals nitrogen signal from the carbon nanotubes locations proving the nitrogen doping along the carbon nanotubes.
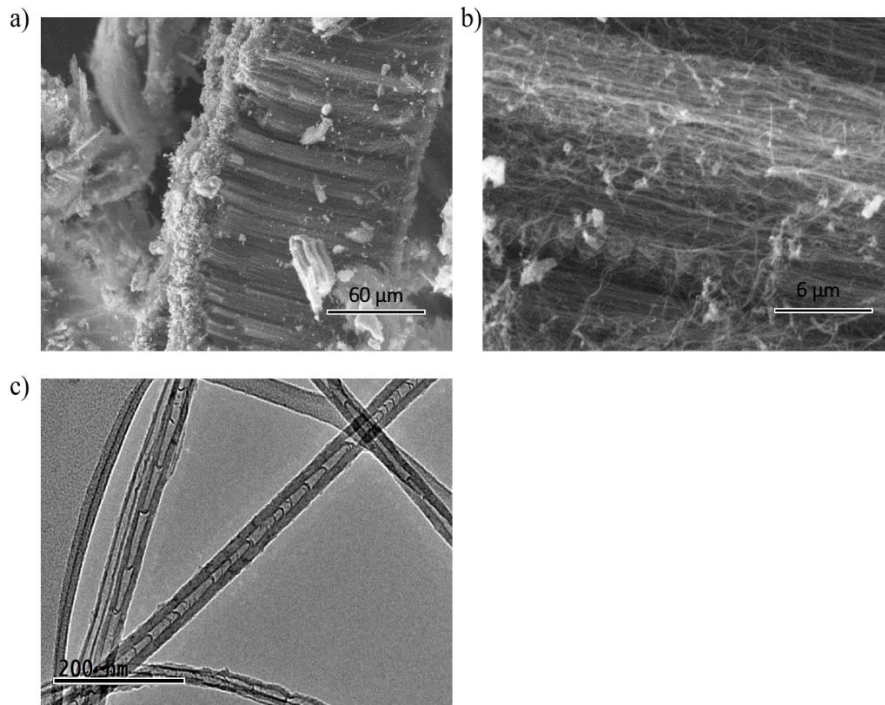
Figure 15. a) and b) are SEM images where it can be observed the forest-like arrays at 500X and 5000X respectively and c) is a TEM micrograph where it can be observed the bamboo structure typical of the CNx.
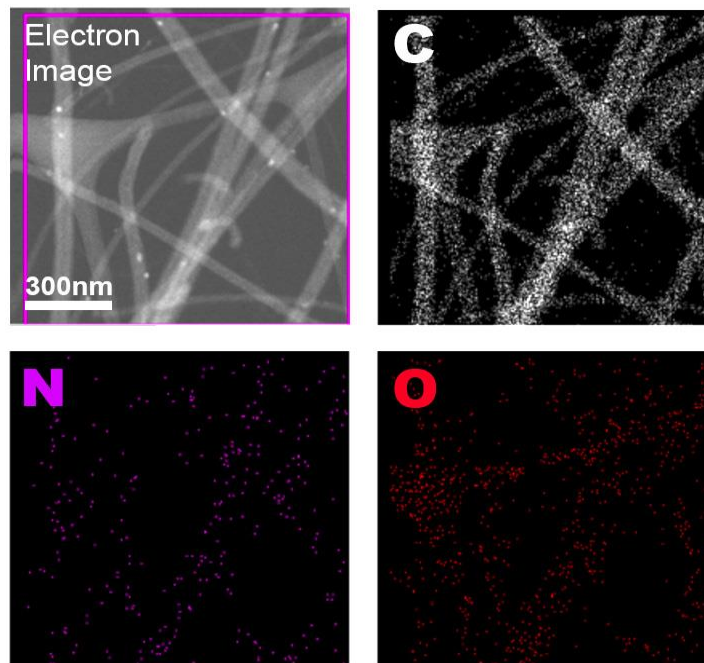
Figure 16. EDXS mapping from the CNx-900C sample taken in STEM mode using a TEM. HAADF image and Maps from Carbon, Oxygen and Nitrogen signal are presented

The samples synthesized at 800 °C, 825 °C, 850 °C, 875 °C and 900 °C were characterized by XPS to evaluate the nitrogen content and the variations in the nitrogen species due to the synthesis temperature (as presented in figure 17).
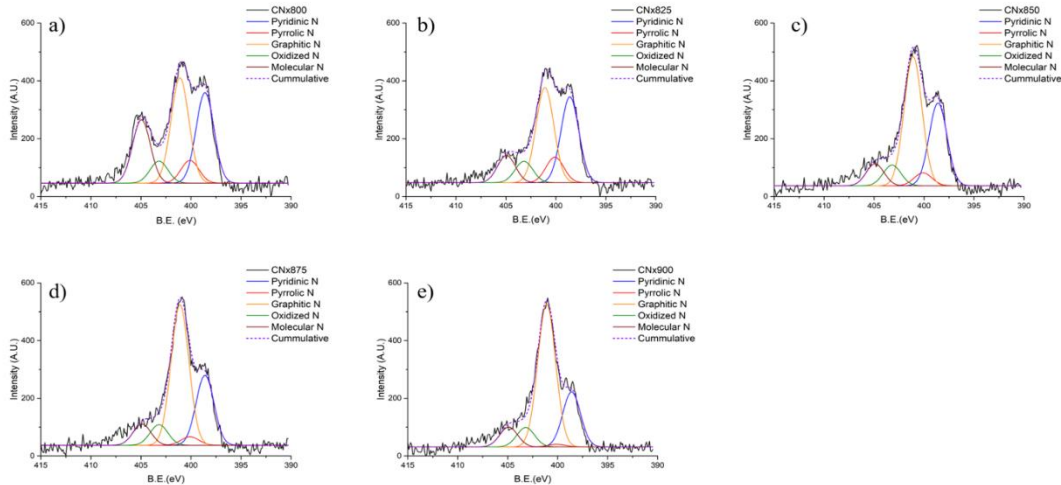
Figure 17. shows the XPS analysis of N 1s where it can be observed the five different species of nitrogen in the carbon nanotubes; pyridinic nitrogen at 398.6 eV, pyrrolic nitrogen at 400.1 eV, graphitic nitrogen at 401.1 eV, oxidized nitrogen at 403.2 eV and molecular nitrogen at

Figures 18a and 18b show the XPS spectra of samples CNx800 and CNx900 respectively (The XPS N1s spectra from the five different CNx samples can be found in figure 17). Five nitrogen species were detected: pyridinic nitrogen (Npy) at 398.6 eV with the sp^2-hybridized nitrogen bonded to two carbon atoms, pyrrolic nitrogen (Npyrr) at 400.1 eV corresponding to nitrogen substitution as pentagonal pyrrolic nitrogen, graphitic nitrogen (Ngraph) at 401.1 eV substituting carbon atoms in the carbon network 403.2 eV and molecular nitrogen (Nmol) at 404.9 eV presumably encapsulated in the cavities of the nanotubes. (Bulusheva et al., 2008; González, Valenzuela-Muñiz, Alonso-Nuñez, Farías, & Gómez, 2017; Guo et al., 2016; Kusunoki, Sakai, Igari, Ishidzuka, & Takami, 2001; Maldonado, Morin, & Stevenson, 2006; Pels, Kapteijn, Moulijn, Zhu, & Thomas, 1995; Raymundo-Piñero et al., 2002)

Figure 18c and 18d present the general trends for the total nitrogen content (relative to carbon) and the different nitrogen species (relative to total nitrogen) as a function of the synthesis temperature for the five different samples. It is observed a slight decrease in the nitrogen content as shown in figure 18c. The

analysis of the nitrogen species in figure 18d reveals that Ngraph exhibits a positive slope while Nmol presents a decrement as the synthesis temperature is increased; Npy and Npyrr show a decrease after 825 °C; while the Nox remains practically constant. To have a closer comparison among the different samples we display the total Nitrogen content values in Table 3, together with the distribution on the different Nitrogen species (relative to carbon). The increasing trend is kept for the Ngraph, while the Npy shows a similar trend as in Figure 18d decreasing after 825 °C. These results correspond to CNx samples obtained by the CVD spray pyrolysis technique, where the nitrogen source comes from the precursor solution solvent (benzylamine). The nitrogen incorporation into the nanotubes carbon network occurs directly during the synthesis process, consequently the synthesis temperature plays a critical role, as evidenced in figure 17 results. Nonetheless, it is worth mentioning that nitrogen doping into graphitic materials can be achieved by different strategies, such as thermal annealing under NH_3 atmosphere of graphitic samples like graphene oxide or HOPG to mention some (Guo et al., 2016; Lai et al., 2012); where the incorporation mechanism can be quite different resulting in different nitrogen proportions.
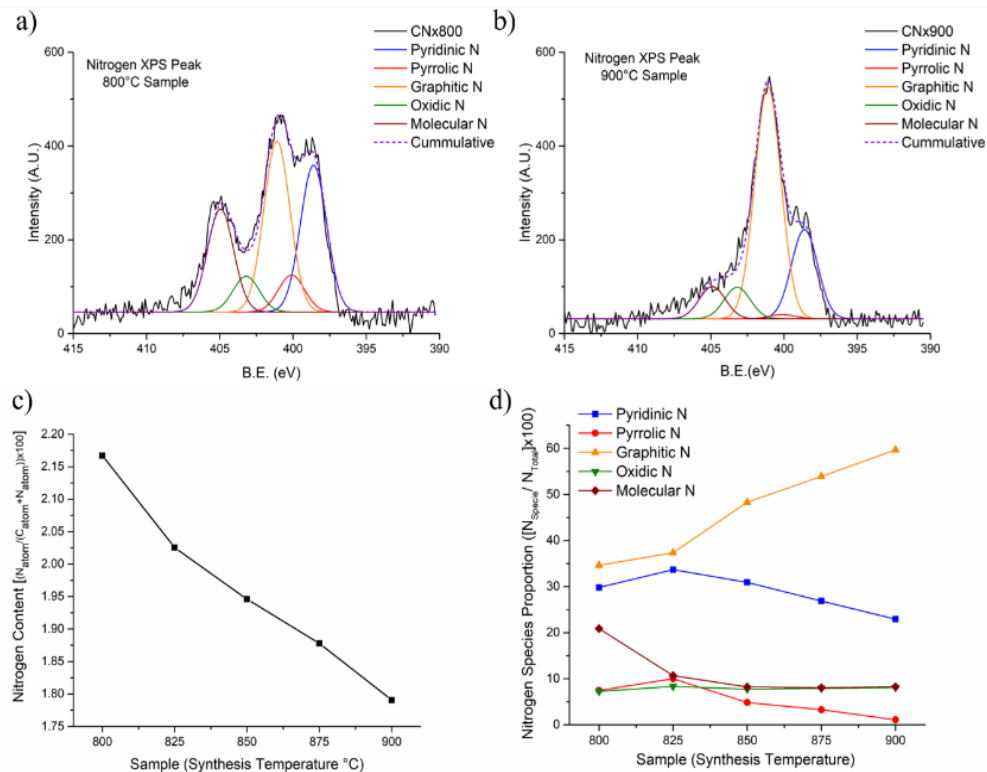
Figure 18. XPS deconvolution of CNx sample synthesized at 800°C, b) XPS deconvolution of CNx sample synthesized at 900°C, c) Nitrogen content at CNx samples synthesized at different temperatures, and d) Nitrogen species proportions in CNx samples synthesized at different temperatures, and d) Nitrogen species proportions in CNx samples synthesized at different temperatures.

It should be highlighted the clear trend observed in figure 18d of increasing the Ngraph in our nitrogen-doped carbon nanotubes when the synthesis temperature is increased, which is also observed in Table 3. This result allows us to systematically analyze the role of graphitic nitrogen in the ORR.

Table 3. Distribution of N species obtained from the deconvoluted N 1s XPS spectra

Sample	N Content	Pyridinic N	Pyrrolic N	Graphitic N	Oxidized N	Molecular N
	(at %)	(at %)	(at %)	(at %)	(at %)	(at %)
		(398.6 eV)	(400.1 eV)	(401.1 eV)	(403.2 eV)	(404.9 eV)
CNx800	2.167	0.646	0.162	0.75	0.157	0.452
CNx825	2.025	0.682	0.203	0.756	0.169	0.216
CNx850	1.946	0.602	0.094	0.94	0.15	0.16
CNx875	1.878	0.505	0.061	1.012	0.149	0.151
CNx900	1.791	0.41	0.019	1.069	0.145	0.148

5.1.3 Oxygen Reduction Reaction Evaluation

Cyclic voltammetry was performed to evaluate the role of nitrogen doping in the carbon nanotubes. This was performed preparing the electrode by depositing 0.2 mg of CNx on the surface of glassy carbon electrodes modifying the conventional usage of Nafion 117. The CV was measured in an alkaline media under saturated oxygen conditions. Figure 19a shows the oxygen reduction activity between 0.1V to 1.1V vs. RHE. When the electrochemical activity of MWCNTs (absence of Nitrogen sites) is compared to the activity of the CNx samples, the onset potential of the MWCNTs is at lower values with a considerably lower peak current. This points to the nitrogen sites as having a strong influence in the ORR activity being registered. Moreover, it can be observed a shift of the onset potential to more positive values for samples synthesized at higher temperatures. Remarkably, the onset potential values trend from the different samples follow a strong correlation with the Ngraph proportion present in the samples, suggesting that an increase in Ngraph improves the electrocatalytic activity of CNx (as shown in figure 19b). According to this evidence, we propose the graphitic Nitrogen (Ngraph) as the active sites for the ORR activity measured.
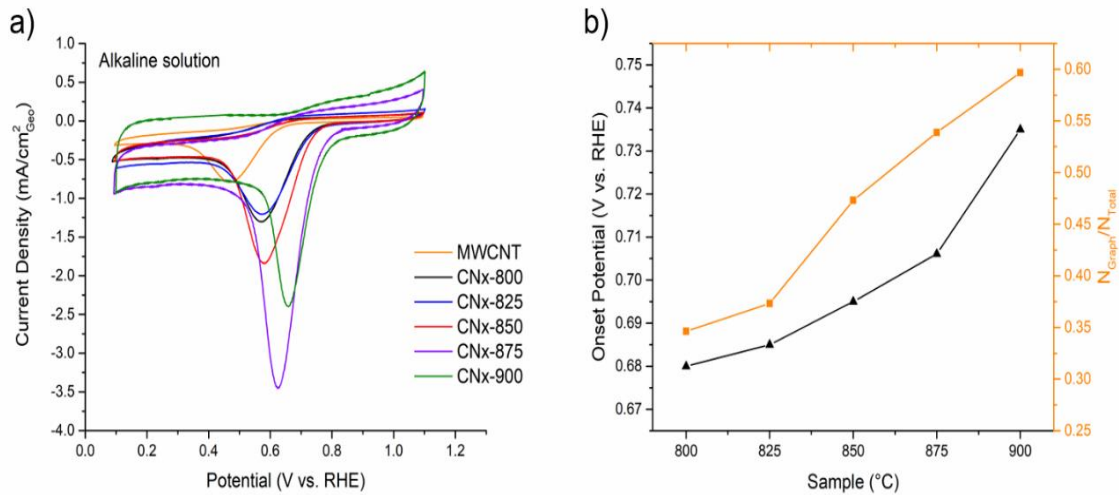
Figure 19. (a) Cyclic voltammograms of CNx synthesized at different temperatures and (b) correlation between the Ngraph present in different samples and the ORR onset potential obtained from the CV of the samples.

In order to estimate the population of Ngraph in the different samples we measured the EASA (Electro-active Surface Area), which was obtained performing CV using 5 mM K3Fe(CN)6 / 0.1 M KCl, at scan rate of 50 mV/s and calculated using the Randles-Sevcik equation (equation 9)

$$i_p = 2.69x10^5 * n^{3/2} * A * D^{1/2} * V^{1/2} * C \tag{9}$$

Where, i_p is the current peak (A), n=1, D=4.34x10^{-6} (cm^2/s), V is the scan rate (V/s), C is the concentration (mol/mL). Solving for A and dividing by the mass loading we obtained the electroactive surface area (cm^2).(Y. Xue et al., 2012)

The CV was performed preparing the electrode by depositing 0.2 mg of CNx on the surface of glassy carbon electrodes with a geometric area of 0.07 cm^2.

Table 4. Electroactive Surface Area of the different samples of nitrogen-doped carbon nanotubes.

Electrode	CNx800	CNx825	CNx850	CNx875	CNx900
EASA (cm²/mg)	6.55	6.59	6.45	6.21	6.19

Linear sweep voltammograms (LSV) were recorded using a rotating disk electrode (RDE) with four different rotation speeds, to analyze the CNx electrocatalytic activity for the ORR and kinetic parameters when the graphitic nitrogen was systematically increased. Then, the CNx samples were drop-casted into the RDE electrode (0.2 mg). The LSVs were performed in alkaline media under saturated oxygen conditions. The density current was normalized against the geometric area. It can be seen from figure 20a two different regimes, at approximately 0.6 V vs. RHE where the ORR is under a diffusion-controlled regime with the mass transfer of oxygen to the electrode determining the ultimate current density; and over 0.6 V vs. RHE where the ORR is under the kinetics-controlled regime and the electrocatalytic activity of the sample is being evaluated. The polarization curves at different rotation speeds represent different oxygen supply rates.

To investigate the kinetic reaction mechanism, the Koutecký-Levich (K-L) model is employed. In the K-L model, the current density measured (j) includes a kinetic (jk) and a diffusion flux (jd) as shown in equation (10)

$$\frac{1}{j} = \frac{1}{j_k} + \frac{1}{j_d} = \frac{1}{j_k} + \frac{1}{B\sqrt{\omega}} \tag{10}$$

In which the B factor is given by:

$$B = -0.62nFD_{O_2}^{2/3}\vartheta^{-1/6}C_{O_2}^* \tag{11}$$

Where n is the number of electrons transferred during the reaction; F is the Faraday constant (96486 C mol^{-1}); DO2 is the oxygen diffusion coefficient (1.73x10^{-5} cm2 s^{-1}); ϑ is the kinematic viscosity (0.01 cm2 s^{-1}); and CO2* is the bulk oxygen concentration (1.3x10^{-6} mol cm^{-3}). The ω corresponds to the rotation speed of the RDE.

Three fixed potentials (E1= 0.6 V vs. RHE; E2= 0.5 V vs. RHE; E3= 0.4V vs. RHE) were selected to obtain K-L plots with linear regressions as presented in figure 20b. The three linear regression showed similar slopes presenting a standard deviation of 10%, with good agreement with the theoretical slope for a two-electron process, indicating a good selectivity for the hydrogen peroxide generation.

Figure 20c shows the LSV for the different samples at 1600 rpm. It is observed a shifting behavior of the onset potential to more positive values related to the increment in Ngraph. This indicates an improvement in the electrocatalytic performance which must be related to the adsorption/reduction processes. Figure 20d shows the K-L analysis performed at 0.5V vs. RHE for the five different samples.
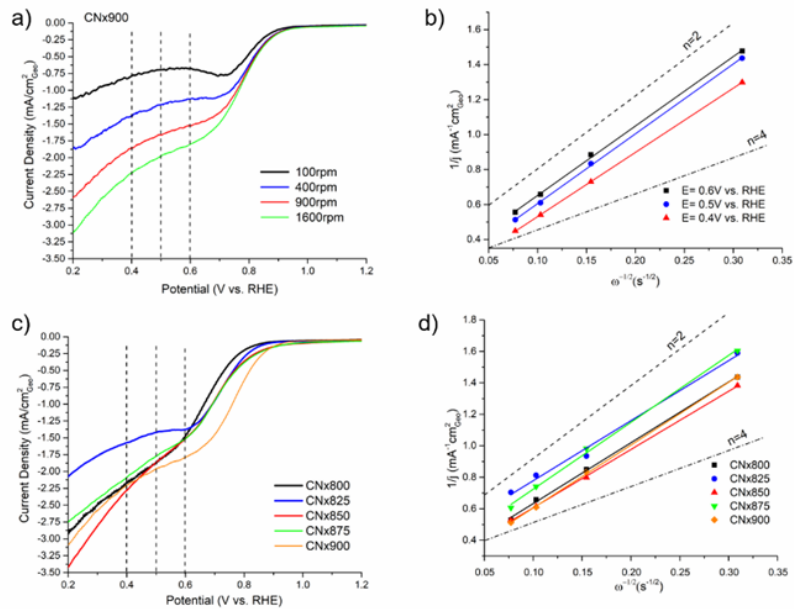
Figure 20. LSV (a) LSV of CNx900 at different rotation speeds, (b) K–L analysis at fixed potentials, (c) LSV of all the samples at 1600 rpm, and (d) K–L analysis of the samples. All the samples were measured at pH 13

It is observed how the linear regression slopes are closer to the theoretical two-electron transferred slope. The values of the complete analysis are shown in table 5. It is observed for the average values how the samples with higher Ngraph content present an increment in the kinetic current density. The general trend for the n values corresponds to values closer to 2, corresponding to the two-electron pathway for the ORR, pointing out the material as a good H_2O_2 generator.

However, it is noteworthy to mention that obtaining of non-integer numbers in between 2 and 4 for n indicate mixed processes due to the presence of varying reactivity for different nitrogen species on the CNx. On this line, it is interesting to point out that the higher values for n were obtained for the CNx825 sample corresponding to the sample with the highest pyridinic nitrogen content (see figure 18).

These results are consistent with the evidence reported by (Lai et al., 2012), where they suggest that the graphitic nitrogen plays an important role to increase the limiting current density while pyridinic nitrogen could promote the ORR reaction mechanism from a two-electron process to a four-electron process. In accordance with the general trend obtained here, where an increase in limiting current density is observed when the Ngraph increases in the CNx; and a slight increase in the average n value is obtained related with a higher proportion of pyridinic nitrogen.

Therefore, the observed shifting in the onset potential correlated with the Ngraph increment in the different samples in figure 19a, closer to 0.7 V vs. RHE (which corresponds to the standard reduction potential for the ORR for H_2O_2 generation) indicates that our CNx samples enriched by Ngraph favor the two-electron pathway. This is also supported by the Koutecký-Levich analysis observing a trend between more Ngraph and a slope closer to the two-electron pathway (as shown in table 5). Confirming that Ngraph must be favoring the two-electron pathway for the H_2O_2 generation.

Table 5. Number of transferred electrons (n) and kinetic current density (jk)at fixed potentials in alkaline media.

	0.6 V vs. RHE		0.5 V vs. RHE		0.4 V vs. RHE		Average	
	n	jk (mAcm^{-2})	n	jk (mAcm^{-2})	n	jk (mAcm^{-2})	n	jk (mAcm^{-2})
CNx800	2.91	2.16	2.18	2.84	2.16	5	2.41	3.33
CNx825	3.01	2.97	2.18	2.62	2.38	4.5	2.52	3.36
CNx850	2.11	2.77	2.23	4.31	2.77	5.26	2.37	4.11
CNx875	2.08	2.7	1.95	3.45	1.86	6.7	1.96	4.28
CNx900	2.09	4	2.08	5	2.26	6.25	2.14	5.08

An important task for wastewater remediation is to optimize the materials for ORR via the two-electron pathway, which can contribute to the in-situ H_2O_2 generation. Then it is quite essential to test these materials under neutral media (pH=7) using the LSV RDE analysis.

Starting with the CNx900 for RDE analysis, we selected three fixed potentials (E1= 0.01 V vs. RHE; E2= -0.09 V vs. RHE; E3= -0.19 V vs. RHE) as shown in figure 21a, and the K-L plots are presented in figure 22b. The lines slopes behavior is closer to the two-electron pathway while incrementing the applied potential.
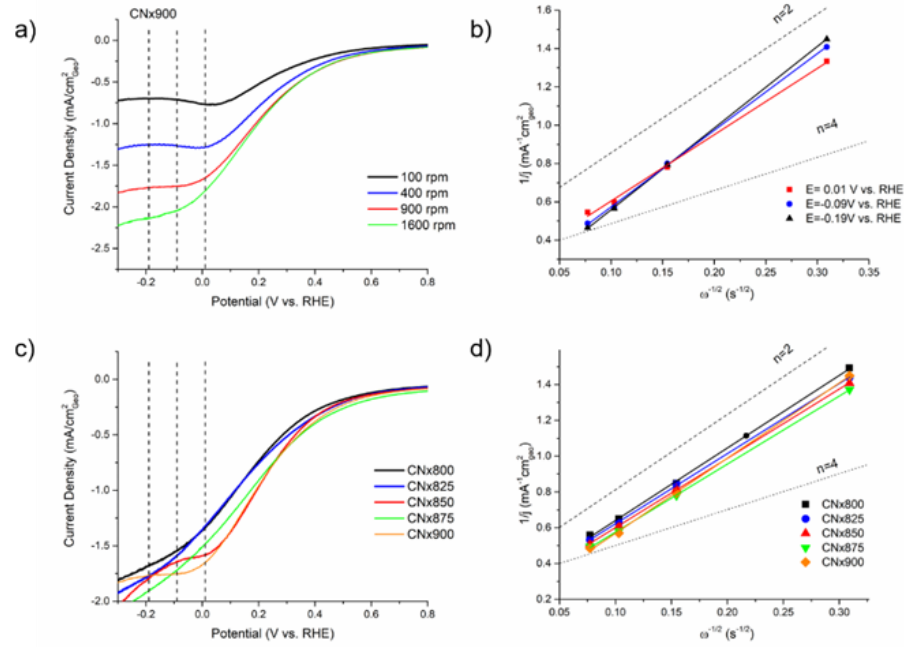
Figure 21. (a) LSV of CNx900 at different rotation speeds, (b) K–L analysis at fixed potentials, (c) LSV of all the samples at 1600 rpm, and (d) K–L analysis of the samples. All the samples were measured at pH 7.

The same analysis was performed for all the samples as shown in figure 21c. The number of transferred electrons (n) and the kinetic current density (jk) values are reported in table 6. The general trend for the n values corresponds to the ORR via the two-electron pathway. It is interesting to outstand how the jk increases when the Ngraph increases in both alkaline and neutral media, which can be related to an increase of catalytic sites that permits adsorption of molecular oxygen and enable the oxygen reduction reaction by the two-electron pathway.

Table 6. Number of transferred electrons (n) and kinetic current density (jk)at fixed potentials in a neutral medium.

	0.01 V vs. RHE		-0.09 V vs. RHE		-0.19 V vs. RHE		Average	
	n	jk (mAcm^{-2})	n	jk (mAcm^{-2})	n	jk (mAcm^{-2})	n	jk (mAcm^{-2})
CNx800	2.1	3.33	1.96	4.34	2.18	4.12	2.08	3.93
CNx825	2.28	3.33	2.11	4.08	2.05	6.66	2.14	4.69
CNx850	2.5	3.46	2.14	4.86	2.36	5.26	2.33	4.53
CNx875	2.24	3.33	2.17	5.26	2.18	7.14	2.19	5.24
CNx900	2.56	3.57	1.97	6.66	1.96	7.14	2.16	5.79

5.1.4 Theoretical considerations

In order to explore if the oxygen reduction reaction by the two-electron pathway is energetically favorable with the presence of graphitic nitrogen, we have carried out total energy calculations together with structural relaxations for different models (on graphitic N doped and pristine carbon nanotubes) including O_2 in physisorbed and chemisorbed states near and far away from graphitic N atoms. Also, hydrogen adsorption on both sides of the O_2 molecule to form H_2O_2 was considered. In agreement with the literature (Giannozzi, Car, & Scoles, 2003; Sorescu, Jordan, & Avouris, 2001; Srivastava & Laasonen, 2016; Srivastava, Susi, Borghei, & Kari, 2014), our O_2 physisorbed states are more stable in both cases, see figure 22a and 22b. For adsorption on the pristine nanotube, configurations with almost degenerate energies were found (Sorescu et al., 2001; Srivastava et al., 2014)(in the figure, we show the most stable one). Note that for adsorption on the graphitic N doped carbon nanotube, oxygen molecules preferably adsorb on top of an alpha carbon (first nearest neighbor of N) and it is slightly tilted towards the N position (Figure 22b). O_2 on the N doped carbon nanotubes has an adsorption energy of around 0.1 eV lower than on the pristine nanotube.

The adsorption energy is more favorable due to the electronegativity of N, which leaves the first nearest neighbor carbon atoms uncompensated with a partially positive charge, and then they can receive charge from the O atom of the adsorbed molecule. Such effect points to the key role that graphitic N doping could be playing in ORR reactions. Once knowing that O_2 preferable adsorbs on the graphitic N doped carbon nanotube, we proceed to evaluate the H_2O_2 molecule on the same system. Therefore, several models were optimized by fully relaxing the atomic positions, with configurations near and far away from the N site. We have found that the H_2O_2 molecule preferably adsorbs on the carbon atoms close to the N atoms (see Figure 22c). The peroxide formation is more stable than single oxygen molecules adsorption by 1.45 eV and 1.55 eV for nitrogen doped and pristine carbon nanotubes, respectively. Then in experimental conditions, the formation of H_2O_2 when oxygen is adsorbed on the N doped nanotubes is expected. If we calculate the adsorption energy using the energy of an isolated H atom, this energy is even more stable (-6.20 eV). This is important due to the existence of protons during the experimental conditions.
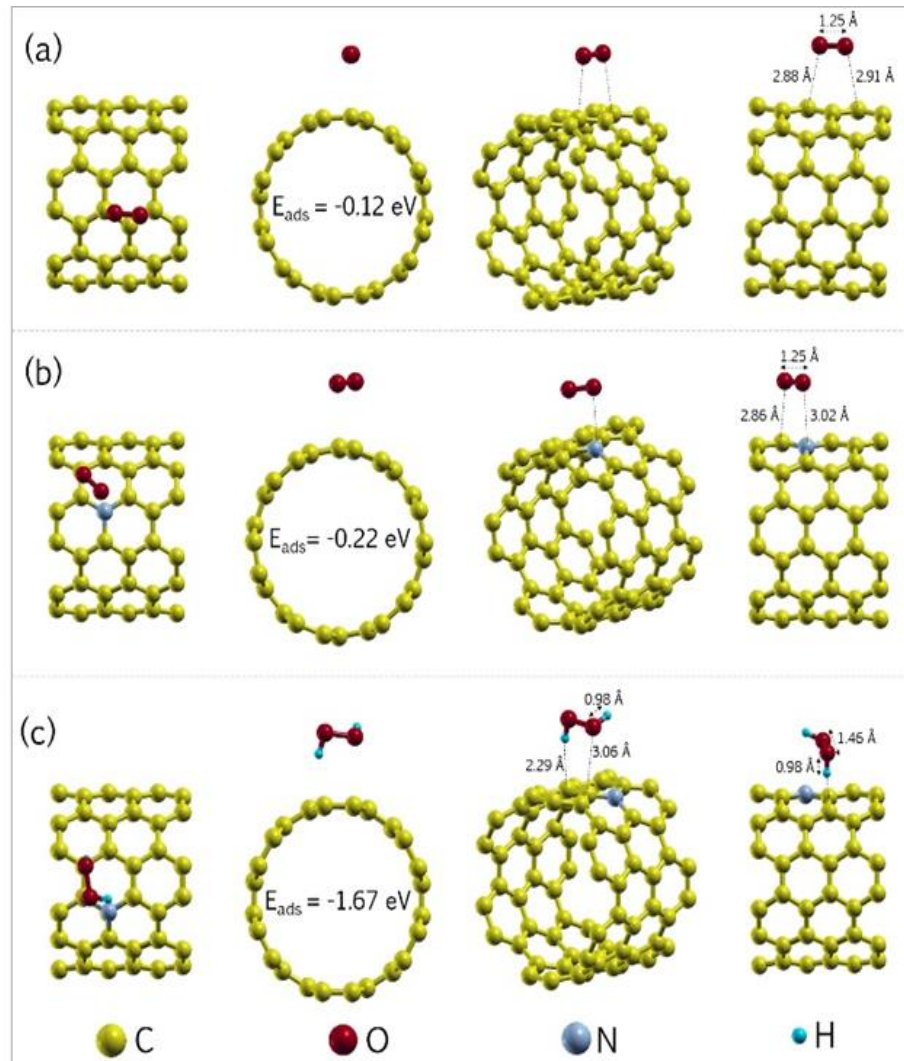
Figure 22. Total energy calculations to explore if the ORR by the two-electron pathway is energetically favorable in the presence of graphitic nitrogen. (a) O2 molecule on a pristine carbon nanotube, (b) O2 molecule on a graphitic nitrogen-doped carbon nanotube and (c) H_2O_2 molecule energetics on graphitic nitrogen- doped carbon nanotube.

5.1.5 Buckypapers as 3D electrodes

Finally, the carbon nanotubes (CNTs) synthesized by CVD grow inherently in a forest-like arrangement. This type of arrangement is usually obviated when electrocatalytic applications are being investigated which can decrease the active surface area available, a crucial role for the ORR performance. To enlighten this concept, we explored between two different arrangements of nitrogen-doped carbon nanotubes (ink or buckypaper) by measuring two different samples where the mass amount was similar: i) ~1.4mg of CNx soot directly from the synthesis slightly dispersed in a water-based ink deposited on the glassy carbon

electrode (1.4mg ink); and ii) a ~0.25cm^2 geometric area CNx membrane piece of ~1.3mg (BP-CNx A1). In order to explore how the buckypaper configuration could scale up, we include a third sample: iii) a ~1.0cm^2 geometric area CNx membrane piece of ~4.3mg (BP-CNx A2). See section 4.2 for further details. Figure 23a shows the cyclic voltammetry of the three different samples of nitrogen-doped carbon nanotubes synthesized at 900°C (CNx900) with the two different configurations described above. By monitoring the cathodic peak current (Ipc) obtained in the CV, together with the geometric area, as presented in figure 23b, we can observe the Ipc of CNx900 (1.4mg ink) at 0.74mA which is lower compared to the buckypaper A1 which is 0.85mA, regardless that CNx900 (1.4mg ink) has more significant geometric area. This could be related to the dispersion of carbon nanotubes assembling the CNx into a more efficient arrangement enhancing the active surface area. However, due to the steady-state assumption of the technique higher currents could not be achieved in cyclic voltammetry. Moreover, it can be observed how the buckypaper configuration keeps with the trend of higher currents compared to the geometric area when the buckypaper size is increased from A1 to A2. Figure 23c shows an SEM micrograph of the CNx900 soot after the synthesis, where it can be observed an agglomerate of the forests –like arrays typical from CVD synthesis; nonetheless, after hydrothermic treatment for the buckypapers fabrication, we can observe how the forest-like arrays disappear, and a uniform membrane has been assembled as shown in figure 23d. The inset in figure 23d (figure 23e) corresponds to a macroscopic picture of a buckypaper, where it can be observed its actual size. It is remarkable that the buckypaper configuration permits to handle the materials in a more natural way than the ink configuration, allowing to think in applications where macroscopic membranes are needed as 3D electrodes.

The macroscopic size of the buckypaper electrodes allows to scale up the electrocatalytic material accessing to considerable increments of Ipc values which translates into higher yields of the ORR reaction. Moreover, the microscopic structure of the buckypaper arrangement meets the need of a conductive network and a porous framework to facilitate electron transfer and mass-gas diffusion at the interface between electrolyte, active sites and gas phase. With the need for the design and development of viable electrocatalysts for the ORR and the high demand for H_2O_2 on-site production, this should represent an important contribution for electrocatalytic applications of the ORR.
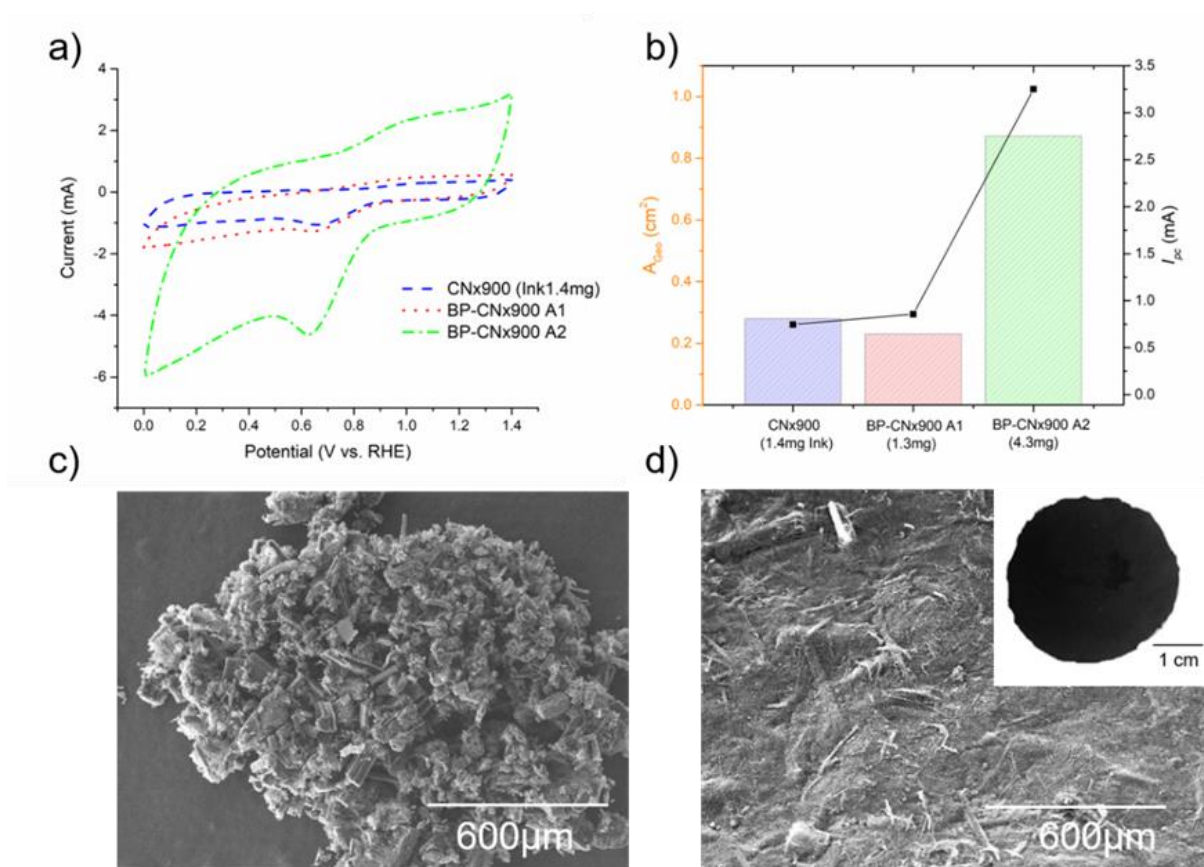
Figure 23. .(a) Cyclic voltammograms for the different configurations of CNx, (b) cathodic peak current (Ipc) for the different configurations and their geometric areas, (c) an SEM image of the CNx-soot at 50×, (d) an SEM image of buckypaper at 50×, and (e) a macroscopic image of the buckypaper

5.1.6 Proposed mechanism

Then, we propose a mechanism that relate the two-electron pathway ORR and the role of graphitic N in the ORR (schematically described in detail in figure 24). This mechanism outstands, that contrary to the pyridinic nitrogen, the graphitic N is unable to complete the four-electron reduction reaction to end up with a couple of water molecules due to the unbalance of charges, making the graphitic N site to release the anchored molecule (hydroperoxide) which will end up as a H_2O_2 molecule, therefore completing the two-electron pathway favoring the H2O2 generation. When samples are enriched with pyridinic nitrogen, the oxygen reduction reaction could continue from the 2-electron pathway to the 2+2 electron pathway, since none unbalance of charges will push for the anchored molecule release.

The figure 24 presents the proposed mechanism for the two-electron pathway ORR by the graphitic nitrogen, it is worthy to note that all the carbons in the schemes are bonded to three carbon neighbors, and all the carbons are sp2 hybridized. The proposed mechanism can only occur under the polarization conditions.

The graphitic nitrogen has a pair of electrons in its p_z orbital, the electron pair makes a π bonding to an alpha carbon (carbon corresponding to the first neighbor), which turns the graphitic nitrogen to be positively charged and the beta carbon (carbon corresponding to the second nearest neighbor) is negatively charged (steps 1-3 observed in figure 23)

An oxygen molecule can be bonded to the radical alpha carbon by free radical addition between the lone electron in the p_z and the lone electron in the π* of the oxygen molecule; it is important to mention that the bond between the oxygen and alpha carbon has been previously demonstrated by Guo et al., (2016) while Sidik et al., (2006) showed that radical alpha carbon can play a role in the ORR. The free radical addition it is observed in figure 23 steps 4-5.

In order to start the ORR, one electron is supplied by the electrical polarization and one proton from the media, the hydrogen then can be bonded to the oxygen molecule by free radical addition, forming an hydroperoxide group bonded to the alpha carbon (as observed in figure 23 step 6).

However, the formed structure is quite unstable due to the unbalance of charges, then the negative charged beta carbon will tend to make a double bond with the alpha carbon releasing a negative charged hydroperoxide molecule (figure 23 steps 7-8). The mechanism ends when a proton bonds a negative charged hydroperoxide and a second lone electron (supplied by the electrical polarization) recombines to the lone electron in the p_z orbital of the graphitic nitrogen (figure 23 step 9).

This mechanism outstands, that contrary to the pyridinic nitrogen, the graphitic N is unable to complete the four-electron reduction reaction to end up with a couple of water molecules due to the unbalance of charges (due to the negative charged beta carbon and positive charged graphitic nitrogen), making the graphitic N site to release the anchored molecule (hydroperoxide) which will end up as a H_2O_2 molecule, therefore completing the two-electron pathway favoring the H_2O_2 generation. When samples are enriched with pyridinic nitrogen, the oxygen reduction reaction could continue from the 2-electron pathway to the 2+2 electron pathway, since none unbalance for charges will push for the anchored molecule release.
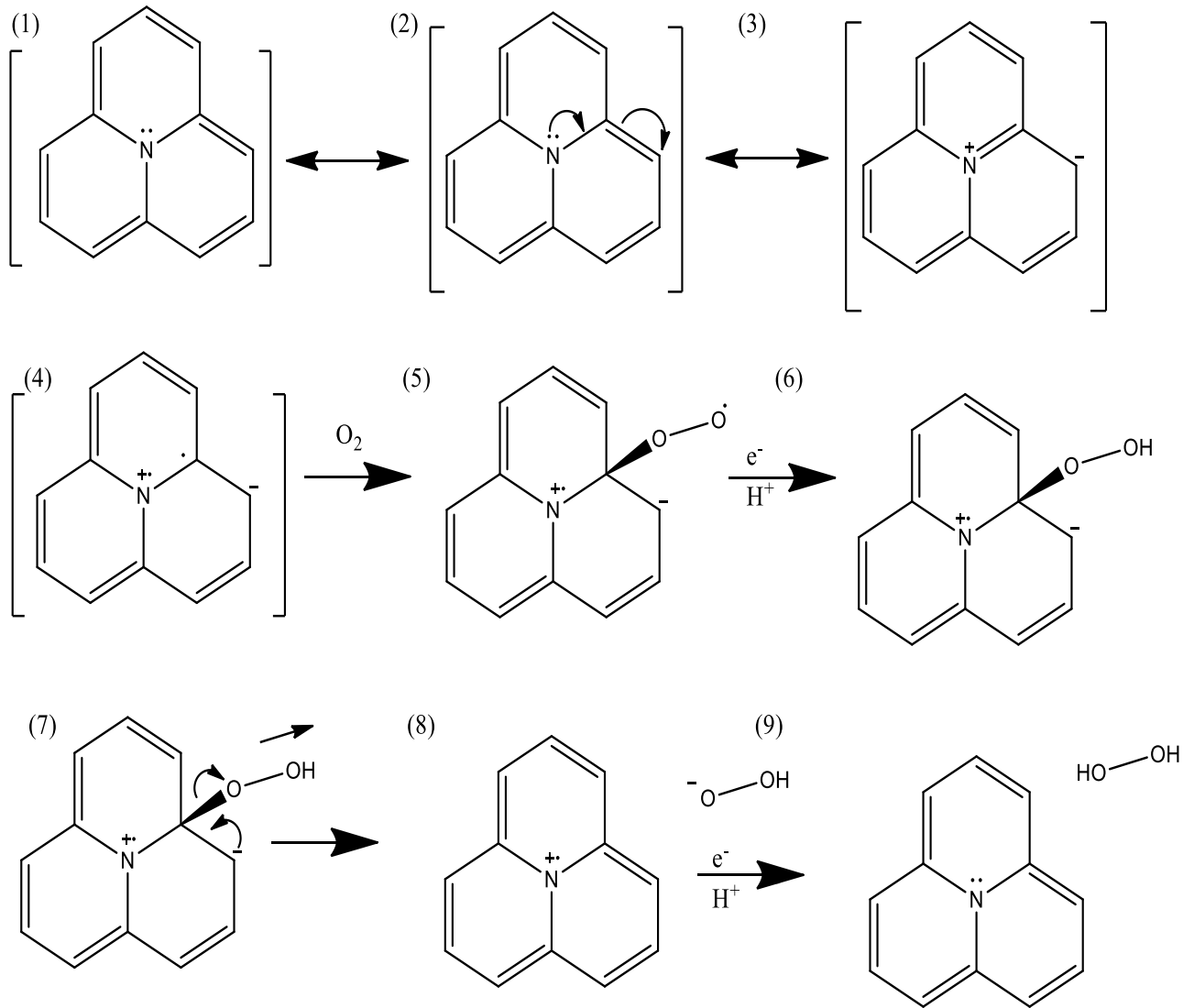
Figure 24. Proposed mechanism for the two-electron pathway ORR performed by graphitic nitrogen.

Section Conclusions

The synthesis temperature resulted in an essential variable to systematically tune the graphitic nitrogen (N_{graph}) in CNx prepared by spray pyrolysis. This effect allowed us to obtain a set of samples where the role of N_{graph} in nitrogen-doped carbon nanotubes can be systematically analyzed for the ORR.

After an XPS analysis, it was observed that the CNx samples analyzed (with a higher content of N_{graph}) favor the two-electron pathway of the oxygen reduction reaction not only in basic media (pH=13) but in a simulated reclaimed water (pH=7). This is an attractive alternative for wastewater remediation application

through the on-site generation of H_2O_2. Moreover, it was proved how N_{graph} is a significant catalytic site for ORR shifting the onset potential to lower potentials; meaning that the more N_{graph}, the less energy needed for the two-electron pathway ORR. Increasing the amount of N_{graph} also enhances the J_k, making N_{graph} desirable for dynamical applications where the two-electron pathway is required. Moreover, a mechanism describing how the graphitic Nitrogen could be favoring the ORR two-electron pathway is presented. Total energy calculations showed that H_2O_2 formation must be favorable with the presence of a graphitic nitrogen site. This statement was corroborated by ab-initio calculations.

It should be remarked how the buckypaper configuration outperformed the electrochemical properties of conventional inks dispersions, showing an outstanding alternative to scale up the properties of CNx for electrocatalytic applications where macroscopic membranes are needed as 3D electrodes. Therefore, the buckypapers correspond to an essential way to create a 3D electrode enhancing the electroactive surface area, being a robust membrane, meeting the need of a conductive network and a porous framework to facilitate electron transfer and mass-gas diffusion at the interface between electrolyte, active sites and gas phase. This points out the buckypaper as an important material to scale up for applications related to reduction reactions.

5.2 Advanced Oxidation Process of dispersed and stabilized Iron Oxide Nanoparticles

5.2.1 State of the Art

5.2.1.1 Advanced Oxidation Process using Iron Oxide Nanoparticles

One of the emergent remediation technologies for the remediation of wastewater contaminated with recalcitrant organic pollutants are the advanced oxidation processes (AOP). The AOPs usually are a combination of oxidants and catalysts which generate highly reactive radicals having strong ability to degrade organic pollutants. For the generation of free radicals one of the most interesting catalysts are the iron oxide materials which present a combination of mixed-valent iron (Fe^{2+}/Fe^{3+}), the iron oxide can promote the two of the most oxidant reaction when are combined with hydrogen peroxide(Fenton-based oxidation) and persulfate (Fenton-like oxidation).(Usman et al., 2018)

The Fenton-based oxidation is a complex catalytic reaction involving the Fe(II) and the hydrogen peroxide under acidic conditions in order to generates the highly reactive hydroxyl radicals (OH) by the Haber-Weiss radical mechanism described by the equation 12. (Haber & Weiss, 1932)

$$Fe(II) + H_2O_2 \rightarrow Fe(III) + HO^- + HO \cdot \tag{12}$$
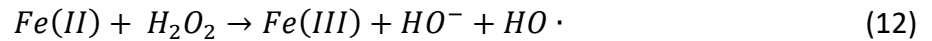
These Fenton-like oxidation is a similar oxidation reaction involving the use of the persulfate anion and the Fe(II) specie which generates a strong oxidant, the sulfate free radical (sulfate) by the equation 13.

$$Fe(II) + S_2O_8^{2-} \rightarrow Fe(III) + SO_4^{2-} + SO_4^{\cdot-} \tag{13}$$
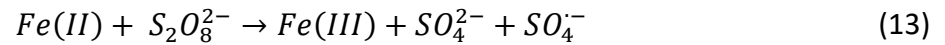
These two free radicals are the most powerful oxidizing agents presenting E^0= 2.8 V for the ·OH and E^0= 2.6 V for the $SO_4^{\cdot-}$ (Gligorovski et al., 2015; Tsitonaki et al., 2010)

Xue, Hanna, & Deng in 2009 studied the iron stoichiometry of the magnetite synthesizing nano magnetite and micro magnetite (labeled as M1 and M2) which presented an Fe(II)/Fe(III) ratio of 0.24 and 0.43 respectively, which allowed them to study this ratio in the kinetics of the Fenton reaction using magnetite (as presented in figure 25). It is observed that the M2 sample presented higher degradation rate of their target molecule compared to the M1. This result prove that the Fe(II) in the magnetite plays an important role for the Fenton reaction, moreover that heterogeneous Fenton using magnetite is possible.
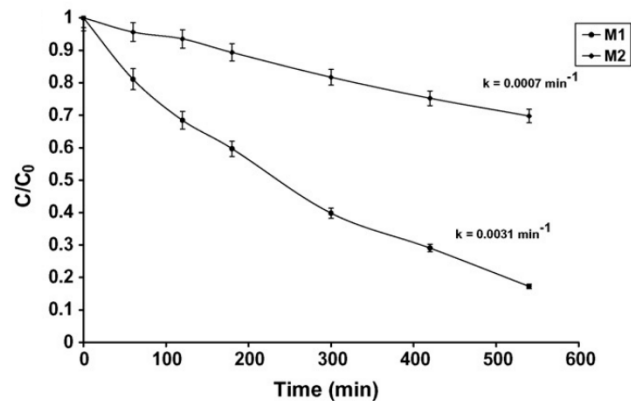
Figure 25. Degradation curves showing the importance of Fe(II)/Fe(III) ratio (image taken from X. Xue et al., in 2009).

However, exists also another Fenton-like reaction for the magnetite which are enhanced under light irradiation called photo-Fenton (if hydrogen peroxide is used) or photo-Fenton-like (if persulfate is used). The reaction for this photo-stimulated Fenton reactions are presented in equation 14. (Minella et al., 2014)

$$Fe^{III}OH^{2+} + hv \rightarrow Fe^{II} + HO \cdot \tag{14}$$

The photo-Fenton reaction requires Fe(III) chelated by an OH which contrasts to the Fenton-based reaction which requires Fe(II). It is important to remark that the enhancement is due to the synergy between the Fenton-based and photo-Fenton.

To prove that, Avetta et al. in 2015 analyzed the magnetite nanoparticles for a photo-Fenton-like using persulfate, observing (see figure 26) when the magnetite nanoparticles were in contact with the persulfate and UVA irradiation presented the maximum degradation rate. When the phenol (the target molecule) was irradiated with UVA without magnetite nanoparticles the degradation took place via photolysis of the persulfate.
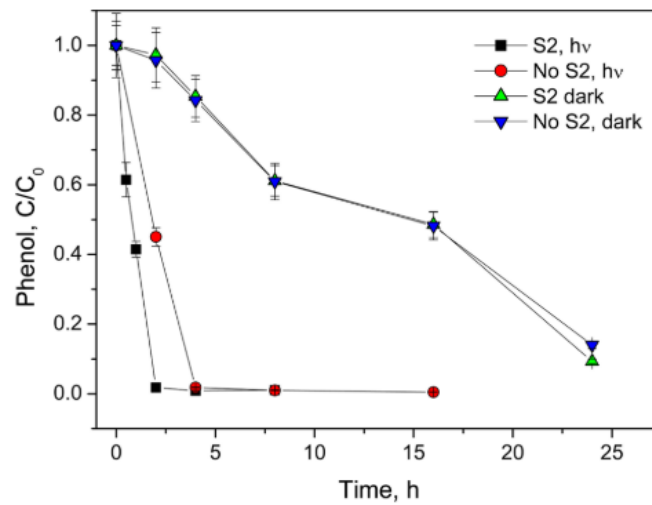
Figure 26. Photo-Fenton-Like reaction using Magnetite Nanoparticles (image taken from Avetta et al. in 2015).

The obtained results demonstrated the importance of the synergy between the iron oxide and the enhancement of the degradation rate assisting the magnetite nanoparticles with UVA light.

5.2.1.2 Water quality in the Tijuana City

The quality of the treated water has been monitored by the Cuenca Rio Tijuana (CRT). The last update of the analysis of the water quality was reported by Melgar-Lopez, Mayra; Cambreros-Urbina in 2017. Three parameters were selected by the CRT in order to observe the pollution in the reclaimed wastewater: The Biochemichal Oxygen Demand (BOD5), Chemical Oxygen Demand (COD), and the Total Suspend Solids (TSS).

The NOM-001-SEMARNAT-1996 (virtual page shorturl.at/jqvzX revised September 20th 2019) mention that the permissible limit parameters for the reclaimed wastewater are: i) COD 150 mg/L, ii) TOC (total organic carbon) 38 mg/L, and iii) TSS 60 mg/L. It is observed in figure 27 that the measurements made by CRT shown the reclaimed wastewater exceeded the permissible limits in COD ant TSS. The values obtained by the COD (200 mg/L) said that the water is considered contaminated (40 < COD ≤ 200) reaching the highly contaminated (COD > 200), while the TSS (73 mg/L) is considered of good quality (25 < TSS < 75). (Melgar-Lopez & Cambreros-Urbina, 2017)
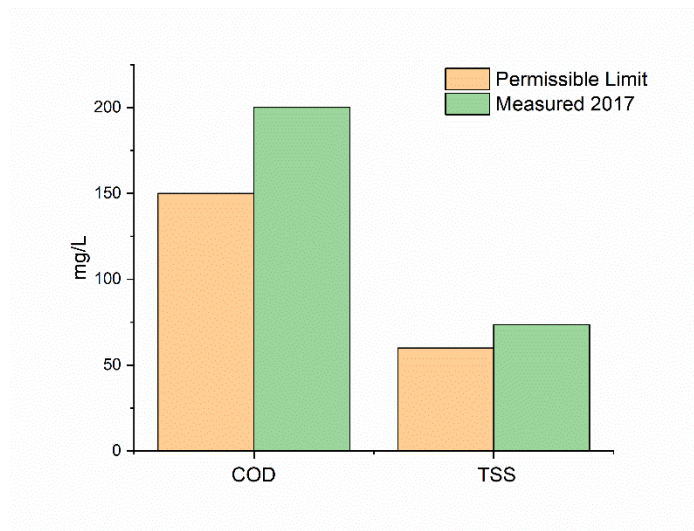
Figure 27. Measured reclaimed wastewater in 2017 by CRT (image made with the data presented by Melgar-Lopez & Cambreros-Urbina, in 2017).

5.2.2 Dispersion and stabilization using ultrasound

The dispersion and stabilization were performed using two different iron oxide nanoparticles: i) α-Fe$_2$O$_3$ and ii) Fe$_3$O$_4$ (purchased at US Nano). For the dispersion of nanoparticles, it was assisted by an ultrasonic probe for n cycles (1 cycle = 30 min of sonication using pulses of 4 seconds on and 1 second rest), adding the iron oxide nanoparticle to 80 mL of a 100 mM solution of stabilizing agent (see figure 28).

We started with a dispersion of iron oxide nanoparticles using the α-Fe$_2$O$_3$ and CTAC by the following conditions: i) it was dispersed 1 wt.% of α-Fe$_2$O$_3$ during 1 cycle ii) the dispersion was cooled down and concentration reduced to 0.1 wt.% sonicated for another cycle iii) the dispersion was reduced to 0.01 wt.% and sonicated for one last cycle.

After the dispersion of α-Fe$_2$O$_3$ at different cycles and different concentrations, it was observed that the 0.01 wt.% presented the higher stability. Then, we proceeded with different stabilizing agents following the same procedure: starting with 1 wt.% dispersion of α-Fe$_2$O$_3$ in each stabilizing agent, followed by one probe sonication cycle; then a dilution to 0.1 wt.% was made following a second probe sonication cycle, to end up with a third dilution to 0.01 wt.% followed by one more probe sonication cycle.
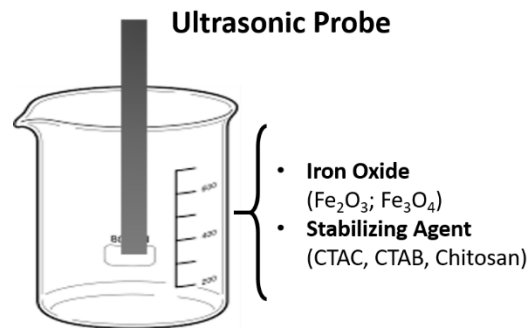
Figure 28. The dispersion and stabilization scheme.

Four stabilizing agents were used, in order to find the right surfactant, we tested solutions of 100 mM cetyltrimethylammonium bromide (CTAB), 100 mM cetyltrimethylammonium chloride (CTAC), 100 mM Sodium citrate (SC), and 0.01 mM of Chitosan.

It is important to remark that chitosan is not properly a surfactant, however, when it is under acidic conditions the amino groups (R-NH$_2$) accept a proton from the media and therefore it presents a charged amino group (R-NH$_3^+$), to do that in the chitosan/deionized water solution (0.01 mM) it was added 100 mM of acetic acid to reach a pH 3 under vigorous stirring at 60 °C.

Besides the four stabilizing agents explored, we included three control conditions: i) probe sonication without stabilizing additive (labeled as no. 3 vial); ii) bath sonication without stabilizing additive (labeled as no. 4 vial); and iii) none sonication without stabilizing agent additive (labeled as no. 5 vial). Moreover, two more samples were explored using 100 mM KCl (labeled as no. 6 vial) and 100 mM KBr (labeled as no. 7 vial), to analyze the adsorption of the halides on the iron oxide nanoparticles. See table 7 for the complete labeling of the nine samples analyzed.

Table 7. Conditions of the Stabilization tests.

Label	1	2	3	4	5	6	7	8	9
Surfactant	CTAC	CTAB	-	-	-	KCl	KBr	SC	Chitosan
Sonication	Probe	Probe	Probe	Bath	-	Probe	Probe	Probe	Probe

Figure 29 shows the stabilization results, it is remarkably to observe the 4th and 5th vials which were the samples without the ultrasonic probe assistance at t = 0 h were completely decanted, the 3rd vial showed to be stable until 3 hours where the iron oxide was precipitated, it could be explained due to the absence of stabilizing agents but showed higher dispersion. It allowed us to conclude that the ultrasonic probe is fundamental for the iron oxide dispersion and stabilization.

After three hours only two samples remained stabilized: using CTAC (labeled as 1) and the sample stabilized using chitosan (labeled as 9). All the samples were tracked until 72 h showing the best results were for CTAC and Chitosan.
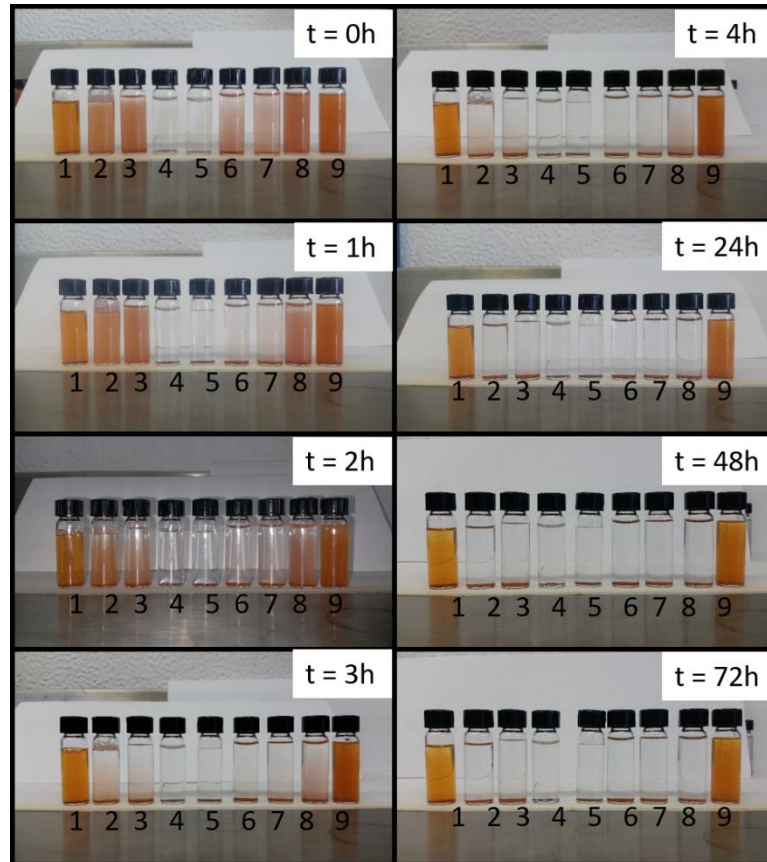
Figure 29. Stabilization test of several stabilizing agents through time.

Later, it was measured the dispersed α-Fe$_2$O$_3$ nanoparticles using CTAB, CTAC and Chitosan using zeta potential (figure 30). However, in order to observe if the halogens contained in the CTAB and CTAC (chlorine and bromine) could poison them we disperse α-Fe$_2$O$_3$ nanoparticles in 100 mM of KCl and 100 mM of KBr. Figure 30 shows the zeta potential of the dispersed nanoparticles observing that the dispersion using the three surfactants presented positive surface charges as expected, however, the α-Fe$_2$O$_3$ nanoparticles dispersed with KCl and KBr showed negative charges that could be attributed to the halogens adsorbed on the nanoparticle surface. Observing these results, we conclude that CTAC and Chitosan were the best candidates for the stabilization of 0.01 wt. % α-Fe$_2$O$_3$.
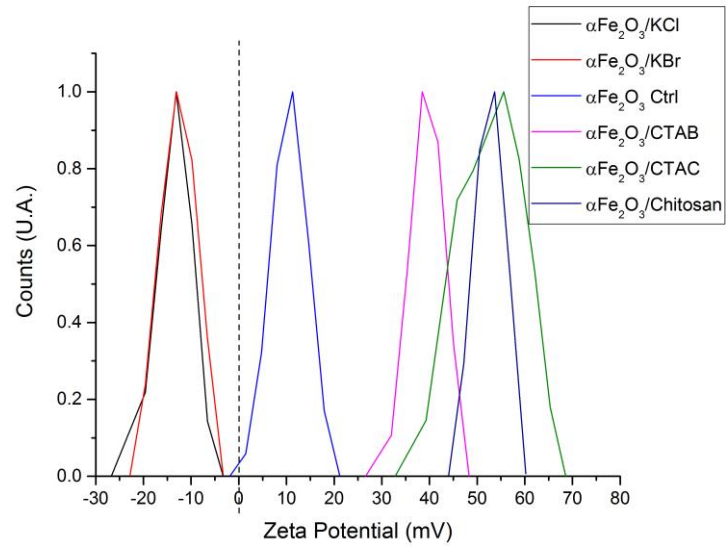
Figure 30. Zeta potential of the dispersed and stabilized alpha iron oxide (0.01 wt. %)

Then, we proceeded to test these stabilizing conditions with magnetite nanoparticles varying the number of applied probe sonication cycles from 1 to 8 cycles. The dispersion was performed using raw magnetite, magnetite with CTAC (labeled as magnetite@CTAC), and magnetite with chitosan (labeled as magnetite@chitosan) at 0.01 wt.% of concentration.

Figure 31 shows the DLS analysis where it can be observed that for all the three samples the bulk magnetite (up to 3000 nm of hydrodynamic diameter) was dispersed into smaller clusters, however, it was not observed smaller clusters than 100 nm of hydrodynamic diameter, A clear tendency of reducing the size of the clusters related with the applied cycles is observed when using both stabilizing agents.
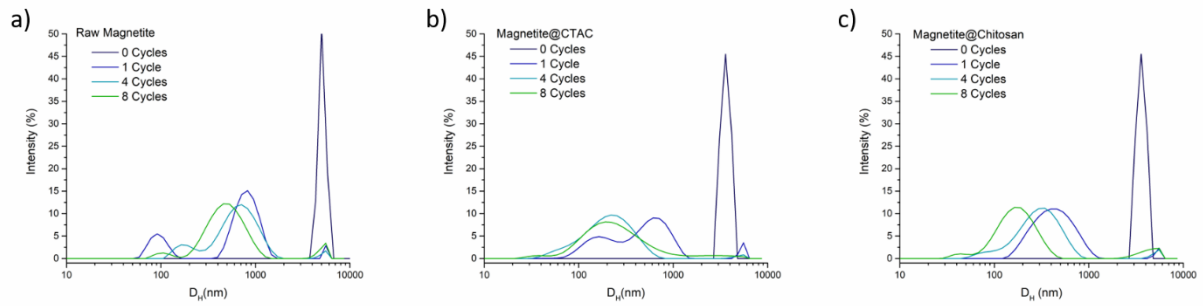
Figure 31. DLS analysis of a) Raw Magnetite, b) Magnetite@CTAC, and c) Magnetite@Chitosan.

The samples were analyzed by zeta potential (figure 32), it is observed that both magnetite@CTAC and magnetite@chitosan presented positive potentials, however the magnetite@chitosan showed a clear tendency between the applied cycles and the increment of zeta potential. It is also interesting to note the zeta potential observed for the raw magnetite, obtaining negative potentials with their maximums at -26 mV and -37 mV. This charge could be attributed to the sonochemical reactions between the magnetite surface and the water, therefore carboxyling the magnetite surface (M-OH/M-COOH) explaining the negative charge and why the dispersion presented good stability compared to the magnetite samples without dispersion by ultrasonic probe.
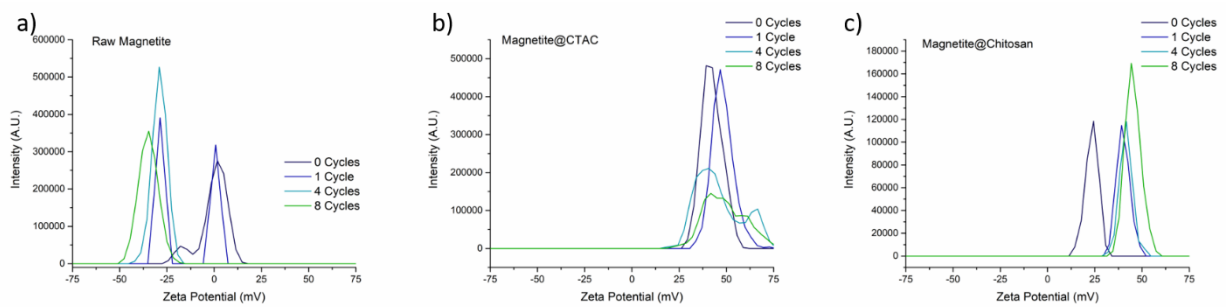
Figure 32. Zeta potential analysis of a) Raw Magnetite, b) Magnetite@CTAC, and c) Magnetite@Chitosan.

5.2.3 Degradation of a target molecule using Fenton reaction

As previously described in section 5.2.2, only magnetite dispersed with CTAC or Chitosan were chosen for degradation tests. Therefore, we dispersed magnetite without surfactants, magnetite with CTAC, and magnetite with Chitosan for 0 to 8 cycles. The conditions used for degradation test were: i) 0.01 wt.% of dispersed magnetite, ii) 50 µM of amaranth red (target molecule) which has an adsorption peak in 520 nm, iii) 60 mM of hydrogen peroxide, and iv) acetic acid to reach a pH of 3. For washing the nanoparticles once dispersed they were precipitated (using a neodymium magnet grade N52) and washed with deionized water until reaching a surfactant concentration of 2 mM in the case of CTAC and 0.2 µM mM in case of Chitosan. It is important to remark that all the tests were performed under dark conditions in order to avoid false positives.

The degradation tests were tracked measuring the reduction in the absorbance peak for 60 min, 90 min, 120 min, and 150 min using the UV-Vis spectrometer (Cary 60). Figure 33 presents the degradation curves of the magnetite. Figure 33a shows the degradation test of the raw magnetite, it is observed that the raw magnetite without dispersion presented the lowest activity reaching a degradation maximum of 81% at 150 minutes, while the raw magnetite dispersed by 1 cycle showed the highest activity reaching a degradation maximum of 93% at 150 minutes, followed by the 4 cycles (85% of degradation at 150 min) and the 8 cycles (83% of degradation at 150 min). This activity could be explained due to the ultrasound effects in the magnetite clusters, it could not only disaggregate the bigger clusters to smaller clusters but having a sonochemical effect that could be poisoning the magnetite (see section 5.2.2 and discussion regarding figure 32a therein).

Figure 33b presents the activity of dispersed magnetite with CTAC observing a considerable reduction in activity, it could be attributed to the chlorine ion poisoning the magnetite sample reducing the activity (see discussion on figure 30). Figure 33c showed a diminishing in the degradation test compared to the raw sample, it could be attributed to the raw magnetite was not completely wrapped by the chitosan giving it the highest activity in degradation of the amaranth red dye (50% of degradation at 150 min). However, after the ultrasonic treatment the samples presented loss in activity which can be attribute to the steric effect of the polyelectrolyte over the magnetite cluster. It is interesting that the same tendency of raw magnetite is presented in dispersed magnetite with chitosan where the highest activity were the magnetite dispersed by 1 cycle presenting a degradation of 44% at 150 minutes, then followed by the 4 cycles with chitosan (43% of degradation at 150 min) and the 8 cycles (41% of degradation at 150 min). (All the UV-Visible spectra of figure 33 are presented in the Appendix)

It made us to conclude that the steric effect plays a key role in the efficiency of magnetite for the degradation of the amaranth red dye where the raw magnetite presented the highest remotion activity followed by the magnetite@Chitosan and by last the magnetite@CTAC.
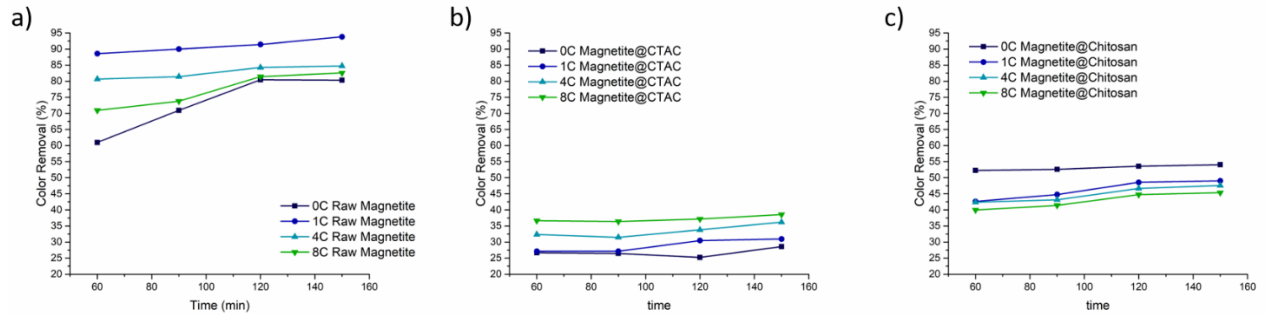
Figure 33. Color Removal of the different dispersion cycles of a) Raw Magnetite, b) Magnetite@CTAC, and c) Magnetite@Chitosan.

5.2.4 Degradation of a target molecule using photo Fenton and photocatalysis

Figure 34 shows the UV-Visible spectra of the degradation test using raw magnetite for one cycle using the same degradation conditions as presented in section 5.2.3. A finer analysis were performed analyzing for 5 min, 10 min, 20 min, 30 min, 60 min, 90 min, 120 min, and 150 min. Figure 34a shows the degradation tests without illumination (dark conditions) reaching a degradation maximum of 73% in 150 minutes. Figure 34b shows the raw magnetite dispersed by 1 cycle at dark conditions showing a degradation maximum of 91% in 150 minutes. These results corroborate the tendency showed in figure 34 where the raw magnetite dispersed by 1 cycle shows higher degradations compared to the magnetite without dispersion.
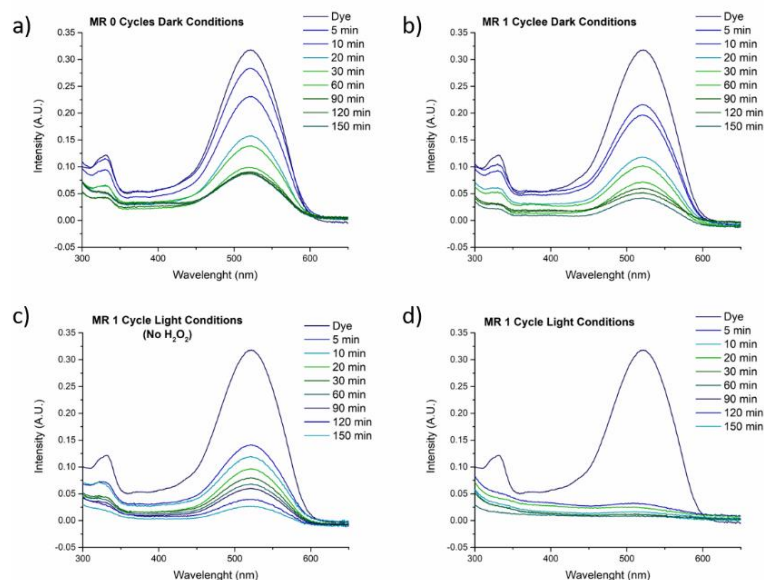
Figure 34. UV-Visible spectra of the degradation test using Raw Magnetite a) 0 Cycles-Dark Condition, b) 1 Cycle-Dark Condition. c) 1 Cycle No hydrogen peroxide-Light Condition, and d) 1 Cycle-Light Condition.

It is important to remark that one of the main reasons we selected amaranth red as target molecule was its low susceptibility to be photodegradated. An interesting effect was observed when was performed the same analysis using raw magnetite dispersed by 1 cycle, but changing the dark conditions for daylight illumination (3:00 PM to 5:30 PM, November 2018) and suppressing the hydrogen peroxide (see figure 34c). The analysis showed degradation maximum of 93% in 150 minutes, similar to the sample observed in figure 34b. It was observed a degradation of the target molecule, however the Fenton reaction needs the hydrogen peroxide in order to form the hydroxyl free radicals, then another mechanism acted in the advance oxidation process. Since the sample was under solar irradiance only two mechanism could be involved: photo-Fenton and photocatalysis.

As previously observed by the zeta potential measurements in section 5.2.2, negative charge of the dispersed raw magnetite could be attributed to the formation of hydroxyl and carboxyl groups on the iron sites, therefore the raw magnetite should present $[Fe(III)OH]^{2+}$ sites. The hydroxide group is important due to photo-Fenton reaction presented in the equation 14 (Minella et al., 2014).

In the other hand, it was reported by (Balberg & Pankove, 1971) that the magnetite nanoparticles presents a band gap of 2.6 eV, therefore the photocatalysis mechanism behind that activity could be attributed to

the pair electron-hole generation due to the interaction with light and therefore the generated holes can oxidize the water to form hydroxyl radicals.

The two mechanisms act in different regions of the solar spectrum, the photo-Fenton requires UV light (from 200 nm to 400 nm) while the photocatalysis requires around 416 nm (wavelength obtained by the conversion of 2.6 eV of band gap). As we do not filtered the light it is an opportunity area for continue this research.
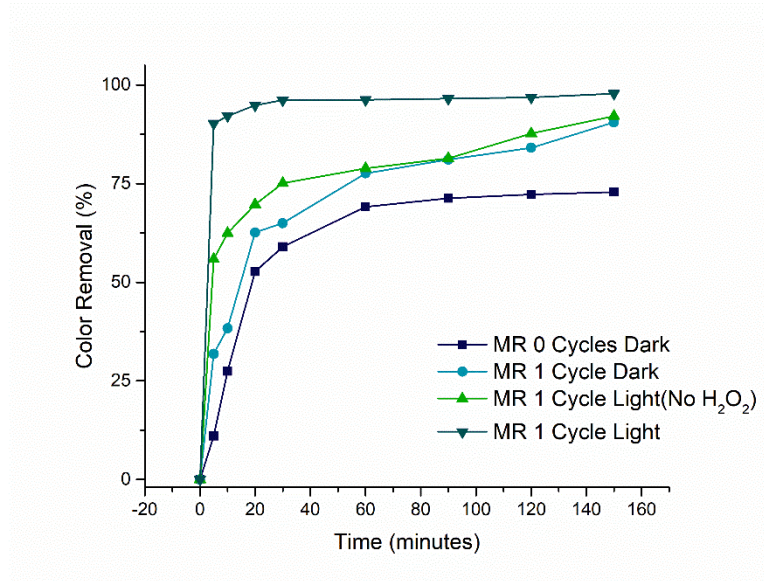
Figure 35. Color Removal summary plot.

The AOP enhanced by the solar light presented faster degradation rate compared to the Fenton reaction at dark conditions (see figure 35). In order to obtain a synergetic effect of the enhanced AOP and the Fenton reaction, it was realized a degradation test using the raw magnetite dispersed by 1 cycle under daylight illumination (3:00 PM to 5:30 PM, November 2018) without avoiding of the hydrogen peroxide (as presented in figure 34d). The degradation rate was the fastest compared to the previously 3, the analysis showed a degradation of 95% in 20 minutes, reaching a maximum of degradation of 98% in 150 min.

5.2.5 Degradation of treated wastewater from Tijuana city

The obtained synergy using the raw magnetite dispersed by 1 cycle under light conditions presented the highest and the fastest rate activity in the degradation of the target molecule (presented in section 5.2.3). Hence it was tested for degradation of reclaimed water obtained from PTAR (Planta de Tratamiento de Aguas Residuales) La Morita in the city of Tijuana (reclaimed water obtained in February 2019).

The obtained wastewater presented a yellowish color (see figure 57 in the appendix), when we performed an UV-Visible analysis observing a small absorption peak at 320 nm (see figure 36), however the absorption peak was too small for being the responsible of this yellowish color. Then we performed a fluorescence spectroscopy observing a broad emission peak (as observed in figure 36). It is important to remark that fluorescence is presented in organic molecules that contains aromatic systems, therefore the recalcitrant organic materials present aromatic systems.

For the degradation analysis, we concentrate the 0.01 wt. % of dispersed raw magnetite to 0.1 wt. % using a neodymium magnet (grade N52) and it was added to 10 mL of the reclaimed wastewater adding the hydrogen peroxide and the acetic acid in the same conditions as previously described. The analysis was tracked by fluorescence spectroscopy using the emission peak, even though the reduction in the emission peak does not imply the removal of organic recalcitrant materials, it implies that the aromatic system has been broken and is a good sign that the degradation system is working.
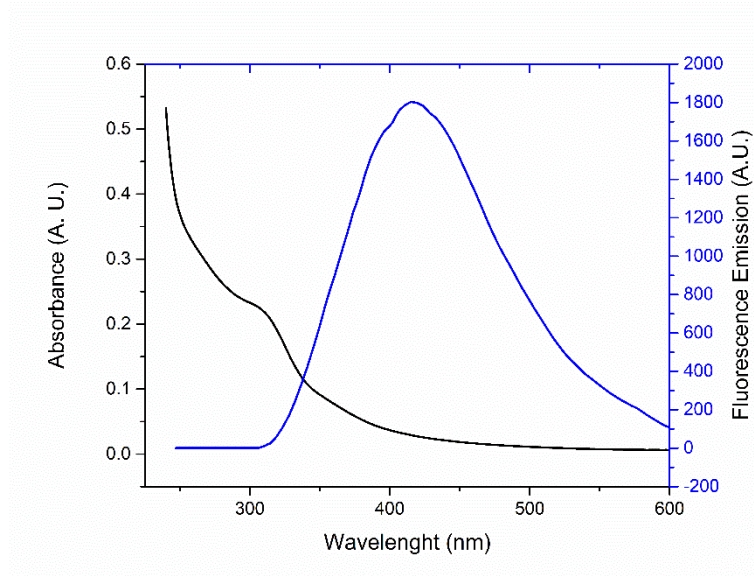
Figure 36. UV-Visible Spectra and Fluorescence Spectra of the Reclaimed Wastewater.

Figure 37 shows the comparison of degradation of reclaimed wastewater using raw magnetite without dispersion and the 1 cycle dispersed raw magnetite (degradation tests were performed in February 2019, between 12:00 PM to 3:00 PM). Figure 37b shows higher degradation rate compared to the raw magnetite without dispersion (figure 37a).
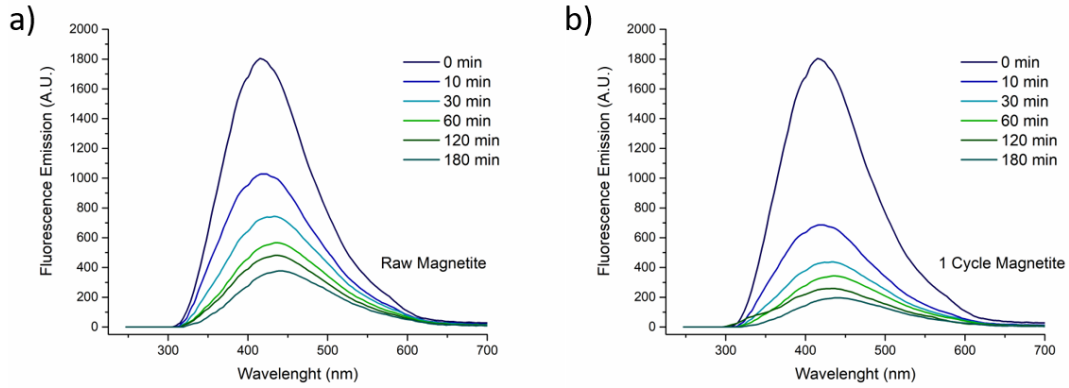
Figure 37. Fluorescence Removal using a) Raw Magnetite- Light Condition, and b) 1 Cycle dispersed Magnetite-Light Conditions.

The degradation rates are presented in figure 38 where the dispersed raw magnetite presented 89% of fluorescence removal compared to the raw magnetite without dispersion which presented 78% both samples at 180 minutes of treatment.

As this experiments are strongly dependent of the solar irradiance, especially in the UV range, we record the conditions of degradation using the UV index provided by the United States Environmental Protection Agency (EPA). The UV index for the reclaimed wastewater degradation was 4, approximately 100 mW/m^2 of irradiance in the UV range. For comparison in the last section 5.2.4 the UV index recorded was 6, approximately 150 mW/m^2 of irradiance in the UV range. Therefore, it is an opportunity area to exploit the synergetic effect UV light for the AOP at different UV irradiances.
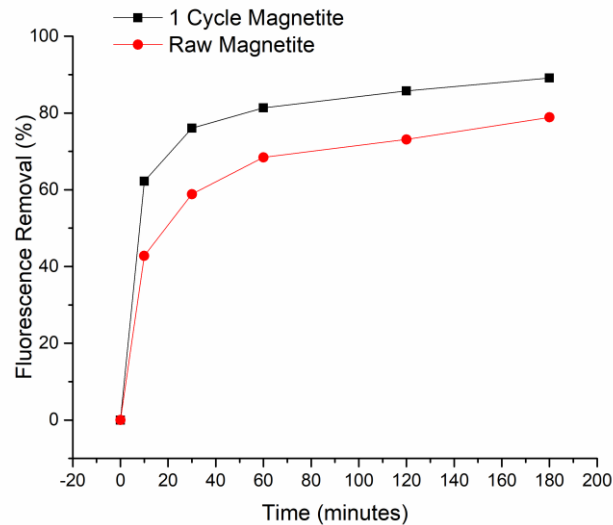
Figure 38. Comparison of the rate of fluorescence removal using Raw Magnetite vs. 1 Cycle dispersed Magnetite.

Since fluorescence it is not directly a measurement of degradation of recalcitrant organic carbon we performed an analysis of Chemical Oxygen Demand, in this analysis we can measure the quantity of organic carbon dissolved in the reclaimed wastewater, the measurement of the treated wastewater showed an initial value of 232 mg/L.

However, when the degradation samples were measured, they showed errors attributed to the acetic acid used for the acidification of the samples. The main problem was due to the AOP not only oxidized the recalcitrant organic molecules but also the acetic acid, therefore it was not possible to use a baseline of the COD of acetic acid. To solve this issue we took advantage of the acidic weakness of the acetic acid quantifying the acetic acid titrating against a strong base (as observed in figure 59 in the appendix). Then, we could subtract the COD contribution due to the acetic acid obtaining the degradation of organic carbon against time (see figure 39).
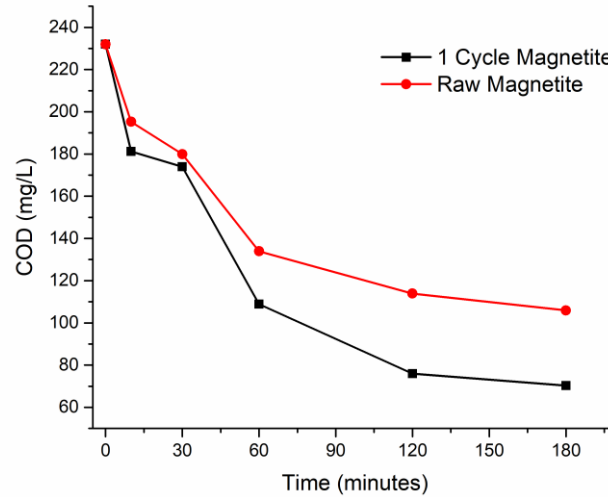
Figure 39. Chemical Oxygen Demand Analysis for the Raw Magnetite and 1 Cycle dispersed Magnetite.

The COD analysis (presented in figure 39) showed a higher activity for the dispersed raw magnetite presenting a COD reduction of 70% compared to the raw magnetite without dispersion which presented a COD reduction of 53%. This analysis corroborate the obtained results of the fluorescence removal and are coherent with the previously obtained results of the removal of the target molecule (see section 5.2.4).

Finally, in order to observe the reusability of the magnetite we performed stability tests. After the 180 minutes of degradation test, we proceeded to recover and to wash the used magnetite with deionized water precipitating them aided by the neodymium magnet and save them for the next day, we analyzed only the activity at 180 min for 10 days as observed in figure 40.

Interestingly the raw magnetite showed the same activity for the ten days, it could due to the synergetic effect, while the Fenton reaction oxidizes the Fe(II) to Fe(III) the photo-Fenton reduce the iron from Fe(III) to Fe(II) which maintained the balance of Fe(II)/Fe(III).
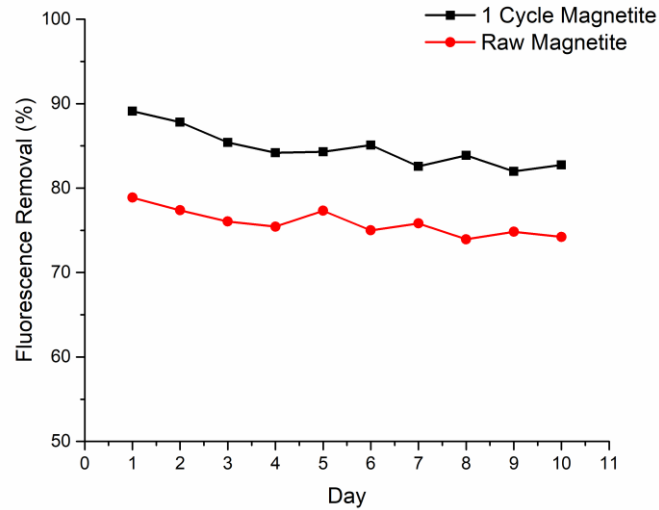
Figure 40. Stability test of the fluorescence removal activity using Raw Magnetite and 1 Cycle dispersed Magnetite through 10 days.

Section Conclusions

The ultrasonic probe disaggregates the clusters into small clusters which allowed to increase the active surface area. It was tested different dispersion cycles for the disaggregation, observing that the best activity for removal of a target molecule was the dispersed nanoparticles using 1 cycle of ultrasonic treatment, it could be attributed to the sonochemical effect caused by the sonic probe.

The halogen contained in neutral salts showed an adsorption effect on the nanoparticles surface, this allowed us to correlate this adsorption effect with the decrease in activity presented by CTAC stabilized nanoparticles which were poisoned by the halides.

The best activity for removal of a target molecule was observed for the raw magnetite dispersed by 1 cycle of ultrasound. The raw magnetite presented a synergetic effect of Fenton, photo-Fenton, and photocatalysis which enhanced the activity when it was irradiated with solar illumination. Afterward, the raw magnetite dispersed by 1 cycle of ultrasound was tested for the removal of recalcitrant organic molecules present in reclaimed wastewater showing the synergetic effect.

Finally, the Raw Magnetite and the 1 Cycle dispersed Magnetite were tasted for recycling stability tests, the activity of the dispersed magnetite remained higher compared to the raw magnetite without dispersion when they were analyzed by fluorescence spectroscopy through 10 days.

5.3 Anchorage of magnetite nanoparticles onto Carbon Nanotubes

5.3.1 State of the Art

5.3.1.1 Anodic membranes made of carbon nanotubes for cleaning water

The first reactor for in situ electrochemistry for cleaning water using buckypapers was obtained by Vecitis, Gao, & Liu, 2011 using MWCNT buckypapers as filter for adsorption and oxidation of pollulant dyes. Figure 41 shows the schematic of the reactor which used a stainless steel mesh as cathode and a MWCNT buckypapers for the dye oxidation.
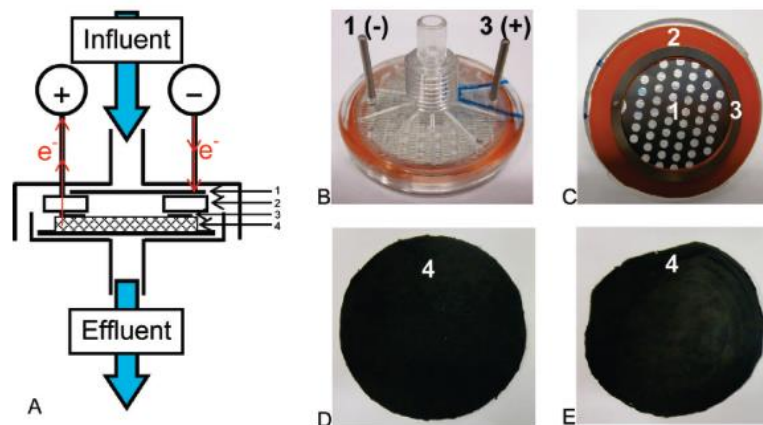
Figure 41. Buckypaper Reactor of Chad Vecitis (image taken from *Vecitis, Gao, & Liu, (2011)*).

Vecitis et al. studied two dyes: methylene blue and methyl orange (as observed in figure 42a and figure 42b respectivley). In both cases it is observed that +1 V was not enough for the oxidation of those dyes.

However, when it was used high anodic potentials (+2 V and +3 V) it was observed an enhancement in the degradation rate for the dyes.
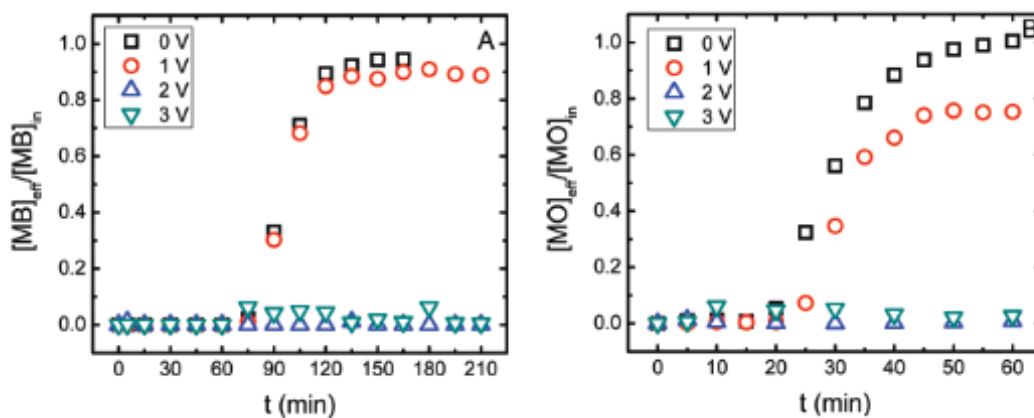
Figure 42. Degradation curves using the buckypaper reactor for the removal of a) Methylene Blue and b) Methyl Orange (image taken from *Vecitis, Gao, & Liu, (2011)*).

Gao & Vecitis in 2012 studied three different types of carbon nanotubes C-CNT (typical multi-walled carbon nanotubes), B-CNTS (boron-doped carbon nanotubes), and N-CNT (nitrogen-doped carbon nanotubes) for the phenol degradation using a similar reactor as the one observed in figure 43. The obtained results presented similar activity for the phenol oxidation as observed in figure 42, however, they observed that the phenol started a polymerization and further precipitation to form polyphenols species.
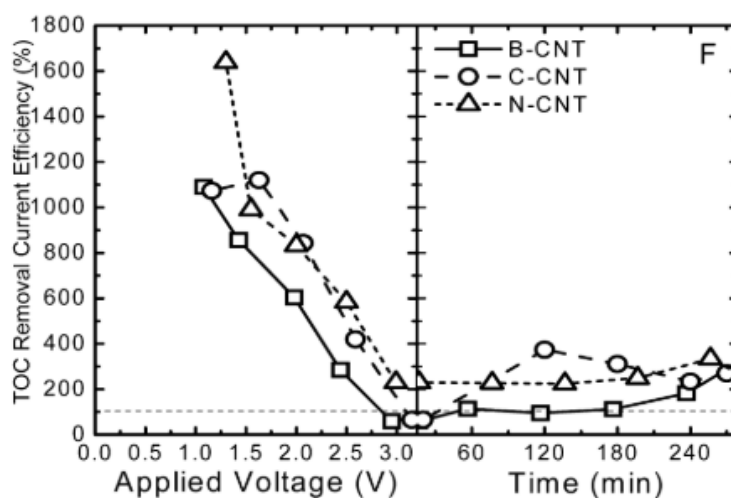
Figure 43. Removal of Phenol Target Molecule tracked by TOC using different doped-carbon nanotubes (image taken from *Gao & Vecitis (2012)*).

Gao & Vecitis in 2012 studied the difference between a batch reactor versus a flux reactor, using for cathode a matrix of stainless steel and as anode the CNTs buckypaper for phenol remotion. They observed (as shown in figure 44) that the removal of phenol measured by TOC was considerable low in the batch reactor compared to the flow reactor this is attributed to the flow through the buckypaper.
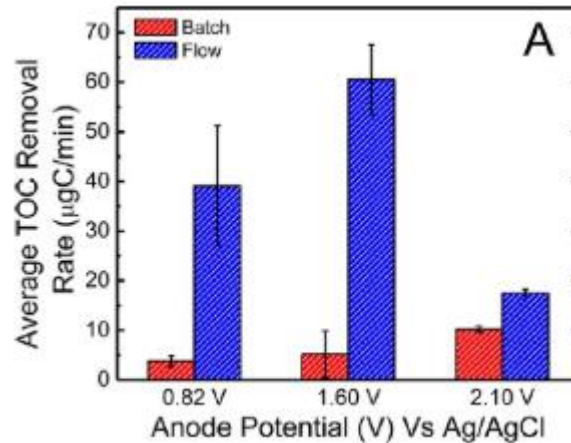
Figure 44. TOC Removal comparing the Batch Reactor against the Flow Reactor at different Anode Potentials (image taken from *Gao & Vecitis (2012)*).

5.3.1.2 Cathodic membranes made of carbon nanotubes for cleaning water

Many researchers have been studying the oxygen reduction reaction aiming for the four-electron pathway for fuel cell applications. The use of cathodic buckypapers for the hydrogen peroxide production is very limited, in this sense, Liu, Xie, Ong, Vecitis, and Zhou, 2015 fabricated a flow electrochemical rector using buckypapers made of MWCNTs as cathode and anode (system MWCNT/MWCNT) for the remotion study of phenol contaminant. They used the anode to oxidize the target molecule, placing the buckypapers close to the influent. For the cathode, they took advantage of the oxygen reduction reaction for the hydrogen peroxide production, which is a strong oxidant (E = 1.7 V). In figure 45 is observed the ORR for the cathode buckypaper at different oxygen fluxes (buckypapers area of 706 mm^2)
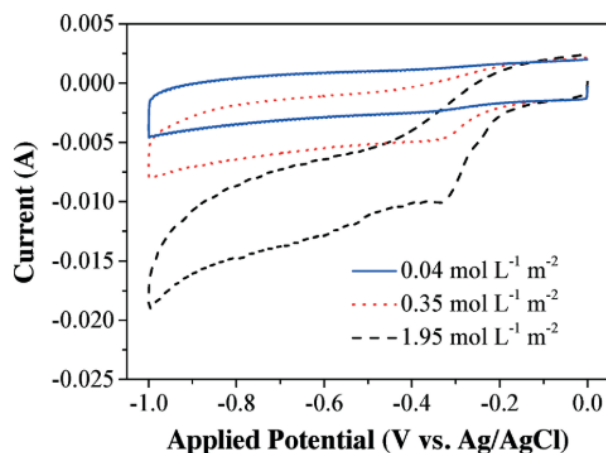
Figure 45. CV of a MWCNT buckypaper as cathode for the ORR. (image taken from *Liu, Xie, Ong, Vecitis, and Zhou, (2015)*).

It is remarkable to say that the research of cleaning wastewater using buckypapers are mostly of remotion of target molecules pollulants (such dyes, phenols, etc) and have not started using reclaimed wastewater. Moreover, most of the fabricated reactors use the buckypapers as anodes to oxidize the pollulant molecule using high electric potentials. The only reactor fabricated using the buckypapers as cathode did not take advantage of the electrofenton, they used the hydrogen peroxide obtained as an oxidant to assist the anode.

Another interesting point is that the use of nitrogen-doped carbon nanotubes was not fully exploited because it was used as anode instead of cathode. The lack of research using the nitrogen doped carbon nanotubes for wastewater treatment can be due to the nitrogen sites influence in the ORR pathway (two or four electrons) recently unraveled, making nitrogen-doped carbon nanotubes a promising 3D cathode for electrofenton.

5.3.2 Wrapping Carbon Nanotubes with a polyelectrolyte

The wrapping of MWCNTs was prepared following three steps. First, we dispersed 50 g of the obtained CNTs soot in water using the hydrothermic method to completely disperse the forest-like arrays of CNTs that comes inherently to the synthesis. (Contreras et al., 2019) The obtained dispersions was concentrated by centrifugation until reaching 100 mL and a concentration of 0.5 mg/mL. Afterwards, a polyelectrolyte

solution was prepared adding 4 wt.% of medium molecular weight Poly-(sodium 4-styrenesulfonate) (PSS) and 0.5 M of NaCl under vigorous stirring. The wrapping was performed out by dripping 1:1 v/v the CNTs dispersion to the PSS solution under vigorous stirring and left stirring overnight.(Correa-Duarte, Sobal, Liz-Marzán, & Giersig, 2004; Pastoriza-Santos, Pérez-Juste, & Liz-Marzán, 2006)

The sample was analyzed by Zeta potential. The figure 46 shows the zeta potential analysis where it can be observed the negative charge of the MWCNT@PSS of -36 mV due to the sulfonate groups of the polyelectrolyte (R-SO$_3^-$). The excess of PSS was removed by centrifugation obtaining 200 mL of the CNTs@PSS dispersion, this procedure was realized twice in order to fabricate two buckypapers. The obtained dispersion was saved for further assembly.
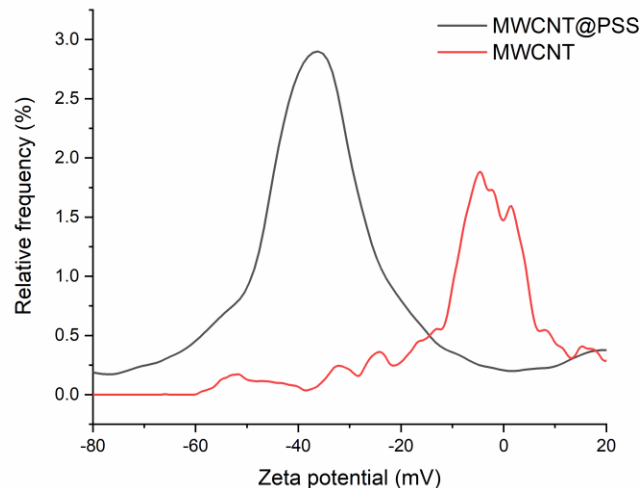
Figure 46. Zeta potential of wrapped MWCNT with PSS compared to the pristine MWCNT.

5.3.3 Anchorage of Magnetite Nanoparticles on wrapped CNTs

The highest activity for a dispersed magnetite wrapped with chitosan (magnetite@chitosan), as previously presented in section 5.2.3, was the dispersed by 1 cycle. The TEM microscopy of these nanoparticles (magnetite@chitosan) are showed in figure 46. Before the dispersion we can observe a big cluster (as observed in figure 47a and figure 47b) while after the ultrasonic processing the magnetite cluster size was

reduced to a smaller one (as observed in figure 47c and figure 47d). They presented an excess of the polyelectrolyte, therefore we proceeded to wash the wrapped nanoparticles.
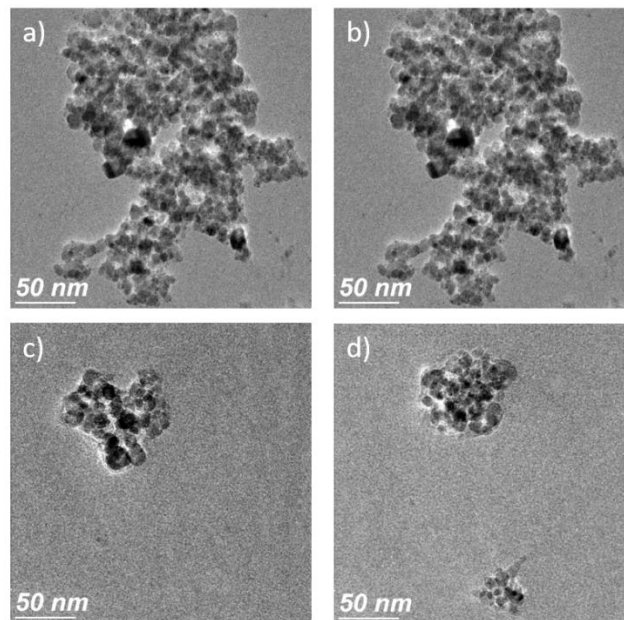
Figure 47. a) and b) are TEM images of the magnetite without ultrasonic dispersion c) and d) are TEM images of the smaller clusters after the ultrasonic treatment at 1 cycle.

The washing process was precipitating the nanoparticles with a N52 Neodymium magnet and removing the supernatant (1:4). The nanoparticles were redispersed with deionized water (1 wash), the same washing process was repeated one to four obtaining a second washed sample (2 washing cycles). In order to observe if the polyelectrolyte was not completely removed, we performed a zeta potential analysis as presented in figure 48, where the magnetite@chitosan without any washes presented +48 mV of zeta potential, after one wash it presented +46 mV and the second wash presented +39 mV. The reduction of surface charge could be attributed to the reduction of the chitosan.
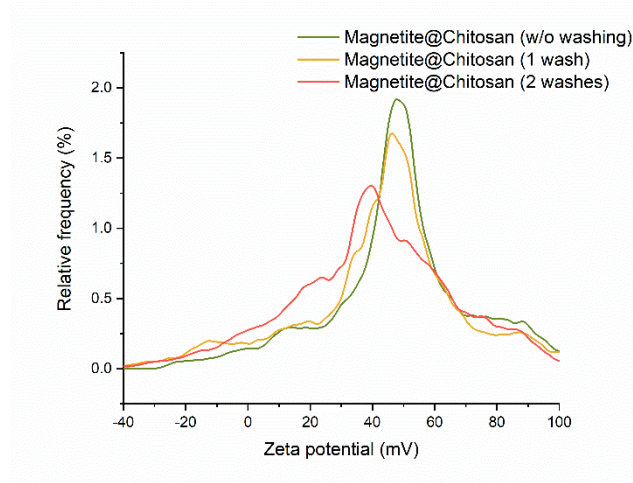
Figure 48. Zeta Potential Analysis of several Magnetite@Chitosan Washes.

Since the analysis of the washing showed to be stable on the surface charge, we proceeded to scale up the dispersion for further anchoring. The raw nanoparticles were dispersed by 1 probe sonication cycle using chitosan of 0.01 wt. % magnetite. The samples were concentrated in order to obtain 200 mL of 0.05 wt. % and 200 mL of 0.1 wt. % of 1 cycle magnetite@chitosan which were saved for posterior anchoring over the MWCNT@PSS.

5.3.4 Assembly of the reactive membrane (Buckypaper)

The assembly of the buckypaper required two steps: First, the anchorage of the washed magnetite@chitosan (+39 mV of zeta potential) to the MWCNTs@PSS (-36 mV of zeta potential) by electrostatic charges.

The buckypaper was obtained by dripping the magnetite@chitosan dispersion (0.05 wt. % or 0.1 wt. %) over the CNT@PSS dispersion and kept under vigorous stirring for 3 h. Second, the buckypaper assembly was made by vacuum assisted filtration of the mixture.

Besides those buckypapers, it was also fabricated two more buckypapers, the first one using the nitrogen-doped carbon nanotubes synthesized at 900 C (CNx900) and the second one using multiwalled carbon nanotubes (MWCNT). The buckypapers obtained have a circular shape as it can be observed in figure 49a,

after the buckypaper fabrication we trimmed the circumscribed square, and selected three different areas in the square: A1 with ~0.25cm2; A2 with ~1cm2 and A3 with ~2.25cm2 (shown in figure 49b). The three different trimmed squares can be seen in figure 98c.
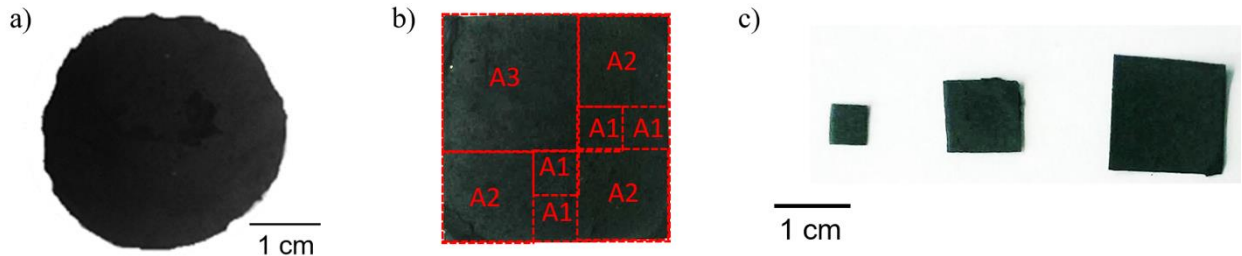
Figure 49. It is observed a) picture of a buckypaper, b) areas selected for trimming and c) the trimmed buckypaper squares.

5.3.5 Degradation of treated wastewater from the city of Tijuana using the prototype reactor

In order to test the obtained buckypapers for degradation of reclaimed wastewater, we fabricated a prototype reactor using a 3D printer. The prototype reactor consisted mainly of two electrodes: The cathode is the responsible for the hydrogen peroxide production (via oxygen reduction reaction), and the anode which closes the circuit and favor the Fenton reaction (via Fe^{2+}) as shown in figure 50. The reclaimed wastewater used for this analysis were obtained by CESPT PTAR La Morita (June 2019)

For the cathode we selected two trimmed buckypapers of 1 cm^2, the BP-CNx900 which presented the highest activity for the hydrogen peroxide production and the BP-MWCNT as a control buckypaper. The anode was made using 1 cm^2 trimmed buckypaper MWCNT@Fe_3O_4 (using the 0.05 wt. % or 0.1 wt. % of magnetite)

The voltage bias was applied in the electrodes connecting them to a power supply, the anode was connected to the positive terminal and the cathode to the negative terminal. In order to assure the -0.9 V vs. Ag/AgCl, we measure the cathode voltage with a Ag/AgCl reference electrode near to the influent. The

-0.9 V vs. Ag/AgCl was obtained by measuring the 1 cm^2 trimmed CNx900 electrode by cyclic voltammetry, observing the cathodic peak (Epc) at -0.9 V vs. Ag/AgCl the shifting to more negative potentials is due to the area of the buckypaper (see cyclic voltammetry in figure 60 in appendix).
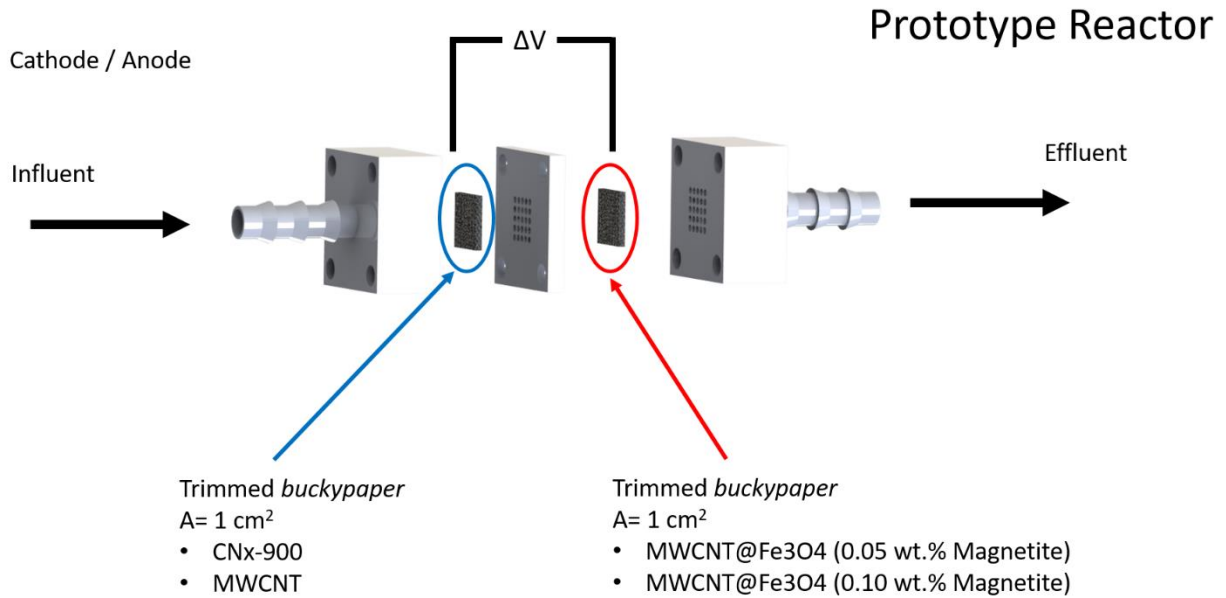
Figure 50. Prototype Reactor (the blue circle at the left shows the cathode and the red circle at the right shows the anode.

We performed an UV-Visible and fluorescence spectroscopy as shown in figure 51 of the initial reclaimed water. It is observed the same behavior as the one observed in the reclaimed water in section 5.2, however this time the water was less contaminated than the water obtained in February.
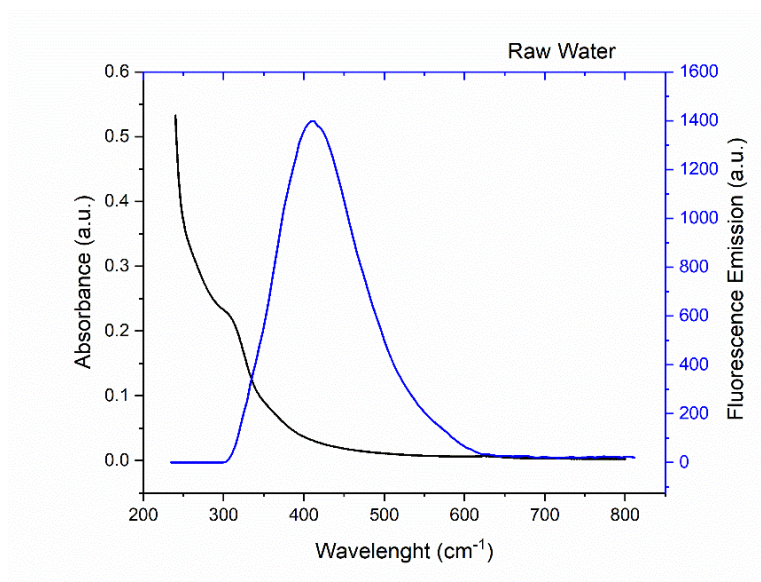
Figure 51. UV-Visible Spectra and Fluorescence Spectra of the Reclaimed Wastewater.

Figure 52 shows the fluorescence removal of the reclaimed wastewater using different cathode/anode system applied in the prototype reactor. Black curve is the fluorescence of the raw water, the blue line represents the measurement of the water filtered through the reactor (without the application of electrical potential), and the red line represents the measurement of the water after the application of a voltage bias. It is important to remark that the flux of water was measured in 5 mL per minute.
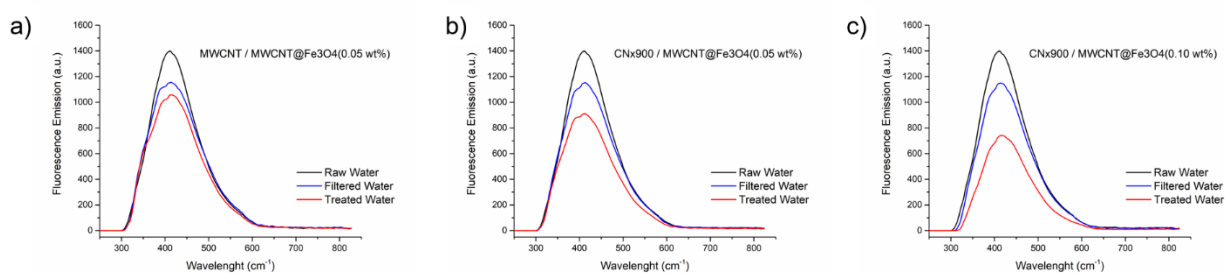
Figure 52. Shows the fluorescence removal by changing the electrode systems.

Figure 52a shows the system 1 which was MWCNT/MWCNT@Fe_3O_4 (containing 0.05 wt. % of magnetite) presenting a 17% of remotion of fluorescent organic molecules when the raw water was only filtered through the electrodes, however when the potential was applied it was observed a 24% of fluorescence

removal. In the figure 52b it was changed the cathode from the MWCNT to the CNx900 and maintaining the same anode (system 2: CNx900/ MWCNT@Fe_3O_4 containing 0.05 wt. % of magnetite), it was observed that the filtering presented 18% of fluorescence removal which was almost the same as the previous system, but when it was applied a voltage bias the fluorescence removal was enhanced to 35%, it could be attribute to the nitrogen species in the nanotubes that favored the hydrogen peroxide production at lower potentials. With that in mind, we maintained the CNx900 buckypaper as the cathode in the system 3, but we changed the anode for the MWCNT@Fe_3O_4 (containing 0.1 wt. % of magnetite) as shown in figure 52c. For the filtration the fluorescence removal remained in 18% while the fluorescence removal after applied potential was 47%.

The enhancement in the fluorescence removal could be attributed to the nitrogen sites in the CNx nanotubes that allowed the hydrogen peroxide production at lower potentials and the increment in the magnetite content which increased the quantity of the active sites for the Fenton reagent generation.

It is important to remark that the fluorescence removal is only the rupture of aromatic systems, therefore in order to obtain information about the organic molecules contained in the reclaimed wastewater (either fluorescent or non-fluorescent) we performed the Chemical Oxygen Demand and the Total Organic Carbon.

Figure 53 presents the COD analysis where the raw water presented an oxygen demand of 129 mL of oxygen per liter to completely remove the organics dissolved in water. When the raw water was just filtered through the system 1 it was observed a 19% of removal while when the potential was applied, we observed a 31% of removal. When we analyzed the system 2 we observed for the filtered a 19% of removal which was similar to the system 1, however an enhancement of degradation reaching 51% was achieved. Finally, we performed the same analysis for system 3, observing a 16% of removal for the filtering but an enhancement of 60% when it was applied the voltage bias.

The differences between the fluorescence removal and the COD is primary due to the fact that some molecules can present fluorescence if they present an aromatic system (such as benzene, antracene, phenol, etc.), however if they don't (such as furan, thiophene, pyrrole, etc.) they will not presentate fluorescence, therefore the water sample obtained tell us that it contained more aromatic compounds than non-aromatic.
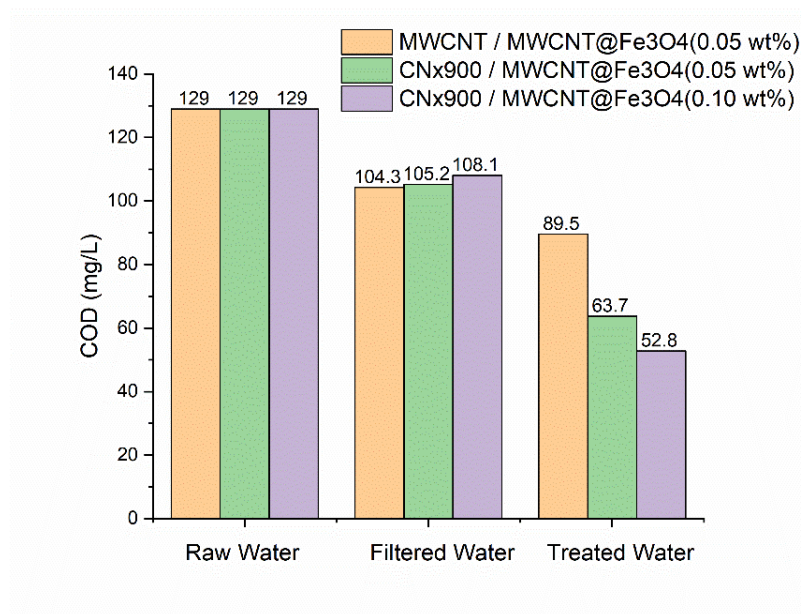
Figure 53. Chemical Oxygen Demand Removal by changing the electrode systems in the prototype reactor.

The total organic carbon analysis (presented in figure 54) showed 60 mg/L of TOC dissolved in water, the three system presented a 14% of TOC degradation when the water was only filtered, and a similar trend than the one observed for COD was obtained once the voltage was applied. System 1 reached 31%, system 2 reached 54%, and system 3 reached 59%.
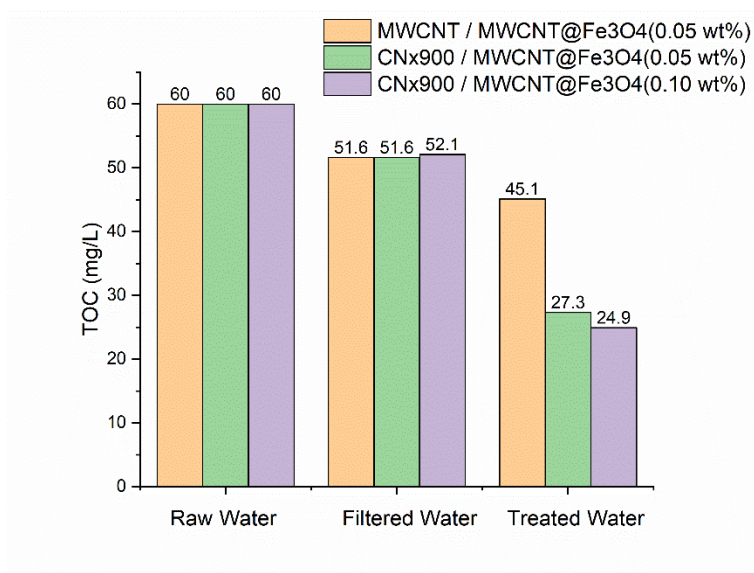
Figure 54. Total Organic Carbon Removal by changing the electrode systems in the prototype reactor.

Section Conclusions

The wrapping of the PSS over the carbon nanotubes showed to be functional, maintaining the physicochemical properties of the carbon nanotubes. It was proven by the zeta potential analysis that the MWCNT wrapped with PSS acquired a negative surface charge. The magnetite nanoparticles coating with positive charged chitosan showed to be efficient due to the resistance to lose surface charge observed in the zeta potential.

The assembly of the buckypapers using the electrostatic charges was made successfully, therefore, the reactive membrane was successfully assembled.

The prototype reactor showed to be efficient for the removal of recalcitrant pollutants in the reclaimed wastewater measured by the fluorescence spectroscopy, chemical oxygen demand, and total organic carbon.

Chapter 6. General Conclusions and Future Perspectives

The graphitic Nitrogen specie is active for the oxygen reduction reaction, and also is selective to the two-electron pathway which led us to improve the *in-situ* hydrogen peroxide production by the electrochemistry via. Also, it was proposed a mechanism that explained how graphitic Nitrogen is selective for the two-electron pathway by an organic chemical reaction mechanism an proved by density functional theory calculations.

The dispersed magnetite showed to be active for the Fenton reaction, taking advantage of its mixed valence states it was improved not only the Fenton reaction but the photo-Fenton and photocatalysis.

The prototype reactor showed to be efficient for the removal of organic recalcitrant pollulants obtained in the reclaimed water from PTAR La Morita, by exploiting the capability of hydrogen production of the nitrogen-doped carbon nanotubes and the magnetite´s ability to reduce the hydrogen peroxide into hydroxyl free radicals for improving the advanced oxidation process.

There still some much field to explore, the doped carbonaceous materials can still being improved by changing the dopant atoms (such as Nitrogen, Boron, Sulphur,etc), incrementing the quantity of dopant, and varying the ratio of the nitrogen species.

Even though the prototype reactor showed to be efficient for the removal of reclaimed wastewater, it still needs more research to improve the technology. Scientific work still needed such as: i) Increment of hydrogen production ii) take advantage of the synergetic effect of the magnetite. The engineering part still need further work to surpass the capabilities of the technology developed in this doctoral thesis, such as: i) the residence time, ii) lifespan of the reactive membranes, etc.

Finally, I would like to address that these buckypapers made with nitrogen-doped carbon nanotubes can be applied for the developing of different technologies in the energy and environmental areas, such as: solar harvesting, storing energy, hydrogen production, fuel cells, biofuel cells and biosensing.

References

Alvizo-Paez, E. R., Romo-Herrera, J. M., Terrones, H., Terrones, M., Ruiz-Garcia, J., & Hernandez-Lopez, J. L. 2008. Soft purification of N-doped and undoped multi-wall carbon nanotubes. *Nanotechnology*, *19,* 15, 155701.

Ameta, R., Chohadia, A. K., Jain, A., & Punjabi, P. B., 2018. Fenton and Photo-Fenton Processes. In *Advanced Oxidation Processes for Wastewater Treatment: Emerging Green Chemical Technology*.

Ameta, R., Solanki, M. S., Benjamin, S., & Ameta, S. C., 2018. Photocatalysis. In *Advanced Oxidation Processes for Wastewater Treatment: Emerging Green Chemical Technology*.

Ameta, S. C., 2018. Introduction. *Advanced Oxidation Processes for Wastewater Treatment: Emerging Green Chemical Technology*, 1–12.

Avetta, P., Pensato, A., Minella, M., Malandrino, M., Maurino, V., Minero, C., … Vione, D., 2015. Activation of Persulfate by Irradiated Magnetite: Implications for the Degradation of Phenol under Heterogeneous Photo-Fenton-Like Conditions. *Environmental Science & Technology*, *49*, 1043–1050.

Balberg, I., & Pankove, J. I., 1971. Cathodoluminescence of Magnetite. *Physical Review Letters*, *27*(20), 1371–1374.

Bhattacharyya, S., Auciello, O., Birrell, J., Carlisle, J. A., Curtiss, L. A., Goyette, A. N., … Zapol, P. 2001. Synthesis and characterization of highly-conducting nitrogen-doped ultrananocrystalline diamond films. *Applied Physics Letters*, *79*, 1441–1443.

Bulusheva, L. G., Okotrub, A. V., Kinloch, I. A., Asanov, I. P., Kurenya, A. G., Kudashov, A. G., … Song, H., 2008. Effect of nitrogen doping on Raman spectra of multi-walled carbon nanotubes. *Physica Status Solidi B Basic Research*, *245*, 1971–1974.

Cheremisinoff, N. P., 1997. Handbook of water and wastewater treatment technology. In *Journal of Hazardous Materials*, Vol. 53.

Contreras, E.,2015. *Diseño de un proceso para la obtención de papeles a base de nanotubos de carbono buckypaper, Tesis de Maestría en Ciencias,*.CICESE.

Contreras, E., Dominguez, D., Tiznado, H., Guerrero-Sanchez, J., Takeuchi, N., Alonso-Nunez, G., … Romo-Herrera, J. M., 2019. N-Doped carbon nanotubes enriched with graphitic nitrogen in a buckypaper configuration as efficient 3D electrodes for oxygen reduction to H 2 O 2. *Nanoscale*, *11*, 2829–2839.

Correa-Duarte, M. A., Sobal, N., Liz-Marzán, L. M., & Giersig, M., 2004. Linear assemblies of silica-coated gold nanoparticles using carbon nanotubes as templates. *Advanced Materials*, *16*, 2179–2184.

Czerw, R., Terrones, M., Charlier, J. C., Blase, X., Foley, B., Kamalakaran, R., … Carroll, D. L., 2001. Identification of Electron Donor States in N-Doped Carbon Nanotubes. *Nano Letters*, *1*, 457–460.

Das, R., Vecitis, C. D., Schulze, A., Cao, B., Ismail, A. F., Lu, X., … Ramakrishna, S., 2017. Recent advances in nanomaterials for water protection and monitoring. *Chemical Society Reviews*, *46*, 6946–7020.

Endo, M., Muramatsu, H., Hayashi, T., Kim, Y., Terrones, M., & Dresselhaus, M. S., 2005. "Buckypaper" from coaxial nanotubes. *Nature*, *433*, 476.

Fellinger, T. P., Hasché, F., Strasser, P., & Antonietti, M., 2012. Mesoporous nitrogen-doped carbon for the electrocatalytic synthesis of hydrogen peroxide. *Journal of the American Chemical Society*, *134*, 4072–4075.

Gao, G., & Vecitis, C. D., 2012a. Doped carbon nanotube networks for electrochemical filtration of aqueous phenol: Electrolyte precipitation and phenol polymerization. *ACS Applied Materials and Interfaces*, *4*, 1478–1489.

Gao, G., & Vecitis, C. D., 2012b. Reactive depth and performance of an electrochemical carbon nanotube network as a function of mass transport. *ACS Applied Materials and Interfaces*, *4*, 6096–6103.

Giannozzi, P., Car, R., & Scoles, G., 2003. Oxygen adsorption on graphite and nanotubes. *Journal of Chemical Physics*, *118*, 1003–1006.

Gligorovski, S., Strekowski, R., Barbati, S., & Vione, D., 2015. Environmental Implications of Hydroxyl Radicals •OH. *Chemical Reviews*, *115*, 13051–13092.

Gong, K., Du, F., Xia, Z., Durstock, M., & Dai, L., 2009. Nitrogen-doped carbon nanotube arrays with high electrocatalytic activity for oxygen reduction. *Science*, *323*, 760–764.

Gong, K., Du, F., Xia, Z., Durstock, M., & Dai, L., 2009. Nitrogen-Doped Carbon Nanotube Arrays with High Electrocatalytic Activity for Oxygen Reduction. *Science*, *323*, 760–764.

González, I. Z., Valenzuela-Muñiz, A. M., Alonso-Nuñez, G., Farías, M. H., & Gómez, Y. V., 2017. Influence of the Synthesis Parameters in Carbon Nanotubes Doped with Nitrogen for Oxygen Electroreduction. *ECS Journal of Solid State Science and Technology*, *6*, M3135–M3139.

Guo, D., Shibuya, R., Akiba, C., Saji, S., Kondo, T., & Nakamura, J., 2016. Active sites of nitrogen-doped carbon materials for oxygen reduction reaction clarified using model catalysts. *Science*, *351*, 361–365.

Haber, F., & Weiss, J. 1932. *The Catalytic Decom position o f Hydrogen Peroxide by Iron Salts **. 332–351.

Han, W. Q., Kohler-Redlich, P., Seeger, T., Ernst, F., Rühle, M., Grobert, N., … Terrones, H., 2000. Aligned CNxnanotubes by pyrolysis of ferrocene/C60under NH3atmosphere. *Applied Physics Letters*, *77*, 1807–1809.

Iglesias, D., Giuliani, A., Melchionna, M., Marchesan, S., Criado, A., Nasi, L., … Fornasiero, P., 2018. N-Doped Graphitized Carbon Nanohorns as a Forefront Electrocatalyst in Highly Selective O 2 Reduction to H 2 O 2. *Chem*, *4*, 106–123.

Ismagilov, Z. R., Shalagina, A. E., Podyacheva, O. Y., Ischenko, A. V., Kibis, L. S., Boronin, A. I., … Tkachev, E. N., 2009. Structure and electrical conductivity of nitrogen-doped carbon nanofibers. *Carbon*, *47*, 1922–1929.

Kusunoki, I., Sakai, M., Igari, Y., Ishidzuka, S., & Takami, T., 2001. *XPS study of nitridation of diamond and graphite with a nitrogen ion beam*. *492*, 315–328.

Lai, L., Potts, J. R., Zhan, D., Wang, L., Poh, C. K., Tang, C., … Ruoff, R. S., 2012. Exploration of the active center structure of nitrogen-doped graphene-based catalysts for oxygen reduction reaction. *Energy & Environmental Science*, *5*, 7936.

Le, T. X. H., Bechelany, M., Lacour, S., Oturan, N., Oturan, M. A., & Cretin, M., 2015. High removal efficiency of dye pollutants by electron-Fenton process using a graphene based cathode. *Carbon*, *94*, 1003–1011.

Lim, S. H., Elim, H. I., Gao, X. Y., Wee, A. T. S., Ji, W., Lee, J. Y., & Lin, J., 2006. Electronic and optical properties of nitrogen-doped multiwalled carbon nanotubes. *Physical Review B - Condensed Matter and Materials Physics*, *73*, 1–6.

Liu, Y., Xie, J., Ong, C. N., Vecitis, C. D., & Zhou, Z., 2015. Electrochemical wastewater treatment with carbon nanotube filters coupled with: In situ generated H2O2. *Environmental Science: Water Research and Technology*, *1*, 769–778.

Maldonado, S., Morin, S., & Stevenson, K. J., 2006. Structure, composition, and chemical reactivity of carbon nanotubes by selective nitrogen doping. *Carbon*, *44*, 1429–1437.

Melgar-Lopez, M., & Cambreros-Urbina, A., 2017. *Diagnóstico socioambiental para el Programa del Manejo Integral del Agua de la Cuenca del Río Tijuana* . Recuperado en septiembre de 2019 de: http://www.cuencariotijuana.org/wp-content/uploads/2017/03/DiagnosticoCRT.pdf

Minella, M., Marchetti, G., De Laurentiis, E., Malandrino, M., Maurino, V., Minero, C., … Hanna, K., 2014. Photo-Fenton oxidation of phenol with magnetite as iron source. *Applied Catalysis B: Environmental*, *154–155*, 102–109.

Myers, R. L., 2007. The 100 Most Important Chemical Compounds: A Reference Guide. In *Greenwood Publishing Group: Westport*.

Nerud, F., Baldrian, P., Gabriel, J., & Ogbeifun, D., 2001. Decolorization of synthetic dyes by the Fenton reagent and the Cu/pyridine/H2O2 system. *Chemosphere*, *44*, 957–961.

Pastoriza-Santos, I., Pérez-Juste, J., & Liz-Marzán, L. M., 2006. Silica-coating and hydrophobation of CTAB-stabilized gold nanorods. *Chemistry of Materials*, *18*, 2465–2467.

Pels, J. R., Kapteijn, F., Moulijn, J. A., Zhu, Q., & Thomas, K. M., 1995. Evolution of nitrogen functionalities in carbonaceous materials during pyrolysis. *Carbon*, *33*, 1641–1653.

Qu, L., Liu, Y., Baek, J.-B., & Dai, L., 2010. Nitrogen-Doped Graphene as Efficient Metal-Free Electrocatalyst for Oxygen Reduction in Fuel Cells. *ACS Nano*, *4*, 1321–1326.

Raymundo-Piñero, E., Cazorla-Amorós, D., Linares-Solano, A., Find, J., Wild, U., & Schlögl, R., 2002. Structural characterization of N-containing activated carbon fibers prepared from a low softening point petroleum pitch and a melamine resin. *Carbon*, *40*, 597–608.

Rigueur, J. L., Hasan, S. a., Mahajan, S. V., & Dickerson, J. H., 2010. Buckypaper fabrication by liberation of electrophoretically deposited carbon nanotubes. *Carbon*, *48*, 4090–4099.

Rinzler, a. G., Liu, J., Dai, H., Nikolaev, P., Huffman, C. B., Rodríguez-Macías, F. J., … Smalley, R. E. 1998. Large-scale purification of single-wall carbon nanotubes: process, product, and characterization. *Applied Physics A: Materials Science & Processing*, *67*, 29–37.

Saldivar, L., & Walsh, C., 2015. Nanotecnología para el tratamiento de agua. Claves sobre la investigación en México. *Mundo Nano*, *8*, 53–69.

Sidik, R. A., Anderson, A. B., Subramanian, N. P., Kumaraguru, S. P., & Popov, B. N., 2006. O2 reduction on graphite and nitrogen-doped graphite: Experiment and theory. *Journal of Physical Chemistry B*, *110*, 1787–1793.

Song, C., & Zhang, J., 2008. *PEM Fuel Cell Electrocatalysts and Catalyst Layers* Vol. 53; J. Zhang, 3

Sorescu, D. C., Jordan, K. D., & Avouris, P. 2001. Theoretical study of oxygen adsorption on graphite and the 8,0 single-walled carbon nanotube. *Journal of Physical Chemistry B*, *105*, 11227–11232.

Srivastava, D., & Laasonen, K., 2016. Dissociative adsorption of O2 on negatively charged nitrogen-doped single-walled carbon nanotubes: First-principles calculations. *RSC Advances*, *6*, 84155–84163.

Srivastava, D., Susi, T., Borghei, M., & Kari, L., 2014. Dissociation of oxygen on pristine and nitrogen-doped carbon nanotubes: A spin-polarized density functional study. *RSC Advances*, *4*, 15225–15235.

Sumpter, B. G., Meunier, V., Romo-Herrera, J. M., Cruz-Silva, E., Cullen, D. A., Terrones, H., … Terrones, M., 2007a. Nitrogen-mediated carbon nanotube growth: Diameter reduction, metallicity, bundle dispersability, and bamboo-like structure formation. *ACS Nano*, *1*, 369–375.

Terrones, M., Terrones, H., Grobert, N., Hsu, W. K., Zhu, Y. Q., Hare, J. P., … Cheetham, A. K., 1999. Efficient route to large arrays of CNx nanofibers by pyrolysis of ferrocene/melamine mixtures. *Applied Physics Letters*, *75*, 3932–3934.

Tsitonaki, A., Petri, B., Crimi, M., Mosbk, H., Siegrist, R. L., & Bjerg, P. L., 2010. In situ chemical oxidation of contaminated soil and groundwater using persulfate: A review. *Critical Reviews in Environmental Science and Technology*, *40*, 55–91.

Usman, M., Byrne, J. M., Chaudhary, A., Orsetti, S., Hanna, K., Ruby, C., … Haderlein, S. B., 2018. *Magnetite and Green Rust : Synthesis , Properties , and Environmental Applications of Mixed-Valent Iron Minerals*.

Vecitis, C. D., Gao, G., & Liu, H., 2011. Electrochemical carbon nanotube filter for adsorption, desorption, and oxidation of aqueous dyes and anions. *Journal of Physical Chemistry C*, *115*, 3621–3629.

Wang, D., Song, P., Liu, C., Wu, W., & Fan, S., 2008. Highly oriented carbon nanotube papers made of aligned carbon nanotubes. *Nanotechnology*, *19*, 075609.

Wu, Z., Yang, S., Sun, Y., Parvez, K., Feng, X., & Müllen, K., 2012. 3D Nitrogen-Doped Graphene Aerogel-Supported Fe 3 O 4 Nanoparticles as Efficient Electrocatalysts for the Oxygen Reduction Reaction. *Journal of the American Chemical Society*, *134*, 9082–9085.

Xue, X., Hanna, K., & Deng, N., 2009. Fenton-like oxidation of Rhodamine B in the presence of two types of iron II, III oxide. *Journal of Hazardous Materials*, *166*, 407–414.

Xue, Y., Liu, J., Chen, H., Wang, R., Li, D., Qu, J., & Dai, L., 2012. Nitrogen-doped graphene foams as metal-free counter electrodes in high-performance dye-sensitized solar cells. *Angewandte Chemie - International Edition*, *51*, 12124–12127.

Appendix
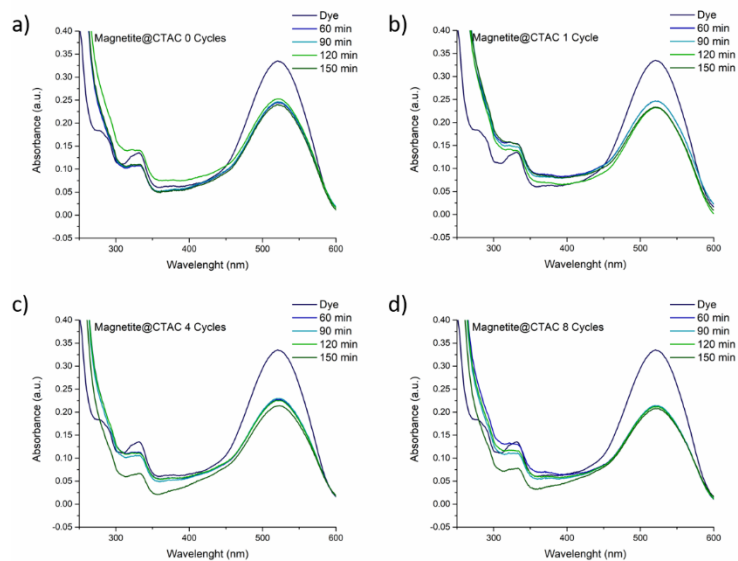
Figure 55. Appendix- Magnetite@CTAC with different cycles.
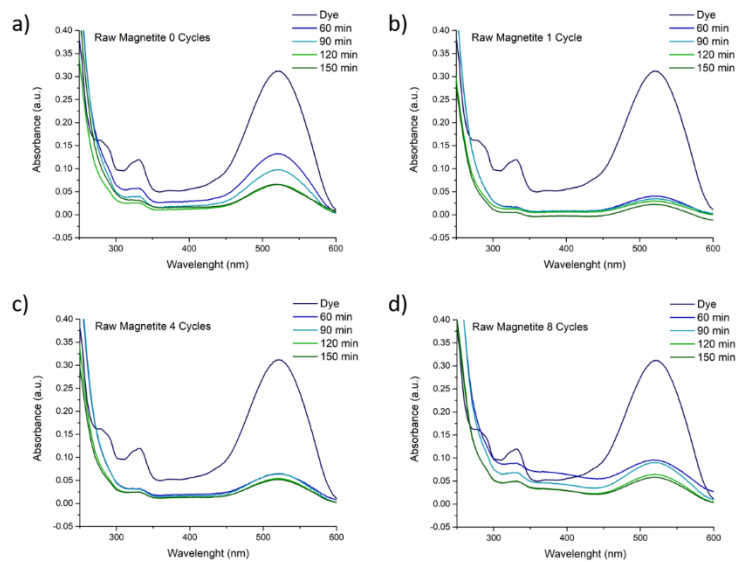
Figure 56. Appendix- Raw Magnetite with different cycles
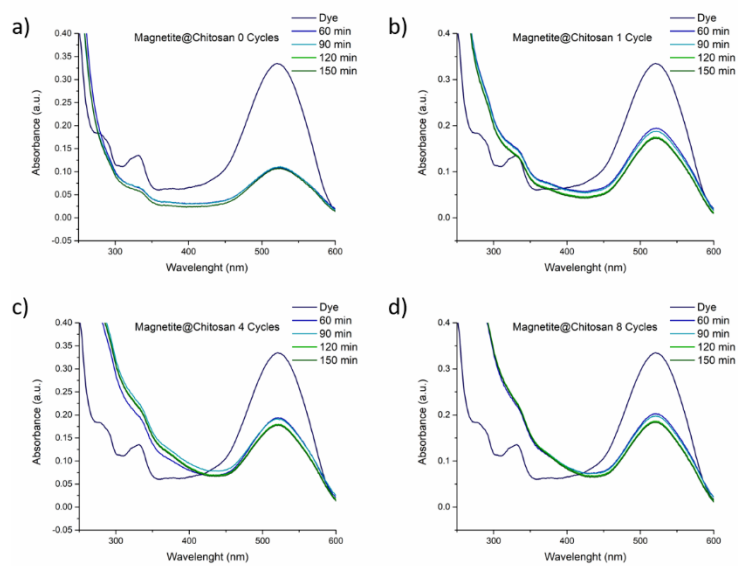
Figure 57. Appendix- Magnetite@Chitosan with different cycles.
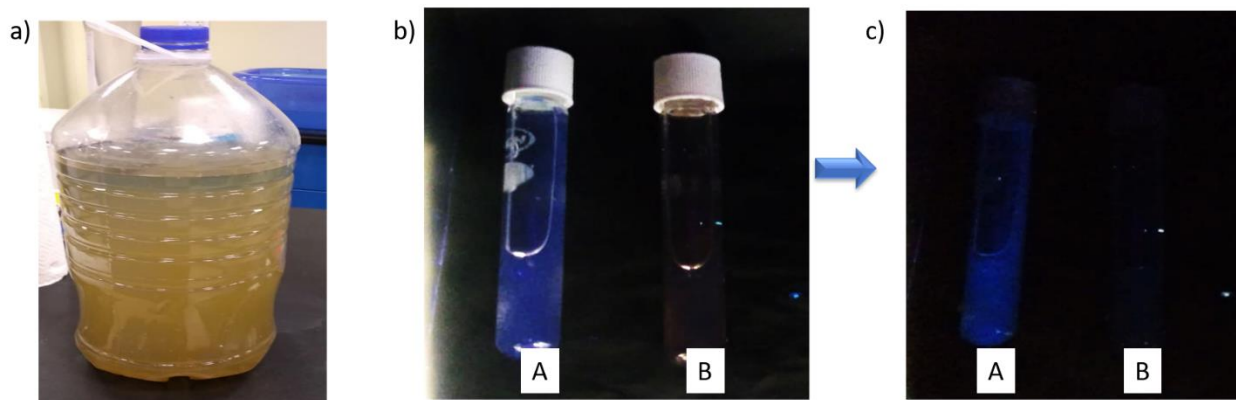
Figure 58. a) Reclaimed wastewater, b) assay tubes before and after treatment under visible light and UV light, and c) assay tubes before and after treatment under UV light.
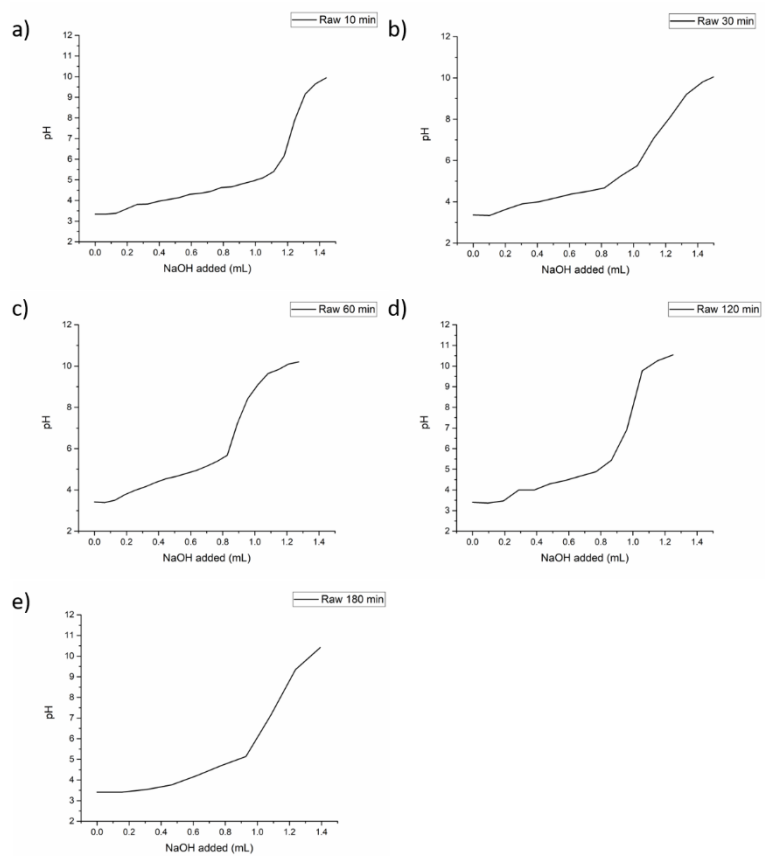
Figure 59. Appendix- Tritiation Curves for the Acetic Acid determination.
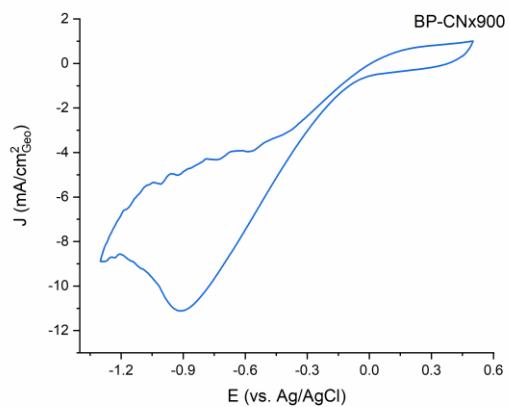
Figure 60. Appendix- CV of the buckypaper in reclaimed wastewater.